2019-09-12

Immiscible Radial Newtonian and non-Newtonian Flow Displacements in Porous Media

Lee, Young Hoon

UNIVERSITY OF CALGARY

Immiscible Radial Newtonian and non-Newtonian Flow Displacements in Porous Media

by

Young Hoon Lee

A THESIS

SUBMITTED TO THE FACULTY OF GRADUATE STUDIES

IN PARTIAL FULFILMENT OF THE REQUIREMENTS FOR THE

DEGREE OF MASTER OF SCIENCE

GRADUATE PROGRAM IN CHEMICAL ENGINEERING

CALGARY, ALBERTA

SEPTEMBER, 2019

Abstract

Immiscible flows that involve radial displacements of shear-thinning or shear-thickening fluids by a Newtonian fluid in a homogeneous porous medium, are modeled numerically. The interfacial instabilities are tracked in time for different values of the rheological parameters, namely the Deborah number (De) and the power-law index (n) and are characterized through the effective number of fingers and the finger area density. The results of the study reveal that the effects of these two parameters on the instability are not monotonic, and it is found that the flow is least unstable for some critical value of either De or n. The dependence of these critical values in particular on the mobility ratio (M) and Capillary number (Ca) is analyzed. It is found that when all other parameters are fixed, the critical Deborah number (De_c) increases as the power-law index increases in shear-thinning fluids or decreases in shear-thickening ones. Similarly, the critical power-law index (n_c) increases with increasing (decreasing) Deborah number in shear-thinning (shear-thickening) flows. Furthermore, both critical parameters are found to vary monotonically with the mobility ratio, with the dependence most noticeable at small values of M. Their variation with the Capillary number is however non-monotonic reaching an extremum at an intermediate value of Ca. An examination of the rate of shear strain at the interface reveals that it consistently shows the smoothest variation and smallest average value at the critical parameter.

In addition to non-Newtonian flow displacements, immiscible radial displacement flows between two Newtonian fluids in a non-homogeneous porous media are also examined numerically. The non-homogeneous porous medium is modeled to vary periodically in the radial direction. Simulations are performed for different values of the Capillary number (Ca) and the mobility ratio (M) varying the frequency of the periodic permeability. The results show that the periodic permeability has negligible effects on the finger structures when the Capillary number and the mobility ratio are small. However, the instability of an interface can be noticeably enhanced in a higher frequency periodic permeability field when the Capillary number and the mobility ratio are large enough.

Acknowledgements

I am so happy to acknowledge my wife Eun Ok and my daughters Seoyeon, Hyeona and Sujung for their support and prayers.

I am also very grateful for my supervisor Dr. Jalel Azaiez and co-supervisor Dr. Ian Gates for their enormous support and guidance.

I am also very thankful for my course instructors Dr. Giovanniantonio Natale, Dr. Luc Bauwens, Dr. Leping Li, and Dr. Da Zhu for their nice teaching and help.

I am also very appreciative for people in the Department of Chemical & Petroleum Engineering for their help.

Finally, I am very thankful for the Lord for everything.

Young Hoon Lee

August, 2019

University of Calgary

Table of Contents

List of Figures

CHAPTER 1

INTRODUCTION

1.1 General

When a less-viscous fluid displaces another fluid of higher viscosity in a porous medium, instability can develop at the interface between the two fluids. Hill examined the instability for the first time in an experiment to displace sugar liquors by water [1]. The instability, which manifests itself in the form of finger-like patterns with the displacing fluid propagating through the displaced fluid, is known as the viscous fingering instability [2]. Viscous fingering instabilities are commonly observed in a broad spectrum of applications such as filtration, fluidization, enhanced oil recovery (EOR) processes, groundwater infiltration, soil remediation, geothermal energy production, and CO_2 sequestration [3], [4], [5]. It was also found that it can describe the dynamics of less common processes such as biological ones involving thin films of cytoskeletal fluids [6] and two-dimensional combustion [7]. Regardless of the applications, these instabilities can have detrimental effects such as in EOR, where they have plagued many processes causing a dramatic reduction in the efficiency of the displacement [8]. They can also be beneficial whenever fluid mixing is important. This is for example the case in CO_2 sequestration where the growth of fingers as a result of the CO_2 rich brine sitting above the CO_2 lean brine, leads to more mixing and an increase in the amount of CO_2 dissolved in water. Viscous fingering has also been proven recently to be a potentially effective approach to enhance mixing in microfluidic devices [9].

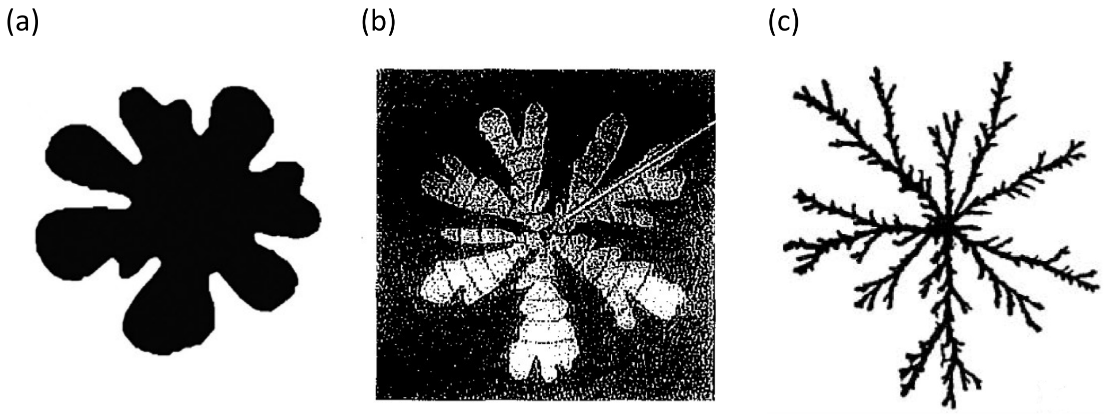

Figure 1.1 *Experimental results from (a) Dias et al. 2012 (b) Kawaguchi et al. 1997 (c) Daccord et al. 1986*

The vast majority of existing literature on the viscous fingering instabilities have focused on Newtonian fluids. However, experimental studies showed that the fingering patterns for non-Newtonian fluids are different from those with Newtonian fluids. In particular, Nittmann et al. performed rectilinear miscible displacement experiments in a Hele-Shaw cell where water displaced non-Newtonian polymer solutions [10]. They found a fractal growth of the viscous finger. Daccord and Nittmann also found fractal viscous fingers when water displaced high-viscosity non-Newtonian polymer solutions in a radial Hele-Shaw cell [11] (see Figure 1.1-c). Kawaguchi et al. analyzed fingering patterns observed when air displaced non-Newtonian hydroxypropyl methyl cellulose (HPMC) solutions with shear-thinning and elastic properties at different injection pressures [12] (see Figure 1.1-b). The fingering patterns showed systematic changes with increasing pressure from dense-branching to tip-splitting and to skewering patterns. They suggested that the pattern morphology strongly depended on the elastic properties. The viscous fingering instability in a rectilinear Hele-Shaw cell where air was injected to displace two different polymer solutions was analyzed by Lindner et al. [13], [14]. They were able to examine the separate effects of the shear-thinning and elastic properties on the width of fingers by using two different solutions. Narrow fingers were observed for the solutions of stiff polymers with shear-thinning property. Wider fingers were however found in the case of solutions of flexible polymers with dominant elastic effects. Miscible flow displacements of Newtonian and shear-thinning fluids in a rectilinear Hele-Shaw cell were investigated by Li et al. [15]. In these experiments, water was injected to displace shear-thinning solutions of Alcoflood polymers. Three Alcoflood polymers were used in three concentrations to prepare weak, medium, and strong shear-thinning solutions. They found that finger structures became more complex for stronger shear-thinning fluids with new fingering patterns. Nagatsu et al. performed a reactive miscible displacement experiment in a radial Hele-Shaw cell. In these experiments, the viscosity of the more-viscous shear-thinning fluid is varied at the interface by changing the pH using neutralization reactions [16]. The fingers were found to get wider with the increase of the viscosity, while narrower fingers were observed with decreasing viscosity. This study has been recently extended to immiscible flows where the surface tension is reduced as a result of chemical reaction [17]. It was found that the reaction has a dual role effect on the fingers development.

Kondic et al. performed nonlinear simulations to study the viscous fingering of a gas displacing a shear-thinning liquid in a radial Hele-Shaw cell [18], [19]. The results showed that the tip-splitting found in a Newtonian fluid was delayed with weak shear-thinning and suppressed with greater shear-thinning. In a subsequent study, Fast et al. studied pattern formation of an *air bubble* expanding into a non-Newtonian fluid in a radial Hele-Shaw cell through both linear stability analysis and nonlinear simulations [20]. They found that the shear-thinning behaviour of the displaced fluid tends to suppress tip-splitting. They suggested that the suppressing tip-splitting could lead to dendritic fingering patterns. Singh and Azaiez conducted numerical simulations to examine the viscous fingering of miscible shear-thinning fluids in a rectilinear Hele-Shaw cell [21]. They found new fingering patterns similar to fractal patterns when shear-thinning fluids displaced a Newtonian fluid.

1.2 Proposed Objectives

The existing studies on the viscous fingering instabilities involving non-Newtonian fluids suggest that the shear-thinning property can have several different effects on the fingering pattern. These include narrowing or widening the width of fingers, suppressing the tip-splitting, and causing fractal fingers. The present study examines thoroughly the shearthinning/thickening effects on the fingering patterns. The present study will analyze the growth of fingers in a radial Hele-Shaw cell or equivalently homogeneous porous medium, where a Newtonian fluid is injected to displace a non-Newtonian shear-thinning or shear-thickening fluid. Most existing studies dealing with non-Newtonian radial displacements were based on the assumption of zero-viscosity of the displacing fluid. As a result, these studies consider only the displaced liquid and assume an infinite mobility ratio. One of the reasons for such an assumption is the challenge in matching the boundary conditions for both the displaced and displacing fluid. In contrast to existing studies on radial flow displacements, the present work considers both phases to have finite but non-zero viscosity. Experimental studies indicate that the dynamics of the flow in very large or infinite mobility ratio displacements are different from those observed in finite mobility ratio ones [22], [23].

Furthermore, unlike the very few studies that looked at displacements where both fluids have finite non-zero viscosities and that considered rectilinear flows, the present study focuses on radial flows. There are important differences that distinguish the physics and flow dynamics as well as the numerical modeling of the radial geometry from its rectilinear counterpart. These include an expanding interface, stronger velocity variations, and special treatment for interface tracking. In addition, as shall be seen later, relations between quantitative characteristics of the interfacial instability and the rheological properties of the displaced non-Newtonian fluid are examined.

Finally, the present study also investigates the immiscible radial displacement flows between two Newtonian fluids in a non-homogeneous porous media whose permeability is modeled to vary periodically in the radial direction. The effects of the frequency of the periodic permeability on the finger stdurcures are examined for different values of the Capillary number (Ca) and the mobility ratio (M).

1.3 Outline

In Chapter 2, a through review of the existing literature on viscous fingering is presented. In Chapter 3, the physical model of the radial displacement flow, the governing equations with boundary conditions, the constitutive equation for describing the shear-thinning and shear-thickening behaviors, and a detailed description of the numerical methods are presented. In Chapter 4, the results from non-Linear simulation of immiscible flows that involve radial displacements of shear-thinning or shear-thickening non-Newtonian fluids by a Newtonian fluid in homogeneous porous media are presented and discussed. In Chapter 5, immiscible radial displacement flows between two Newtonian fluids in a non-homogeneous porous media with a periodic permeability are examined numerically.

CHAPTER 2

LITERATURE REVIEW

In this Chapter, a literature review on pertinent studies is presented. Due to the rather limited number of studies on viscous fingering instabilities for non-Newtonian flows compared to Newtonian ones, the literature review will cover both types of flows. The main rationale is that many of the mechanisms of instability are shared between these two classes of fluids, and it is therefore necessary to benefit from the great wealth of studies on Newtonian flows. Moreover, almost all studies dealing with non-Newtonian fluids focus on comparing the effects of the rheological behaviors of the non-Newtonian fluids by contrasting them with those of Newtonian fluids, and it is therefore very pertinent to have a good understanding of the instability in Newtonian displacements.

In addition to this major classification; Newtonian versus non-Newtonian, displacements can be either miscible or immiscible, develop in simple geometries such as the Hele-Shaw cell or quarter five spot geometries, or in actual heterogeneous porous media. Finally approaches in studying such flow instabilities can be based on either experimental or modeling strategies, or a combination of both. In addition, modeling studies are typically carried out through Linear Stability Analysis (LSA) where the response of the flow to small perturbations is analyzed, or Numerical Simulations (NS) that model the actual nonlinear development of the flow.

The present literature review is divided into three major sections. The first one deals with experimental work, the second presents results of linear stability analysis studies while the third focuses on nonlinear simulations. Each of these sections is subdivided into two subsections that deal with Newtonian and non-Newtonian flows.

2.1 Experimental Studies

In this section, experimental studies involving both real porous media and Hele-Shaw cells or its variants such as the five spot geometry, are presented. Studies dealing with Newtonian flows are first reviewed followed by those on non-Newtonian flows. For each type of flow, the review is presented mostly in chronological order and covers both miscible and immiscible displacements.

2.1.1 Newtonian Flows

Viscous fingering of miscible Newtonian fluids was first examined in 1952 by Hill in a series of experiments that involve the displacement of sugar liquors by water from a vertical, uniformly packed column of charcoal [24]. The author found that the interface became unstable when the less viscous water displaced the more viscous sugar liquors. He formulated his theory quantitatively and defined an expression for a critical velocity using the densities and viscosities of the fluids under small perturbations at the interface. He found that the velocity of the flow should be less than a critical velocity to avoid interfacial instabilities. In the same year, Slobod and Caudle used radiographic techniques to take images of the areal sweep-out patterns during miscible displacements in a plate of fused alundum [25]. They determined areal sweep out efficiencies by varying the mobility ratio and reported that the mobility ratio remarkably affected the sweep efficiency. Five years later, Van Meurs used a three-dimensional model made of glass walls filled with finely powdered glass to visually observe oil displacement processes by water and gas [26]. He performed experiments in three different flow models which were, a rectangular model for the linear water-drive experiments, a model for the five-spot well pattern, and a cylindrical tube model for the solution gas-drive experiments.

In a seminal study in 1958, Saffman and Taylor studied the interfacial instability between two immiscible fluids with different densities and viscosities in a porous medium [27]. They performed experiments using Hele-Shaw cells that were set either horizontally or vertically. For the vertically configured Hele-Shaw cell, the more viscous glycerin was displaced downwards by the less viscous air injected from the top. In this case, the interface became unstable when the injection velocity exceeded a critical velocity. The results showed that the fingers at the later stage of the flow tended to space evenly. In addition, they noted that fingers could inhibit the growth of neighboring fingers when they grew ahead of their neighbors. They also performed experiments using a long horizontal Hele-Shaw cell to study the penetration of a single finger through an infinite channel. A subsequent study carried by Blackwell et al. in 1959 investigated factors influencing the efficiency of miscible displacement in porous media [28]. The authors performed experiments using sand-packed rectangular Lucite models to examine the effects of the mobility ratio, gravity segregation, permeability, and model geometry for miscible displacements.

Artificially consolidated sand models were used in an experimental study by Haberman to determine the efficiency of miscible displacements as a function of mobility ratio [29]. The author found that high mobility ratios mainly caused extensive fingering regardless of the medium heterogeneity. Thus, it was concluded that a miscible-slug dry-gas drive process using a low viscosity solvent was not efficient. Benham et al. studied viscous fingering in miscible displacements under adverse viscosity ratios using an open Hele-Shaw model and the same model packed with glass beads [30]. The authors found that the lengths of fingers were distributed normally and the fingering from a miscible slug displacement was much greater. The effects of injection rates at a fixed viscosity ratio on the shape of fingers were investigated experimentally by Slobod and Thomas in the case of miscible displacement [31]. In addition, other experiments were carried out to study the effect of a continuous gradation in viscosity and an X-ray technique was used to take an image of the fingering patterns. The shape and pattern of fingers were also analyzed using a radiographic technique by Perkins and Johnston for both rectilinear and radial displacements of miscible fluids [32]. The same authors carried a series of experiments to analyze immiscible fingering in Hele-Shaw and Bead-packed models

[33]. They noticed that there were noticeable differences between Hele-Saw cells and Bead-packed models. In particular, it was found that bead-packed models with initial residual water showed very different fingering patterns. A series of experiments in a tilted Hele-Shaw cell were carried out by Wooding to study the growth of fingers at an unstable diffusing interface [34]. The author found that the mean amplitude of fingers grew as a square of time and they grew proportional to time after a transitional period.

Paterson studied radial fingering in a circular Hele-Shaw cell that developed when air was injected at the center to displace glycerin [35]. He also examined fingers that develop as a result of the withdrawal of glycerin which was enclosed by oil in a radial Hele-Shaw cell. The author derived an equation for the minimum wavelength required for the growth of fingers in a radial outward displacement. In addition, he presented approximate equations for the growth rate of the fingers and the shape of a long finger. The results from the equations were compared with the fingers from experiments. They verified that the displacement is stable if the circumference of the injected fluid is less than the minimum wavelength. They also found that the suggested maximum wavelength matched the wavelength of the initiall fingers.

A number of subsequent studies examined factors that may affect the instability aside from the fluids properties (mobility ratio, surface tension) or those of the porous medium (e.g. permeability). These include the surface of the plates in Hele-Shaw cells, the presence of heat transfer, chemical reaction, as well as the nature and orientation of the flow. The following review though not exhaustive covers some of the most salient or initial studies on these aspects.

The first study that had analyzed the effects of the plate roughness on viscous fingering was carried by Chen for both miscible and immiscible displacements in a radial Hele-Shaw cell [36]. The author also examined the effects of the flow rate and the interfacial tension on the fingering instability. The effects of the cell orientation were analyzed by Kong et al. who performed experiments to visualize steam injection processes in Hele-Shaw cells that were horizontal, tilted, and vertical [37]. The authors used both Newtonian mineral oil and non-Newtonian crude oil and synthetic oil. The first study dealing with miscible viscous fingering experiments inside three-dimensional (3-D) porous media were carried out by Bacri et al. [38]. The authors used an acoustic technique to determine the concentration in the porous media. Concentration profiles were measured at 10 different locations along the flow direction and the growth of profiles were examined in three different porous media. The experimental data showed that there was a crossover regime between diffusive and convective regimes. In addition, they also found that the viscosity ratio and gravity had an influence on the instability. Banpurkar et al. studied viscous fingering of the immiscible kerosene-glycerin system in an anisotropic radial Hele-Shaw cell [39]. The anisotropy on the bottom plate of the Hele-Shaw cell was achieved by attaching a patterned copper circuit board on the plate. Thermal effects were considered in a study by Nagatsu et al. who had investigated non-isothermal miscible displacements in a radial Hele-Shaw cell by injecting less-viscous liquids at high temperature (80°C) to displace high viscosity liquids at room temperature [40]. The authors found that the effect of non-isothermal displacements was non-monotonic with respect to the mobility of the existing fluid and monotonic with the injection rate. White and Ward performed immiscible displacements experiments in a radial Hele-Shaw cell where a precipitation reaction happened at the gas-liquid interface [41]. The effects of the nature of the injection flow were examined in a study by Dias et al. who performed a series of experiments in a radial Hele-Shaw cell with time-dependent injection rates to minimize the growth of fingers [42] (see Figure 1.1-a).

2.1.2 Non-Newtonian Flows

When compared with Newtonian flows, one is forced to note that there are fewer studies dealing with non-Newtonian flow displacements where either or both fluids exhibit some form of non-Newtonian behavior. This may be attributed in part to the complexity of non-Newtonian flow displacements and the challenges in characterizing accurately the rheological behavior of non-Newtonian fluids.

One of the earliest studies was carried out in 1967 by Marshall and Metzner who performed experiments to examine the flow of polymeric non-Newtonian solutions through a sintered bronze porous disk [43]. Three different polymeric materials were used to prepare the non-Newtonian fluids with very low, intermediate, and high relaxation times. The authors were able to measure increased pressure drops at Deborah numbers that characterize the elastic behavior, beyond 0.05. A study published in the same year by Dauben et al. examined slow flow displacements of shear-thinning polymer solutions through a cylinder packed with glass beds [44]. In the subsequent year, Lee and Claridge conducted miscible displacement experiments in a five-spot Hele-Shaw cell model using shear-thinning polymer solutions to displace glycerin-water mixtures [45]. They measured the areal sweep efficiency of the displacement. It was found that the areal sweep at a breakthrough was poorer than those where a Newtonian fluid with similar viscosity was injected. However, the areal sweep efficiency was significantly improved at 1 pore volume (PV) injection of a shear thinning solution compared to the case with water injection. Savins reviewed studies on the complex flow behavior of non-Newtonian fluids in a porous media where the shear rates in the flow were values of the order of one s^{-1} [46].

Nittmann et al. performed rectilinear miscible displacement experiments in a rectilinear Hele-Shaw cell where water was used to displace more viscous non-Newtonian polymer solutions [10]. The authors reported a fractal growth of the viscous fingers. A related study by Daccord and Nittmann published in the same year, showed that fractal viscous fingers were observed when water displaced high-viscosity non-Newtonian polymer solutions in a radial Hele-Shaw cell [47]. The authors found that the fingering patterns from a Hele-Shaw cell initially containing a non-Newtonian fluid were very different from those with Newtonian fluids. Experiments in a radial Hele-Shaw cell using Newtonian and non-Newtonian fluids were carried out by Allen and Boger in 1988 [48]. Water was injected to displace shear-thinning polyacrylamide and polysaccharide solutions in order to investigate the fingering patterns at the rear interface between chasing waterflood and polymer slug in polymer flooding. The interface between water and the shear-thinning fluids became significantly more unstable. However, elastic fluids showed negligible effects on the fingering patterns. A series of experiments involving the displacement of aqueous colloidal suspensions with air in a Hele-Shaw cell was conducted in the same year by Damme et al. [49]. The authors compared the morphological features of highly branched fractal viscoelastic fingering patterns from the experiments with those obtained by injecting water.

Smith et al. examined the development of a finger that penetrated into a linear Hele-Shaw cell containing polystyrene solutions [50]. It was found that the width of the finger started to become narrow at a shear rate which was about the inverse of the polymer Zimm relaxation time. The variation of the width of fingers in a linear Hele-Shaw cell were further analyzed by Bonn et al. for flows involving the injection of a less viscous oil to displace a more viscous water with the addition of surfactant [51]. For the system with polymer solutions, the air was injected as the displacing fluid. The finger width was measured as a function of velocity and it was reported that the width reached a minimum value, increased with increasing velocity and settled at a plateau value. Fingering patterns observed at different injection pressures where air displaced non-Newtonian hydroxypropyl methyl cellulose (HPMC) solutions that exhibit both shear-thinning and elastic properties were analyzed by Kawaguchi et al. in radial Hele-Shaw cells [12]. The fingering patterns with increasing pressure showed systematic changes from dense-branching to tip-splitting and to skewering patterns. The authors suggested that the pattern morphology strongly depended on the elastic properties.

Lindner et al. studied viscous fingering instability in linear Hele-Shaw cell where air was injected to displace two different polymer solutions [14]. By using two different solutions, they were able to separately examine the effects of two non-Newtonian properties; shear thinning and elastic effects, on the width of fingers. Narrow fingers were observed for the solutions of stiff polymers with shear thinning property. Wider fingers were however found in the case of solutions of flexible polymers with dominant elastic effects. Li et al. investigated miscible flow displacements of Newtonian and shear-thinning fluids in a rectilinear Hele-Shaw cell [15]. Water was injected to displace shear-thinning solutions of Alcoflood polymers. Three Alcoflood polymers were used at three different concentrations to prepare weak, medium, and strong shear-thinning solutions. The viscosity of the polymer solutions was measured using a rheometer over the shear-rate range from 0.01747 to 140 s^{-1}. The viscosity measurements were then fitted to a modified Carreau-Yasuda model. The polymer solution relaxation time was estimated as the inverse of the shear-rate at the start of shear-thinning effect. The range of Deborah number in the experiments was from 0.03 to 7.8. It was found that finger structures became more complex for stronger shear-thinning fluids with new fingering patterns not observed in Newtonian fluid displacements. Nagatsu et al. performed a reactive miscible displacement experiment in a radial Hele-Shaw cell where the viscosity of the more-viscous shear-thinning fluid is varied at the interface by changing pH using neutralization reactions [16]. Fingers were found to get wider with the increase of the viscosity, and narrower fingers were observed with decreasing viscosity. This study has been recently extended to immiscible flows where the surface tension is reduced as a result of chemical reaction [17]. It was found that the reaction has a dual role effect on the finger development.

The Saffman-Taylor instability in yield stress fluids was investigated by Lindner et al. [52]. They performed experiments using gels and foams in a rectilinear Hele-Shaw cell and observed very branched fingers in the gel. They also found a crossover from yield stress dominated to viscous behavior. Malhotra and Sharma performed an experimental study to examine the influence of fluid elasticity on miscible viscous fingering [53]. Water was injected to displace constant viscosity elastic fluids (Boger fluids) in a rectilinear Hele-Shaw cell. They observed the growth of multiple thinner and longer fingers. An extensive review of experimental studies by McCloud and Maher covered a wide variety of experiments with additional perturbations to the Saffman-Taylor flow [5]. The dynamics of driven interfaces and the relation of material properties to dynamical pattern evolution can be better understood with the experiments.

2.2 Linear Stability Analysis

2.2.1 Newtonian Flows

In his 1952 study discussed earlier, Hill analyzed the stability of the interface for a small depression at the interface in a vertical uniformly packed column [24]. He derived an equation for a critical velocity using the densities and the viscosities of the fluids. For a small perturbation, the flow becomes unstable if the velocity exceeds the critical velocity when the density and viscosity of the displacing fluid are smaller than those of the displaced one. In the case where the displacing fluid is denser and more viscous than the displaced fluid, the flow becomes stable if the velocity exceeds the critical velocity v_c determined by

$$v_c = \frac{g(\rho_1 - \rho_2)}{k(\mu_1 - \mu_2)}$$

where μ_2 and ρ_2 are the viscosity and density of the displacing fluid, and μ_1 and ρ_1 are the viscosity and density of the displaced one. The constant k must be determined experimentally. It is not related to permeability. Saffman and Taylor (1958) also performed a linear stability analysis for the interface between two immiscible fluids in a homogeneous porous medium assuming the normal velocity and the pressure were continuous at the interface [27]. The instability condition was derived for the wave-like perturbation on the interface. It was found that the wavelength of the disturbance had no effect on the instability condition. A similar linear stability analysis study of the interface for immiscible liquid-liquid displacements in a *tilted* permeable media considering the surface tension was carried out by Chuoke and Meurs [54]. The authors derived an equation for a critical velocity using the densities, viscosities, permeabilities and the directional cosine. It was found that the instability will occur for all flowrates greater than the critical velocity if the initial disturbance of the interface contains modes with wavelengths greater than a critical wavelength. They also reported that there is a wavelength which leads to a maximum instability.

Schowalter developed a stability criteria for the displacement of a fluid in a porous medium by injecting at a constant velocity in the direction of gravity, a more dense fluid which is miscible with the existing fluid. He showed that the displacement velocity had a significant effect on the stability criteria [55]. The conditions for the onset of instability during two-phase immiscible displacement in porous media were examined by Peters and Flock [55]. A dimensionless number and its critical value for predicting the start of instability were presented. The dimensionless number was derived from a stability theory for a cylindrical system. A theoretical analysis of the stability of miscible displacements in homogeneous porous media for rectilinear flow was carried out by Tan and Homsy (1986) [56]. In deriving the predictions of the growth rate, they made use of the quasi-steady-state approximation that assumes that the growth of disturbances is faster than the change of the base state, except at short times where the base state changes rapidly. The predictions were compared with several experiments in the literature, and they gave a good prediction of unstable fingers. A subsequent study by the same authors involved a linear stability analysis for miscible displacements for a radial source flow in homogeneous porous media [57].

Effects other than the fluids properties were also investigated in a number of studies. Ghesmat and Azaiez studied viscous fingering instability in porous media with anisotropic velocity-dependent dispersion [58]. They performed the linear stability analysis of the flow to determine the effects of the main parameters on the growth of the disturbances using a similar approach to that by Tan and Homsy. They found that stronger dispersion resulted in larger growth rates of disturbances. The flow became less unstable with an increase in the dispersivity ratio. Alhumade and Azaiez carried out a linear stability analysis of reversible reactive flow displacements in a rectilinear Hele-Shaw cell [59]. They considered that the viscous fingering was caused by the viscosity mismatch between the reactants and the product. They found that the growth of instability can be reduced by increasing the reversibility of the reaction. However, the instability can be increased if the reversibility exceeds a critical value which depends on the mobility ratios of the different species. Ghesmat et al. performed a linear stability analysis to examine the impact of nanoparticle on the hydrodynamic instability around a miscible front [60]. They found that nanoparticles have destabilizing effects in the initial stage. However, it was found that nanoparticles stabilize the miscible front at longer times due to the deposition of nanoparticles into the medium. Linear stability analysis for viscous fingering of a miscible reactive interface was carried out by Hejazi et al. in order to classify the various possible instability scenarios [61]. They found that injecting a more viscous fluid into a less viscous fluid can even lead to an unstable interface when the chemical reaction results in non-monotonic viscosity profiles.

2.2.2 Non-Newtonian Flows

One of the earliest LSA studies on non-Newtonian flows is attributed to Pascal who examined in 1998 the stability of immiscible non-Newtonian fluid interfaces in porous media and developed approximate analytical solutions for describing the stability conditions [62]. The displacing and displaced fluids were non-Newtonian, and the power law model was used to describe their rheological behavior. For the radial displacement, the solution showed the existence of a critical value for the interface location from which the disturbance would stabilize or grow. For a rectilinear displacement without gravity force, the solution showed the existence of a critical interface velocity. In a subsequent study, Wilson performed a linear stability analysis of immiscible non-Newtonian fluid interfaces in a rectilinear Hele-Shaw cell [63]. Oldroyd 'Fluid B' model was used for the purely elastic fluid, and Ostwald-de Waele power-law model was used for the purely shear-thinning fluid. The author concluded that the shear-thinning behavior does not have a great effect on the fingering patterns. On the other hand, the elastic fluid showed qualitatively new effects but not greatly different from a Newtonian fluid, and the new effects may result in an increase of the growth rates of fingers. He suggested that the power law model might not be good enough because of the assumption of zero yield stress. A linear stability analysis of immiscible displacements of a non-Newtonian shear-thinning and-thickening fluids which were also represented by the power law model, was carried out by Sadar et al. in the case of a radial Hele-Shaw cell [64]. An *inviscid* fluid was injected to displace the shear-thinning fluid. The authors found that decreasing the power-law index caused fingering patterns to develop rapidly. They concluded that displacing shear-thinning fluids can lead to fractal fingering patterns at a much earlier stage than displacing Newtonian fluids.

Azaiez and Singh performed a linear stability analysis of the viscous fingering of miscible non-Newtonian flow displacements in a rectilinear Hele-Shaw cell [65]. The Carreau model was used to represent the shear-thinning fluid using two parameters, *De* and *n*. It was found that stronger shear-thinning behavior of the displaced fluid contributed to less unstable flow. Recently, Shoghi and Norouzi studied the viscous fingering instability of miscible fluids in the presence of permeability heterogeneity using LSA [66]. They found that shear-thinning fluids can suppress the instability in cases where the mobility ratio is high and/or the heterogeneity of the medium is adverse.

2.3 Nonlinear Simulations

2.3.1 Newtonian Flows

Koval (1963) considered the factors such as longitudinal dispersion and channeling for viscous fingering and developed an empirical model, K-factor method using a number K which was the product of a heterogeneity factor and an effective viscosity ratio [67]. The K-factor method was able to predict recovery and solvent cut given a pore volume of solvent injected. However, this method could not predict the growth and shape of fingers. Todd and Longstaff (1972) developed and verified a method for modifying existing numerical reservoir simulators to simulate miscible flooding [68]. Fayers (1988) derived one-dimensional model to approximate miscible viscous fingering with physically related parameters [69].

A 1962 reference work by Peaceman and Rachford presented a system of partial differential equations for miscible fluids displacements including gravity, medium permeabilities, fluid viscosities and diffusion [70]. The finite difference method was presented and tested to solve the system of equations for a horizontal two-dimensional geometry. They found that the propagation rate of the fingers was similar to the rate observed in experiments. In addition, the simulation results agreed with the experiments in the dependence of oil recovery on the amount of injected solvent. Christie and Bond performed nonlinear simulations for the unstable miscible flooding using the same equations [71]. The pressure equations with a concentration-dependent mobility were solved using the incomplete Choleski conjugate gradient (ICCG) technique [72]. The authors were able to run simulations with mobility ratio from 5 to 86 for large Péclet numbers. The results showed good agreement with Blackwell's [28] and Handy's experiments [73].

Tan and Homsy conducted nonlinear simulations for viscous fingering in miscible displacement using a Fourier spectral method as the basic scheme [74]. The flow instability was governed by two parameters, the Péclet number (Pe) and mobility ratio (M). In this study, the dispersion was considered to be isotropic. It was found that the growth rate and the wavelength of fingers at short times matched well the results from their linear stability analysis. The tip-splitting phenomenon was identified and studied for the first time. Christie further developed the finite difference scheme for high-resolution nonlinear simulations of two-phase, three-component flow [75]. The numerical methods were able to simulate both miscible and immiscible displacements simultaneously. It was reported that the capillary pressure had stabilizing effects on viscous fingering in immiscible flows. The simulation results also showed that injecting water and solvent simultaneously at the optimum water-alternating-gas (WAG) ratio could almost completely stabilize viscous fingering. Particle-tracking simulations were conducted by Araktingi and Orr to study the combined effects of viscous fingering, gravity segregation, and reservoir heterogeneity in miscible displacements in vertical cross sections [76]. The effects of anisotropic dispersion on viscous fingering of miscible displacements were analyzed through nonlinear simulation by Zimmerman and Homsy [77]. A Hartely transform-based numerical scheme was used and the dispersion coefficients were determined from Taylor dispersion in Hele-Shaw cells. The same authors extended their aforementioned nonlinear simulations to include a general velocity-dependent dispersion [78]. They also extended the isotropic simulation of Tan and Homsy [77] to much broader and longer domains.

In 1997 Chen et al. presented a simple level set method for implicitly evolving sharp interfaces between two immiscible phases [79]. Complicated interfacial shapes such as fingering of immiscible phases were captured using this method. In the same year, Hou et al. introduced a hybrid numerical method utilizing the immersed interface method and the level set method together for moving interface problems [80]. They applied this method to simulate viscous fingering of immiscible displacements in a Hele-Shaw cell. Guan and Pitchumani developed a volume tracking method to simulate viscous fingering in a Hele-Shaw cell with finite viscosity ratio and interfacial tension [81]. They examined the effects of finite viscosity ratio and capillary number. In the process, they identified four distinct finger patterns depending upon the viscosity ratio and the modified capillary number for constant flow rate or for constant driving pressure difference. Ghesmat and Azaiez (2007) performed nonlinear simulations for viscous fingering of miscible displacements with anisotropic velocity-dependent dispersion [58, 60]. The model equation from Bear [82] was used to determine the longitudinal and transverse dispersion coefficients along the flow streamline. They examined the velocity field to explain the development of new fingering patterns.

The effects of time-dependent injection flows on finger patterns in miscible displacements were examined by Yuan and Azaiez through numerical simulations [83]. The authors found that the effects of the velocity amplitude and cycle period were significant when the inertial effects were considered in the simulations. The viscous fingering instability between two immiscible Newtonian fluids within a Hele-Shaw cell were investigated by Jackson et al. [84]. The boundary element method was used to determine the normal velocity at the interface. They studied the effects of mobility ratio ranging from 1 to 1000 and capillary number varying between 2000 to 12000. Lins and Azaiez examined the effects of time-dependent injection schemes on the nonlinear development of fingering patterns in immiscible displacements [85]. A hybrid scheme combining the immersed interface method and the level set method was used in the numerical simulations. The cyclic schemes with small periods and large amplitudes lead to less unstable interfaces. Monotonic injection schemes reduced the growth of viscous fingering at high surface tensions and low mobility ratios. The same authors investigated in a more recent study the effects of radial cyclic injection flows of immiscible fluids [86]. They mainly examined the effects of the period of the sinusoidal injection and found resonance-like effects where the fingering structures were significantly changed at a critical period. Chen and Meiburg conducted a detailed computational investigation for the two-dimentional miscible quarter five-spot displacements in a homogeneous porous media [87]. They performed simulations to investigate the effects of the Péclet (Pe) number and the mobility ratio on the flows. Vigorous viscous fingering near the injection well was observed with sufficiently large Pe. They found a clear separation in space and time scales in the flow. Small scales were observed near the injection well and the production well. However, larger scales dominated the central domain. They also tried to optimize recovery by using a time-dependent injection rate because the flows showed apparent spatial non-uniformity. They found that the recovery can be increased by reducing the flow rate at early times and then increasing it at later times. Almarcha et al. studied theoretically and experimentally the effects of density changes due to a reaction on the buoyancy-driven instabilities at a horizontal interface between two liquids [88]. They performed an experiment with HCL solution on top of NaOH solution in a vertical Hele-Shaw cell. A sinusoidal perturbation was observed slightly above the contact line soon after contact, and then fingers developed. They also numerically showed that the reaction can make a buoyantly stable system unstable. Sajjadi and Azaiez investigated miscible flow displacements with unfavorable mobility ratios through horizontal layered heterogeneous media [89]. They examined the effects of a wide range of parameters such as the injection velocity, diffusion, viscosity, and the heterogeneity length scale and variance on the flow instability. It was revealed that the flow displacements in layered heterogeneous media show similar flow regines as the ones in homogeneous media. Yuan et al. investigated the concentration-dependent diffusion coefficient (CDDC) in nonlinear numerical simulations of frontal instabilities and mass transfer in a homogeneous porous media [90]. In the study, the diffusion coefficient is exponentially proportional to concentration. The frontal instabilities on mass transfer were enhanced when the CDDC was adopted in a simulation. They found that instabilities develop at a very early time with a sharp interface. Huang and Chen performed non-linear simulations using a diffuse-interface method to examine the influence of fluid miscibility and injection scheme on radial displacements in a Hele-Shaw cell [91]. They examined two injection schemes, constant and linear injection rates, and three miscibility conditions, immiscible with surface tension, partially miscible with effective interfacial tension and fully miscible. It was found that the linear injection scheme has stabilizing effects on all three miscibility conditions. They also found that the linear injection scheme in a fully miscible interface shows different results such as longer channeling zone and interfacial length. They suggested that the different results are from the absence of the interfacial tension at the miscible interface.

2.3.2 Non-Newtonian Flows

Kondic et al. derived a generalized Darcy's law where the viscosity is a function of the squared pressure gradient [18]. Kondic et al. (1998) performed nonlinear simulations to study the viscous fingering of a gas displacing a shear thinning liquid in a radial Hele-Shaw cell [92]. Darcy's law generalized for non-Newtonian fluids was used in the numerical simulations. The results showed that the tip-splitting found in a Newtonian fluid was delayed with weak shear thinning and suppressed with greater shear thinning. Fast et al. (2001) studied pattern formation of an air bubble expanding into a non-Newtonian fluid in a Hele-Shaw cell through numerical simulations [20]. They found that the shear-thinning behavior of the displaced fluid suppressed tip-splitting. They suggested that the suppressing tip-splitting could lead to dendritic fingering patterns.

Lindner et al. suggested that the effective Darcy's law, in which the constant viscosity was replaced by the shear-thinning viscosity, was able to model weakly shear-thinning fluids [13]. However, the effective Darcy's law was not recommended for stronger shear-thinning fluids. Singh and Azaiez conducted numerical simulations to examine the viscous fingering of miscible shear-thinning fluids in a rectilinear Hele-Shaw cell [21]. A pseudo-spectral numerical technique based on the Hartely transform was used, and Darcy's law was modified such that a shear-dependent viscosity replaced the constant viscosity. The modified Carreau Model was used to determine the viscosity of non-Newtonian fluid. The results for shear-thinning fluid displacing a Newtonian fluid showed new fingering patterns that were similar to fractal patterns. Shoghi and Norouzi examined the viscous fingering instability of miscible non-Newtonian fluids in the presence of permeability heterogeneity [66]. Carreau Model was used to determine the viscosity of non-Newtonian fluid. The magnitude of the rate-of-strain tensor was determined using the second invariant of the rate-of-strain tensor. More recently, Shokri et al. studied the viscous fingering instability of miscible displacement involving a viscoelastic fluid in a rectilinear Hele-Shaw cell using a numerical method and linear stability analysis for the first time [93]. The simulations covered Weissenberg numbers from 2 to 20. It was found that the system becomes less unstable with the increase in Weissenberg number. The same research team had also examined the viscous fingering instability of miscible displacement involving a nonlinear viscoelastic fluid in horizontal layered heterogeneous medium in addition to a homogeneous media [94]. Shi and Tang studied immiscible non-Newtonian displacements in a simplified porous media using the lattice Boltzmann method [95]. Fingers became more unstable with the increase of the capillary number, and lower displacement efficiency was obtained with the increase of the viscosity ratio. In addition, shear thickening fluid showed higher displacement efficiency than shear thinning fluid. Recently, Yazdi and Norouzi performed a numerical study for Saffman-Taylor instability of an immiscible nonlinear viscoelastic fluid displacing Newtonian fluid in a rectilinear Hele-Shaw cell [96]. They applied the volume of fluid method for predicting the formation of two phases and the Giesekus model as the constitutive equation for the viscoelastic fluid. They examined the destabilizing effect of shear-thinning property of nonlinear viscoelastic fluid on the interfacial instability. It was found that the fluid elasticity and capillary number decrease the intensity of the interface. Noorouzi performed another study on Saffman-Taylor instability of immiscible viscoelastic-Newtonian displacement in a rectilinear Hele-Shaw cell [97]. In this study, the Oldroyd-B constitutive equation which describes Boger liquids better was used. They found that the elasticity of the displacing fluid stabilizes the flow field in the presence of interfacial tension.

2.4 Conclusion

There are limited number of studies on viscous fingering instabilities for non-Newtonian flows compared to Newtonian ones. However, the existing studies on the viscous fingering instabilities involving non-Newtonian fluids suggest that the shear-thinning property can have several different effects on the fingering structures which include narrowing or widening the width of fingers, suppressing the tip-splitting, and causing fractal fingers. Those different effects of shear-thinning/shear-thickening fluids are thorouly examined in this study.

CHAPTER 3

MODEL AND METHODOLOGY

In this Chapter, the physical model of the flow, the governing equations with boundary conditions, and the constitutive equation for describing the shear-thinning and shear-thickening behaviors are presented. This is followed by a detailed description of the numerical methods used to solve the model equations. This Chapter will be wrapped with a presentation and discussion of the numerical code we have developed to solve the flow problem, its implementation, validation and convergence.

3.1 Model Geometry and Governing Equations

In this first section, the considered geometry in which the flow develops is presented. Subsequently, the governing equations and corresponding boundary conditions are discussed. Furthermore, the constitutive equation to characterize the rheological behavior of the non-Newtonian fluid are detailed.

3.1.1 Model Geometry

The domain under consideration consists of a horizontal two-dimensional homogeneous square [2a x 2a] porous medium with constant permeability k. The flow is under the creeping regime where inertial effects can be neglected and it is assumed that it develops radially from a centre source. A Newtonian fluid (fluid 1) of viscosity η_1 is injected in the centre of the domain to displace radially a second fluid (fluid 2) of viscosity η_2, that initially occupies the porous medium. The displaced fluid considered in this study is non-Newtonian, with a shear dependent viscosity; $\eta_2(\dot{\gamma})$ and a zero-shear viscosity η_{20}. A related variable that will be used throughout this study is the mobility $\beta_i = {}^{K}/_{\eta_i}, i = 1{,}2$ defined as the ratio of the medium permeability and the fluid viscosity. In the case of the non-Newtonian fluid, the mobility is based on the zero-shear viscosity, η_{20}. Both fluids are assumed to be fully immiscible with a surface tension τ, and the flow is considered to be isothermal. A schematic of the flow is depicted in Figure 3.1.

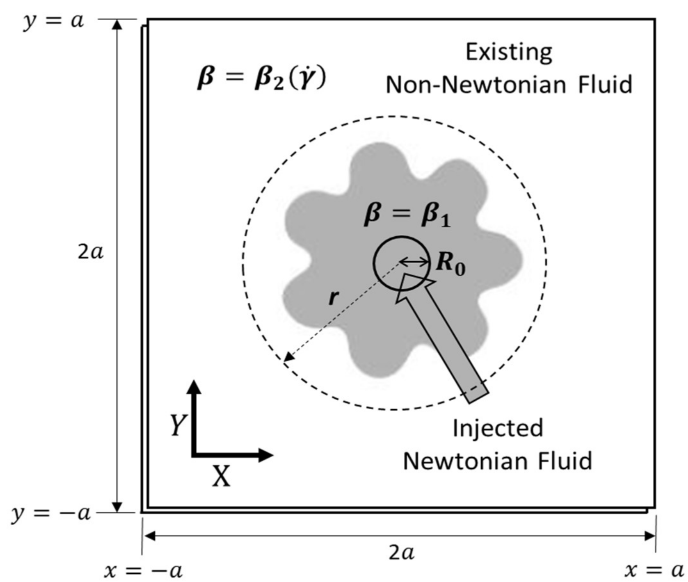

Figure 3.1 *Schematic of the two-fluid radial displacement in the porous medium.*

3.1.2 Governing Equation

The flow displacement is governed by the following equations:

$$\nabla p = \begin{cases} -\dfrac{1}{\beta_1} U & fluid\ 1 \\ -\dfrac{1}{\beta_2(\dot{\gamma})} U & fluid\ 2 \end{cases} \tag{3.1}$$

$$\nabla \cdot U = \begin{cases} \phi(r), & r \leq R_0 \\ 0, & r > R_0 \end{cases} \tag{3.2}$$

Equation (3.1) for fluid2 is a modified Darcy's law in which a shear-dependent mobility $\beta_2(\dot{\gamma})$ is used in the case of the non-Newtonian fluid [13], [21], [65], [66]. Equation (3.2) is the continuity equation for incompressible fluids with a source term $\phi(r)$ in the injection area. The boundary conditions at the interface are

$$[p]_1^2 = \tau\kappa \tag{3.3}$$

$$[U_n]_1^2 = 0 \tag{3.4}$$

The pressure drop across the interface is determined using the Laplace-Young equation (3.3) where τ is the surface tension and κ is the curvature of the interface. Equation (3.4) is the kinematic boundary condition. The injection strength $\phi(r)$ is distributed over the injection area [86]:

$$\phi(\mathrm{r}) = \begin{cases} \varphi_0[1 + \cos(\pi \mathrm{r}/\mathrm{R}_0)], & \mathrm{r} \leq \mathrm{R}_0 \\ 0, & \mathrm{r} > \mathrm{R}_0 \end{cases} \tag{3.5}$$

where φ_0 is the injection strength coefficient. The constant injection rate Q_0 can be obtained by integrating $\phi(r)$ over the injection area:

$$\mathrm{Q}_0 = \varphi_0 {\mathrm{R}_0}^2 \left(\pi - \frac{4}{\pi}\right) \tag{3.6}$$

The non-Newtonian shear-thinning or shear-thickening behavior of fluid2 may be represented using the Ostwald de Waele Power-Law model commonly adopted in other studies [13] [62]

[63] [64] [95]. However, this model fails at very small shear rates and the Carreau model will be adopted instead:

$$\frac{\eta - \eta_\infty}{\eta_0 - \eta_\infty} = [1 + (\lambda\dot{\gamma})^a]^{\frac{n-1}{a}} \tag{3.7}$$

In the above equation η_0 is the zero-shear rate viscosity, η_∞ is the infinite-shear-rate viscosity, λ is a time constant, n is the power-law index, and a describes the transition region from the zero-shear rate to the power-law region [98]. The magnitude of the rate of strain tensor, $\dot{\gamma}$ is determined using the second invariant:

$$\dot{\gamma} = \sqrt{\frac{1}{2}\sum_i \sum_j \dot{\gamma}_{ij}\dot{\gamma}_{ji}} \tag{3.8}$$

where $\dot{\gamma}_{ij}$ is the rate of strain tensor $(\partial u_i/\partial x_j + \partial u_j/\partial x_i)$. The mobility of the shear-thinning fluid becomes, using $\eta_\infty = 0$ and $a = 2$:

$$\beta_2(\dot{\gamma}) = \frac{\beta_{20}}{[1 + (\lambda\dot{\gamma})^2]^{\frac{n-1}{2}}} \tag{3.9}$$

where β_{20} is the zero-shear rate mobility of the non-Newtonian displaced fluid.

The governing equations are made dimensionless using the following scaling factors: $1/\phi_0$ for time, R_0 for length, $\phi_0\mathrm{R}_0$ for velocity, and $\phi_0\mathrm{R}_0^2/\beta_1$ for pressure, where $\phi_0 = \mathrm{Q}_0/\pi\mathrm{R}_0^2$. The resulting governing equations and boundary conditions in dimensionless form are:

$$\nabla^* p^* = \begin{cases} -\mathrm{U}^* & fluid\ 1 \\ -M_g\mathrm{U}^* & fluid\ 2 \end{cases} \tag{3.10}$$

$$\nabla^*.\,\mathrm{U}^* = \begin{cases} \phi^*, & r^* \leq 1 \\ 0, & r^* > 1 \end{cases} \tag{3.11}$$

$$M_g = M[1 + (De\dot{\gamma}^*)^2]^{\frac{n-1}{2}} \tag{3.12}$$

$$[p^*]_1^2 = \tau^* \kappa^* \tag{3.13}$$

$$[\mathrm{U}_n^*]_1^2 = 0 \tag{3.14}$$

In the above equations, $\mathrm{U}^* = \mathrm{U}/(\mathrm{R}_0 \phi_0)$, $\mathrm{U}_n^* = \mathrm{U}_n/(\mathrm{R}_0 \phi_0)$, $r^* = r/\mathrm{R}_0$, $\phi^* = \phi/\phi_0$, $\tau^* = \tau\beta_1/\mathrm{R}_0^3\phi_0$, $p^* = p\beta_1/\phi_0 \mathrm{R}_0^2$, $\kappa^* = \kappa \mathrm{R}_0$, $M = \beta_1/\beta_{20}$, $De = \lambda\phi_0$, and $\dot{\gamma}^* = \dot{\gamma}/\phi_0$. Here, M is the mobility ratio, *De* is the Deborah number, and τ^* is the dimensionless surface tension. Henceforth, M_g is referred to as the effective mobility ratio. Furthermore, we may refer to the Capillary number defined as the inverse of the dimensionless surface tension; $Ca = 1/\tau^*$.

3.1.3 Shear Rate in a Hele-Shaw Cell

The three-dimensional velocity field in a Hele-Shaw cell can be estimated from the two-dimensional gap-averaged velocity field calculated from the Darcy's law:

$$\begin{gathered} v_x(x,y,z,t) = F(z)u_x(x,y,t) \\ v_y(x,y,z,t) = F(z)u_y(x,y,t) \\ v_z(x,y,z,t) = 0 \end{gathered} \tag{3.15}$$

where $F(z) = \frac{3}{2}(1 - \frac{z^2}{d^2})$. The strain rate tensor, $\dot{\gamma} = \nabla v + (\nabla v)^T$, for a Hele-Shaw cell becomes

$$\dot{\gamma}_{11} = \left(\frac{\partial v_x}{\partial x} + \frac{\partial v_x}{\partial x}\right) = 2F(z)\frac{\partial u_x}{\partial x}$$

$$\dot{\gamma}_{12} = \left(\frac{\partial v_x}{\partial y} + \frac{\partial v_y}{\partial x}\right) = F(z)\left(\frac{\partial u_x}{\partial y} + \frac{\partial u_y}{\partial x}\right)$$

$$\dot{\gamma}_{13} = \left(\frac{\partial v_x}{\partial z} + \frac{\partial v_z}{\partial x}\right) = F'(z)u_x$$

$$\dot{\gamma}_{22} = 2F(z)\frac{\partial u_y}{\partial y} \tag{3.16}$$

$$\dot{\gamma}_{23} = \left(\frac{\partial v_y}{\partial z} + \frac{\partial v_z}{\partial y}\right) = F'(z)u_y$$

$$\dot{\gamma}_{33} = \left(\frac{\partial v_z}{\partial z} + \frac{\partial v_z}{\partial z}\right) = 0$$

$\dot{\gamma}_{21} = \dot{\gamma}_{12}, \dot{\gamma}_{31} = \dot{\gamma}_{13}, \dot{\gamma}_{32} = \dot{\gamma}_{23}$

The magnitude of the rate-of-strain tensor, $\dot{\gamma}$ can be determined by the second invariant of the strain rate tensor [98]:

$$\dot{\gamma} = \sqrt{\frac{1}{2}\sum_{i=1}^{3}\sum_{j=1}^{3}\dot{\gamma}_{ij}\dot{\gamma}_{ji}} = \sqrt{\frac{1}{2}\left(\dot{\gamma}_{11}{}^2 + \dot{\gamma}_{22}{}^2 + \dot{\gamma}_{33}{}^2 + 2\dot{\gamma}_{12}{}^2 + 2\dot{\gamma}_{13}{}^2 + 2\dot{\gamma}_{23}{}^2\right)}$$

$$= \sqrt{\frac{1}{2}\left(\left(2F(z)\frac{\partial u_x}{\partial x}\right)^2 + \left(2F(z)\frac{\partial u_y}{\partial y}\right)^2 + 2\left(F(z)\left(\frac{\partial u_x}{\partial y} + \frac{\partial u_y}{\partial x}\right)\right)^2 + 2(F'(z)u_x)^2 + 2(F'(z)u_y)^2\right)} \qquad (3.17)$$

If the velocity gradients in x and y directions are ignored assuming they are too small compared to the velocity gradient in z direction, the shear rate may be simplified to:

$$\dot{\gamma} = \sqrt{(F'(z)u_x)^2 + (F'(z)u_y)^2} \qquad (3.18)$$

The shear rate at (x,y) can be determined by gap-averaging $|\dot{\gamma}|$:

$$\frac{1}{2d}\int_{-d}^{+d} |\dot{\gamma}|\, dz = \frac{3}{2d}\sqrt{(u_x)^2 + (u_y)^2} \qquad (3.19)$$

The above gap-averaged shear rate was suggested in several studies [13], [21]. However, the velocity gradients in x and y directions are not ignored in this study because simulation results show they have comparable values near the interface. The shear rate is determined as the second invariant of the strain rate tensor only in the x-y directions without considering the thickness direction. As a result, the present study focuses on the shear rate due to the velocity gradients in the x-y directions nearby the interface.

3.2 Numerical Methods

The governing equations with the jump conditions at the interface can be considered as a two-dimensional elliptic interface problem with a constant coefficient β_1 inside the interface and a non-constant coefficient $\beta_2(\dot{\gamma})$ outside the interface [99]. The equations are solved using a hybrid method introduced by Hou et al. [100] based on a combination of the Fast Immersed Interface Method (FIIM) and the Level Set Method (LSM). IIM consists of a finite difference method to solve Eqs. (3.1) – (3.2) by implementing correction terms at the interface to account for the jump conditions, Eq. (3.3).

3.2.1 Fast Immersed Interface Method

In the Fast Immersed Interface Method, the elliptic interface problem is preconditioned to an equivalent problem [101]. The problem and jump conditions along the interface are

$$\Delta(\beta(x,y)\nabla u) = f(x,y)$$

$$[u] = w(s) \tag{3.20}$$

$$[\beta u_n] = v(s)$$

where f is the source term and the jump comditions across the interface are $[u]$ and $[\beta u_n]$. The solution can be discontinuous along the interface if $w(s) \neq 0$. If $v(s) \neq 0$, there is a source along the interface. In this study, $v(s)$ is zeor and $w(s)$ is the pressure drop due to surface tension. The above problem is preconditioned to an equivalent problem:

$$\Delta u + \frac{\nabla\beta^+}{\beta^+}\cdot\nabla u = \frac{f}{\beta^+}\ (inside\ interface)$$

$$\Delta u + \frac{\nabla\beta^-}{\beta^-}\cdot\nabla u = \frac{f}{\beta^-}\ (outside\ interface) \tag{3.21}$$

$$[u] = w(s)$$

$$[u_n] = g(s)$$

where $g(s)$ is unknown. In the present study, the preconditioned PDE is solved using an iterative method utilizing the fast Poison solver. In order to use the fast Poison solver, terms other than Δu are moved to the right hand side:

$$\Delta u = \frac{f}{\beta^+} - \frac{\nabla\beta^+}{\beta^+} \cdot \nabla u \; (outside\ interface)$$

$$\Delta u = \frac{f}{\beta^-} - \frac{\nabla\beta^-}{\beta^-} \cdot \nabla u \; (inside\ interface) \tag{3.22}$$

The iteration starts with the case where β^+ and β^- are constant. The right hand side of the equation is calculated from the solution of the previous iteration and treated as constant. The iteration continues until the relative difference of the current and previous solutions is less than 1.0E-04. The correction term in each iteration is assumed to be the same as the correction term of the first iteration where β^+ and β^- are constant. As a result, the fast immersed interface method in the present study has two iterations which are the iteration for solving the preconditioned PDE with non-constant coefficient β and the GMRES (generalized minimal residual method) iteration to find a solution for the preconditioned PDE which satisfies the jump contion of the original problem.

Interface derivatives of the jump conditions are required to determine the correction term. A least square interpolation scheme is used to evaluate interface derivatives, and it is recommended to use 9~12 interface points for the interpolation [99]. The least square interpolation scheme is tested to determine how many points are required to have accurate interface derivatives. In the present study, the jump condition $w(s)$ is a pressure drop at the interface due to surface tension which equals surface tension τ times the curvature κ. The curvature at a point is determined using the signed distance level set function Ø which defines an interface implicitly:

$$\kappa = -\frac{\emptyset_{xx}\emptyset_y^2 - 2\emptyset_{xy}\emptyset_x\emptyset_y + \emptyset_{yy}\emptyset_x^2}{(\emptyset_x^2 + \emptyset_y^2)^{3/2}} \tag{3.23}$$

The dimensionless curvature is -1 at the points on a circular interface. The negative curvature means the interface is concave towards the center. A circular interface of a radius 0.5 is used, and the first and second derivatives of the pressure drop, $w(s)$ along the interface are evaluated using different numbers of interface points. The circular interface is represented using a level set function, and the points on the interface are determined as normal projections of the adjacent grid points to the interface. The first and second interface derivatives of the pressure drop should be 0 because the curvature of a circle is constant and does not change along the interface. The first interface derivatives of the pressure drop, $w(s)$ are shown in Figure 3.2. The results are accurate when more than 10 interface points are used for the interpolation.

(a) (b) (c)

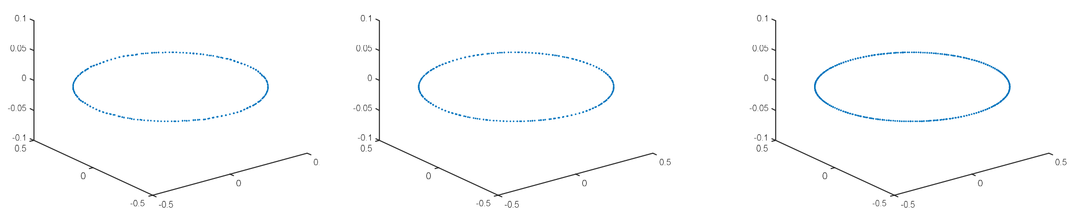

Figure 3.2 *The first interface derivatives $w'(s)$ of a circular interface determined from (a) 2-6 interface points, (b) 10-16 interface points, and (c) 16-23 interface points.*

Figure 3.3 shows the second interface derivatives of the pressure drop. As shown in Figure 3.3, the second derivatives from 2-6 interface points are not accurate, and the results become accurate when using more than 16 interface points.

(a) (b) (c)

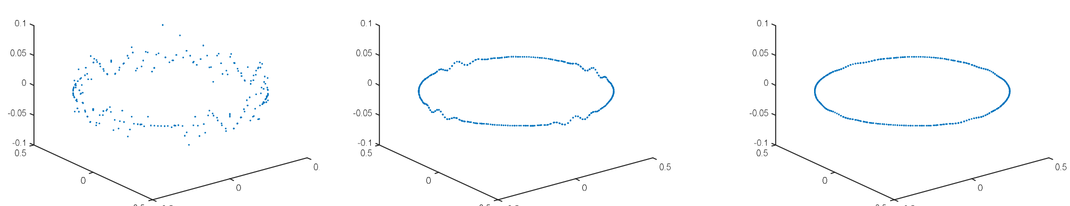

Figure 3.3 *The second interface derivatives $w''(s)$ of a circular interface determined from (a) 2-6 interface points, (b) 10-16 interface points, and (c) 16-23 interface points.*

3.2.2 Level Set Method

In the LSM used in this study, the interface is defined implicitly as an iso-contour of a signed distance function which gives the shortest distance to the interface for a given point in the domain [102]. The signed distance function is defined as:

$$\emptyset(\vec{x}) = \begin{cases} 0 \text{ on the interface} \\ d(\vec{x}) \text{ in the exterior region} \\ -d(\vec{x}) \text{ in the interior region} \end{cases} \tag{3.24}$$

where $d(\vec{x})$ is the shortest distance to the interface. The level set function satisfies [103]

$$\emptyset_t + \nabla\emptyset \cdot \boldsymbol{U} = 0 \tag{3.25}$$

where $\boldsymbol{U} = \frac{d\vec{x}}{dt}$. The position of the interface is tracked by solving the above equation in the Level Set Method. The initial condition of the signed distance level set function is a circle with a radius of R_0:

$$\emptyset(x, y, t = 0) = \sqrt{x^2 + y^2} - \mathrm{R}_0 \tag{3.26}$$

When a speed in the outward normal direction, V_n is given, the equation becomes:

$$\emptyset_t + |\nabla\emptyset| V_n = 0 \tag{3.27}$$

The time change of the level set functions can be tracked by solving equation (3.25) or (3.27). In the present study, the Level Set Method Library (LSMLIB) is used for the simulation program [104].

The LSMLIB is tested with simple 2D shapes such as a circle and a V shape by moving the interfaces and calculating the inside areas. A signed distance function can be defined by assigning the shortest distance to the interface for every grid point. It has a negative distance for the points inside the interface and a positive one for the points outside the interface. Several interfaces can be combined as a union or an intersection. For example, a triangle can be defined as an intersection of three line interfaces. Four simple shapes are defined in level sets, and they are visualized as 0 contour plot in Matlab and shown in Figure 3.4.

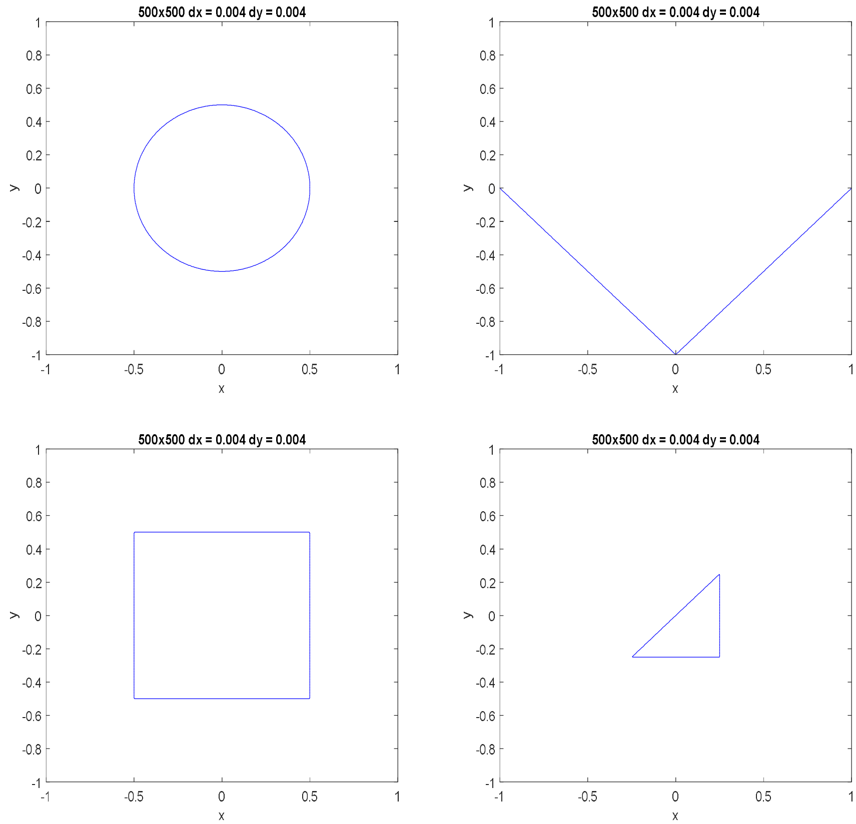

Figure 3.4 *Zero contour plot of level sets for simple 2D shapes*

The interior area of an interface can be calculated by evaluating the following integral over the entire grid points [102].

$$\int \big(1 - H(\emptyset)\big) dA \tag{3.28}$$

$H(\emptyset)$ is a Heaviside function. $H(\emptyset)$ can be calculated using a first-order accurate smeared-out approximation [102]

$$H(\emptyset) = \begin{cases} 0 & \emptyset < -\epsilon \\ \dfrac{1}{2} + \dfrac{\emptyset}{2\,\epsilon} + \dfrac{1}{2\pi}\sin\left(\dfrac{\pi\emptyset}{\epsilon}\right) & -\epsilon \le \emptyset \le \epsilon \\ 1 & \epsilon < \emptyset \end{cases} \tag{3.29}$$

where a typical value of ϵ is $1.5\Delta x$. The calculated areas are shown in Table 3.1.

As can be seen in Table 3.1, the % error is not decreased significantly when the grid space is reduced from 0.01 to 0.004. This indicatess that the approximation of the areas is first order accurate.

***Table 3.1** Calculated areas of simple shapes and % error*

Shape	Actual Area	Approximation			
		dx=dy=0.004	% Error	dx=dy=0.01	% Error
Circle	0.785398	0.785413	0.002	0.785492	0.012
Rectangle	1	1.000023	0.002	1.000146	0.015
Triangle	0.125	0.125041	0.033	0.125247	0.198
V shape (upper area)	3	2.995995	0.133	2.989972	0.334

With a constant normal speed, equation (3.27) becomes

$$\emptyset_t + a|\nabla\emptyset| = 0 \tag{3.30}$$

where a is a constant normal speed. The spacial derivative, $\nabla\emptyset$ is approximated using a second-order accurate HJ ENO(Hamilton-Jacobi essentially non-oscillatory) following upwind differencing. In HJ ENO, Newton polynomial interpolation is used to find the smoothest fit to $\emptyset$ and then differentiate to get $\emptyset_x$ [102]. The discretization of $\emptyset$ with respect to time is performed using a second order accurate TVD RK (total variation diminishing Runge-Kutta) method. In the second order TVD RK, the forward difference operation for the time is performed two times to get $\emptyset^{n+1}$and $\emptyset^{n+2}$, and the final $\emptyset^{n+1}$ is determined by averaging $\emptyset^{n}$ and $\emptyset^{n+2}$ [102]. The simulation results for the movement of the four simple shapes are presented below.

The inside area of the circle has negative level set values. The interface moves outward with a positive constant normal speed of 0.2 as shown in Figure 3.5.

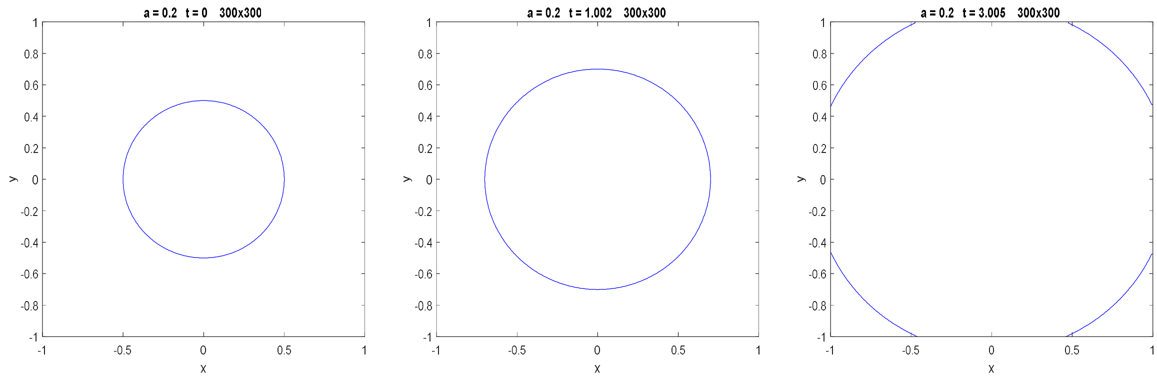

Figure 3.5 *Propagation of a circular interface with a constant positive normal speed, a = 0.2*

The interface moves inwards with a negative constant normal speed of -0.2 as shown in Figure 3.6.

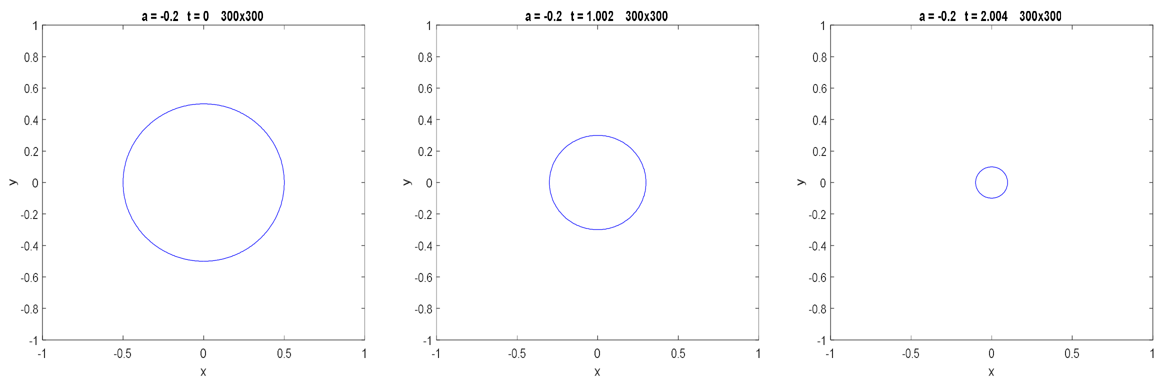

Figure 3.6 *Propagation of a circular interface with a constant negative normal speed, a = -0.2*

The inside area of the rectangle has negative level set values. The interface moves outward with a positive constant normal speed of 0.2 as shown in Figure 3.7. The corners become a rarefaction fan as the interface moves outwards. This can be explained by an entropy condition that says no new information can be created during the propagation of interface [103].

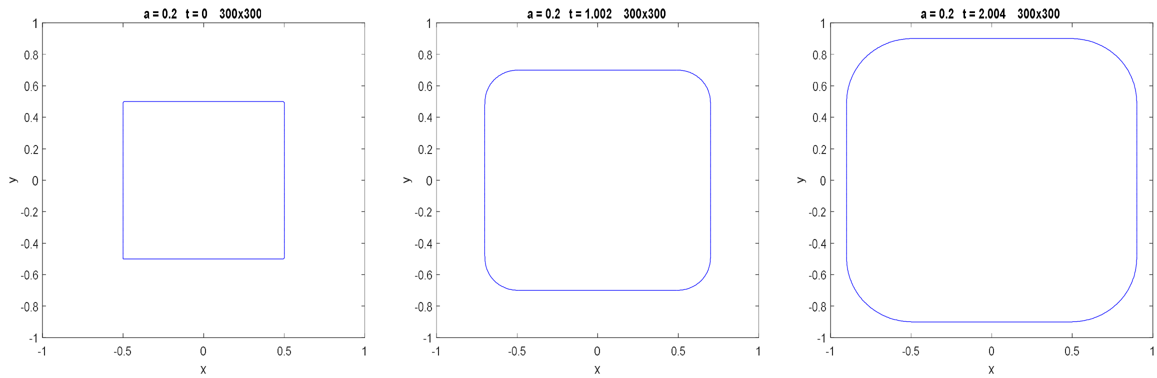

Figure 3.7 *Propagation of a rectangular interface with a constant positive normal speed, a = 0.2*

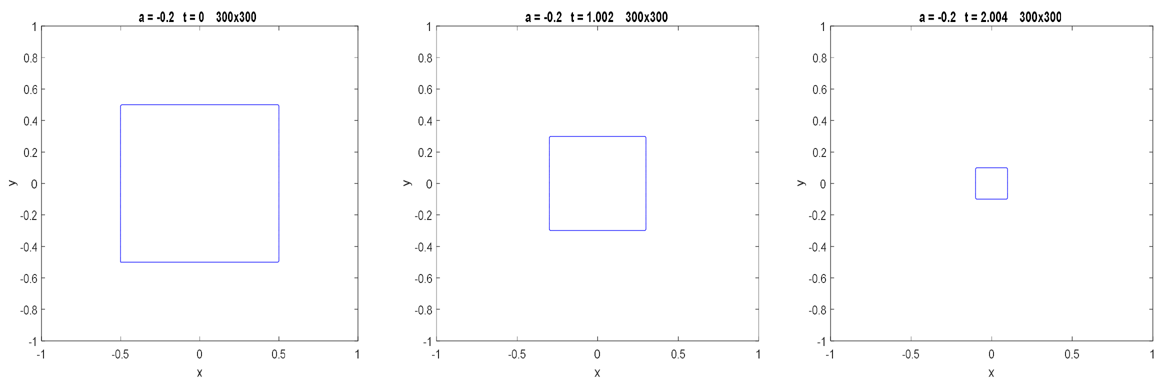

Figure 3.8 *Propagation of a rectangular interface with a constant negative normal speed, a = -0.2*

The corners remain during the shrinkage of the rectangular interface as shown in Figure 3.8. However, the interface information at the corners are lost. The upper area of the V shape has negative level set values, and the movement of the V shape is shown in Figure 3.9. The interface moves downwards with a positive constant normal speed of 0.2.

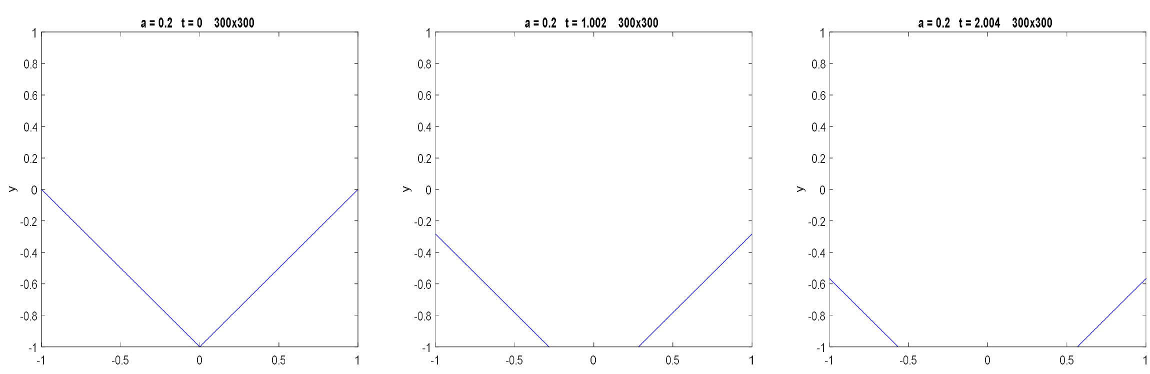

Figure 3.9 *Propagation of a V interface with a constant positive normal speed, a = 0.2*

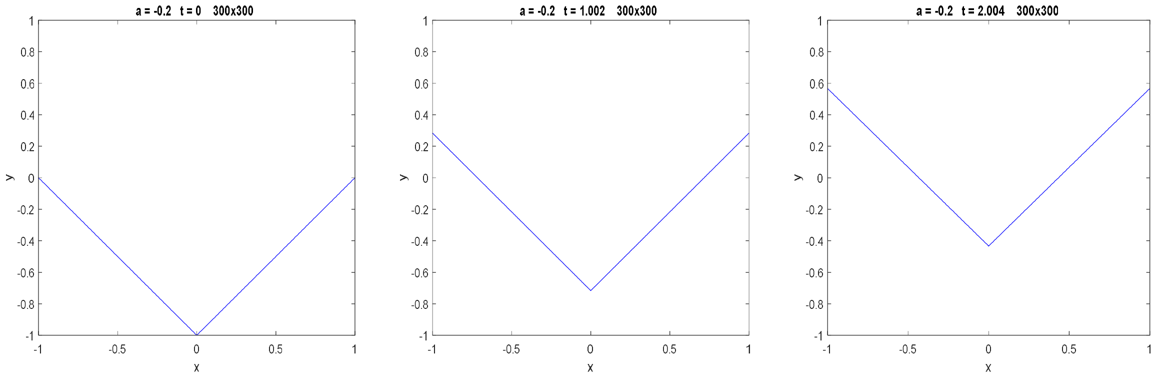

Figure 3.10 *Propagation of a V interface with a constant negative normal speed, a = -0.2*

As shown in Figure 3.10, level set values at the lower and upper x boundaries are linearly extrapolated as the interfaces move inward. The outward and inward movements of the triangle is shown in Figure 3.11 and 3.12 respectively. The inside area has negative level set values. The corners become a rarefaction fan as the interface moves outwards.

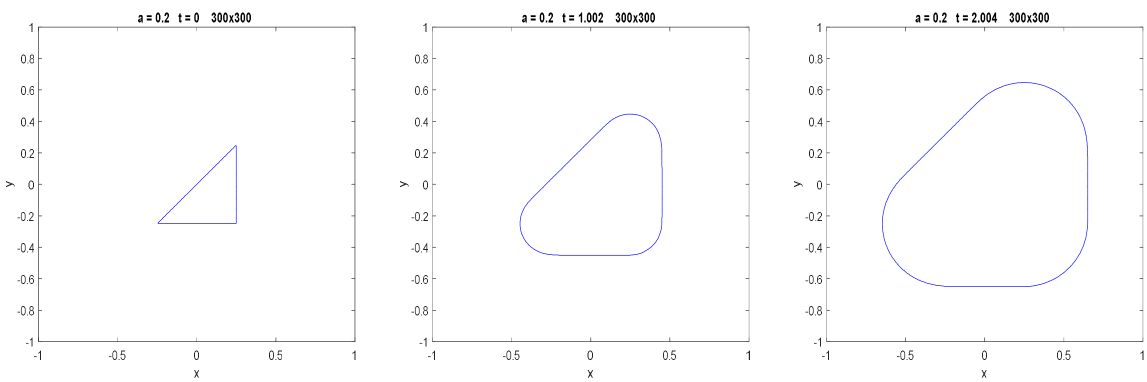

Figure 3.11 *Propagation of a triangular interface with a constant positive normal speed, a = 0.2*

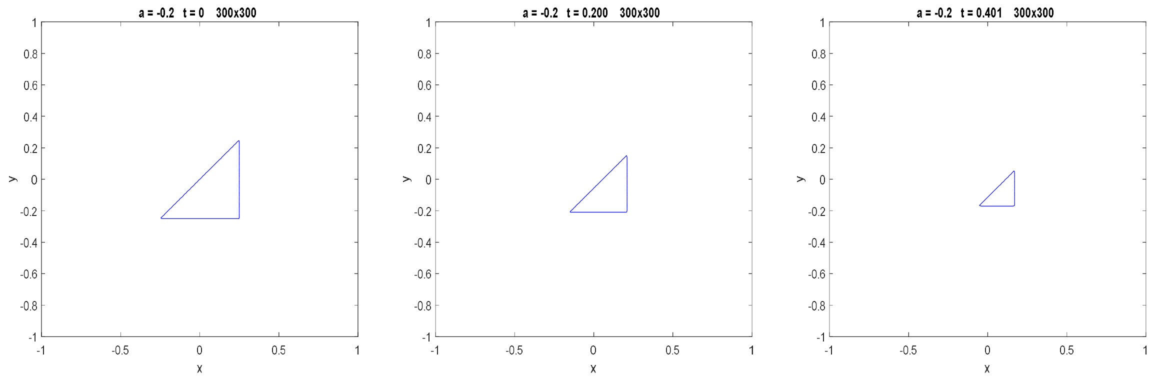

Figure 3.12 *Propagation of a triangular interface with a constant negative normal speed, a = -0.2*

3.2.3 FIIM and LSM

In the present study, the implementation of the FIIM is based on the FIIM_LEVEL package where the FIIM uses a signed distance level set function to represent an interface [105]. The pressure solution of the Hele-Shaw flow is obtained using the FIIM, and the normal velocity field is computed from the pressure solution following the methods suggested by Hou et al. [80]. For the regular grid points outside the interface, whose standard five-point stencil is not cut through by the interface, the normal velocity can be calculated directly by

$$u_n = -\beta p_n = -\beta \nabla p \cdot \mathbf{n} \tag{3.31}$$

where **n** is the unit normal vector calculated from the signed distance level set function. For the irregular grid points outside the interface, the normal velocity is interpolated using normal velocities from the two closest points on the interface and one close regular grid point on the same side. For the grid points inside the interface which are close to the interface, the normal velocities are calculated by just extending the normal velocities on the interface. Once the normal velocity field is determined from the pressure solution, the interface is moved by solving the Equation (3.27) with the normal velocity field.

3.2.4 Numerical Validation

Prior to presenting the results of the numerical simulations, the convergence of the numerical scheme and the validation of the code are briefly discussed. The number of grid points in the domain was varied to ensure the convergence of the numerical simulations. A representative result is presented in Figure 3.13 for a Newtonian displacement with *M*=100 and *Ca*=130 where time sequences ($t^{*}\epsilon[0,9]$) of interfacial contours are depicted for different grid sizes. It is clear that the overall finger structures as well as the number fingers are not changed with increasing grid size, *m*. The convergence has also been ascertained through the values of the base and the tip radius (at t*=9), defined as the radial location of the closest and farthest points of the interface from the injection centre.

(a) (b) (c)

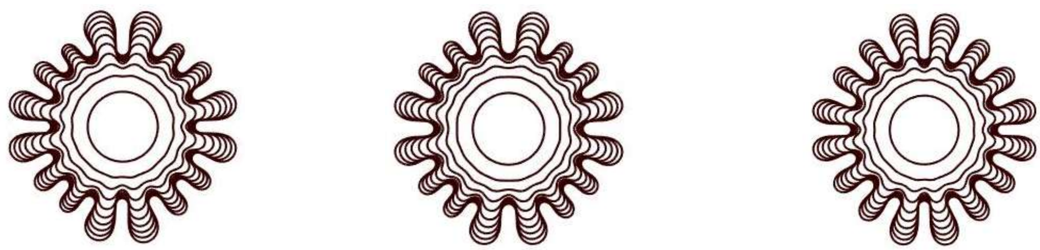

(a)	(b)	(c)
Base Radius = 2.03	Base Radius = 2.07	Base Radius = 2.07
Tip Radius = 3.37	Tip Radius = 3.42	Tip Radius = 3.42

Figure 3.13 *Numerical Convergence of fingers with spatial resolution ($m \times m$) for (a) $m = 280$, (b) $m = 300$, and (c) $m = 360$ at $M = 100$, $Ca = 130$, $n = 1.0$, and $t^{*} = 0$ to 9.*

(a) (b) (c)

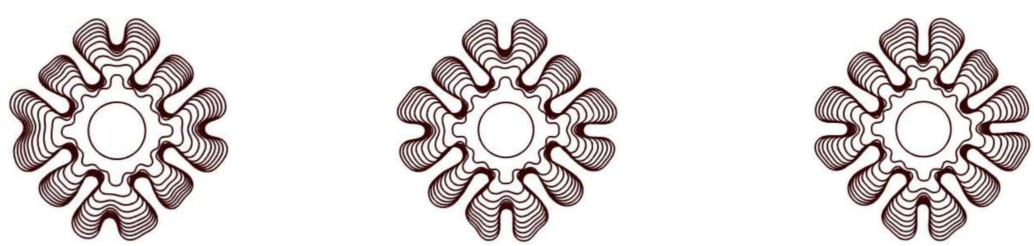

(a)	(b)	(c)
Base Radius = 1.77	Base Radius = 1.76	Base Radius = 1.77
Tip Radius = 3.98	Tip Radius = 4.10	Tip Radius = 4.10

Figure 3.14 *Numerical Convergence of fingers with spatial resolution ($m \times m$) for (a) $m = 280$, (b) $m = 300$, and (c) $m = 340$ at $M = 100$, $Ca = 70$, $n = 0.9$, $De = 0.25$, and $t^{*} = 0$ to 15.*

Similar contours are shown in Figure 3.14 in the case of a non-Newtonian displacement with *M*=100, *Ca*=70, *n*=0.9, De=0.25 and different grid sizes. It is also clear here that the overall finger structures and the number of fingers as well as the base and tip radii virtually do not change as *m* is increased. More details on the numerical technique and validation can be found in [85], [86]. In what follows, results are presented for shear-thinning fluids followed by those for a shear-thickening one.

3.2.5 Finger Structures of non-Newtonian Displacements

In order to establish the direct relationship between the finger structures and the rheological behaviour of the non-Newtonian fluids, i.e. their shear-dependent viscosity, numerous simulations were carried out for fluids with different values of the Deborah number and power-law index but that have identical or similar viscosity profiles. It was found that in all cases, the finger structures are virtually identical, showing the direct relationship between the interfacial instability and the rheological behaviour of the displaced non-Newtonian fluids.

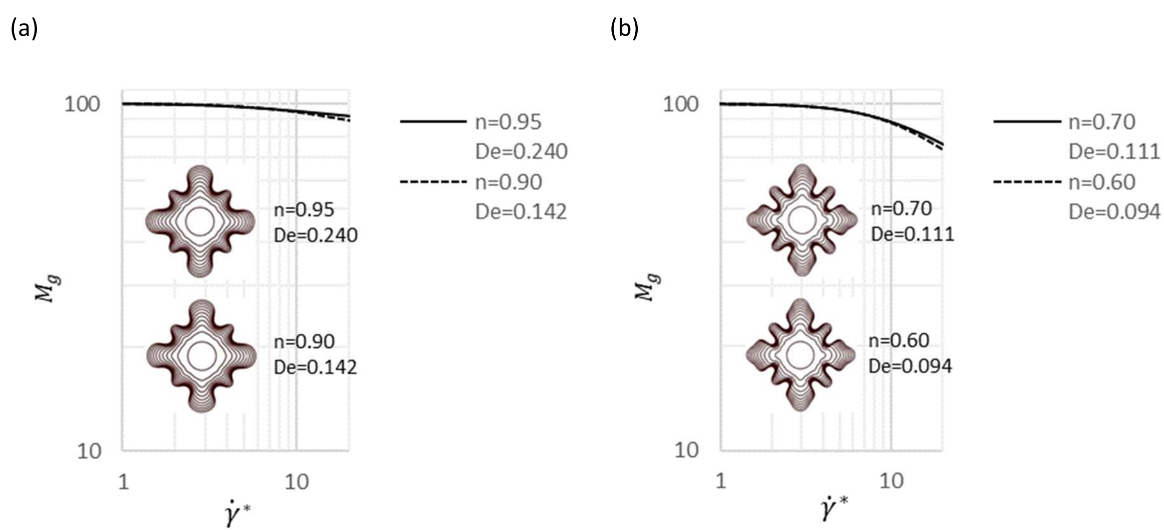

Figure 3.15 *Effective mobility ratio M_g versus shear rate $\dot{\gamma}^*$ for the pairs showing very similar finger structures.*

Figure 3.15 illustrates this result, where the effective mobility ratio M_g profiles versus shear rate $\dot{\gamma}^*$ are depicted along with the corresponding finger structures, for selected pairs of *De* and *n*. It is clear that combinations of (*De, n*) that result in the same viscosity profile, lead to virtually indistinguishable fingering patterns.

CHAPTER 4

RESULTS: NON-NEWTONIAN FLOW DISPLACEMENTS

In this chapter, immiscible flows that involve radial displacements of shear-thinning or shear-thickening non-Newtonian fluids by a Newtonian fluid in homogeneous porous media are examined. The flow displacements are characterized qualitatively through time sequences of the interfacial contours as well as quantitatively using the effective fingers number k_{eff} obtained from Fourier spectra of the interface and the finger area density, FAD.

4.1 Shear-Thinning Flow Displacements

In this section, the effects of the two rheological parameters De and n are analyzed in the case of shear-thinning (pseudo-plastic) fluids. The results are presented by first examining interfacial contours and then through a quantitative analysis.

4.1.1 Interfacial Contours

Figure 4.1 depicts time sequences of the interface for a power-law index, $n = 0.8$ and different values of the Deborah number, from zero to 0.50. For very small values of *De*, the instability is virtually identical to its Newtonian counterpart exhibiting eight dominant fingers at the interface. As the Deborah number is further increased and the flow moves to a stronger non-Newtonian regime, the finger structures start gradually to change. In a first regime, the instability and in particular fingers' tip-splitting is attenuated with increasing *De* ultimately resulting in mainly four developed fingers instead of the eight ones observed in the Newtonian (*De=0*) and very small Deborah number cases. This least unstable interface is observed for *De≈0.07*. The delay and ultimately full suppression of tip-splitting effects of weak shear-thinning fluids were also observed in previous studies [19], [20]. This trend is however reversed when *De* is further increased resulting in the emergence and development of new fingers that result in more complex interfacial structures involving a variety of fingers' growth mechanisms such as multiple-tip splitting and side branching. It should be also noted that with increasing Deborah number, interfacial instabilities tend to develop earlier in the flow and the breakthrough time decreases.

$De = 0.00$ $De = 0.03$ $De = 0.05$ $De = 0.06$

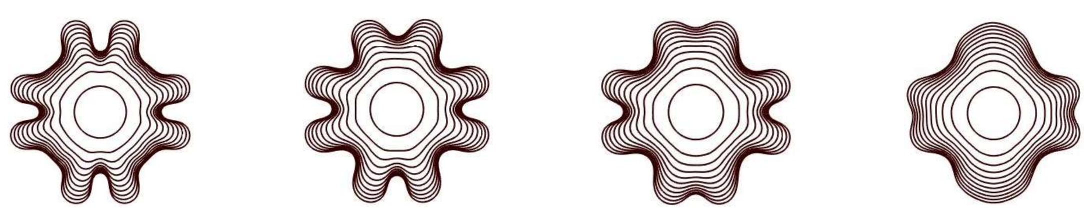

$De = 0.07$ $De = 0.09$ $De = 0.15$ $De = 0.16$

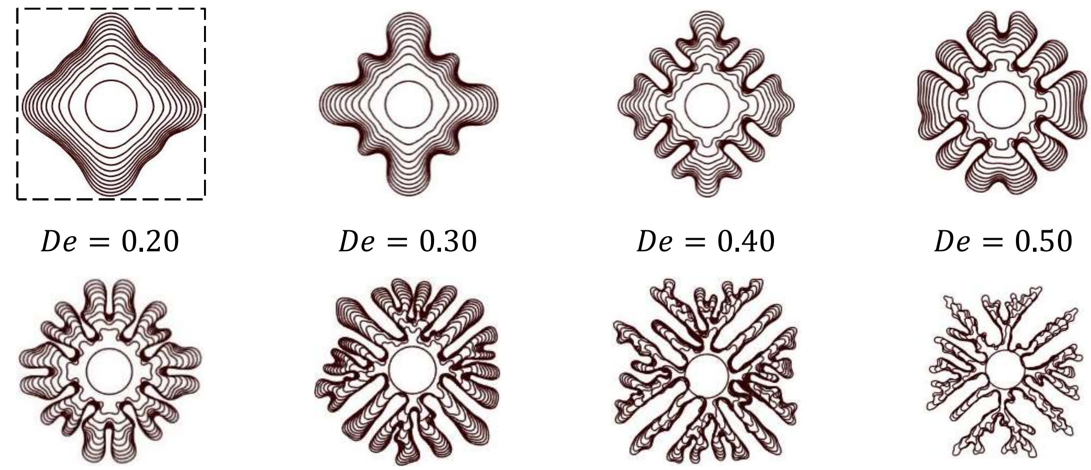

Figure 4.1 *Time sequences of the interface for* $n = 0.8$ *and different values of the Deborah number over* $t^* = 0\ to\ 15$ *or breakthrough.*

Similar results for a larger value of the power-law index; *n=0.9*, are shown in Figure 4.2. The trends are qualitatively similar to the ones reported for *n=0.8*, with an initial stage of attenuation of the instability followed by a trend change that in this case takes place at a larger value of the Deborah number (*De≈0.09*). It should be noted that in this case, the effects of attenuation of the instability also occur at a larger value of *De*.

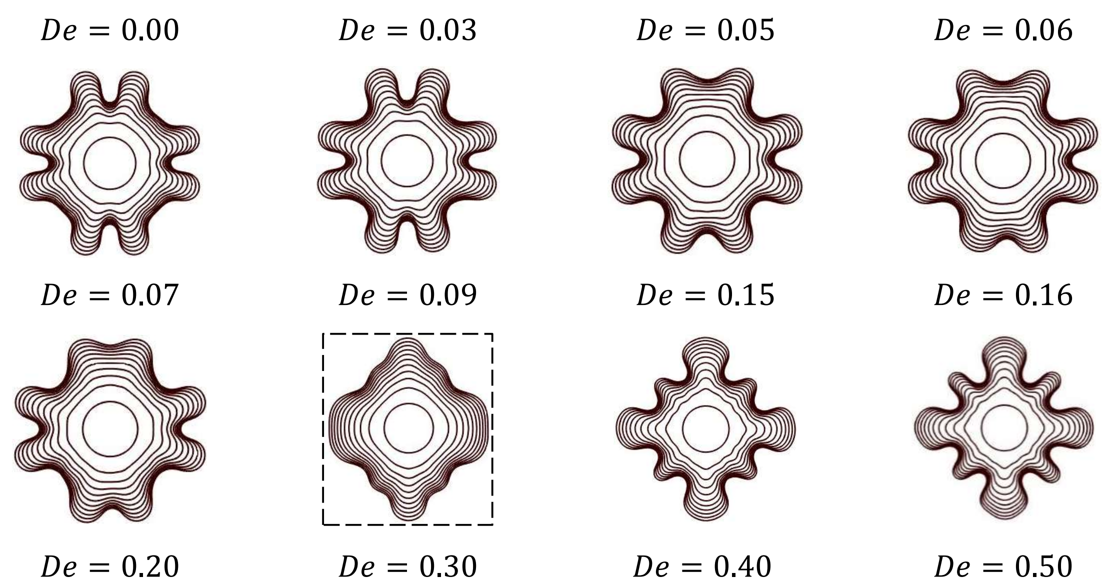

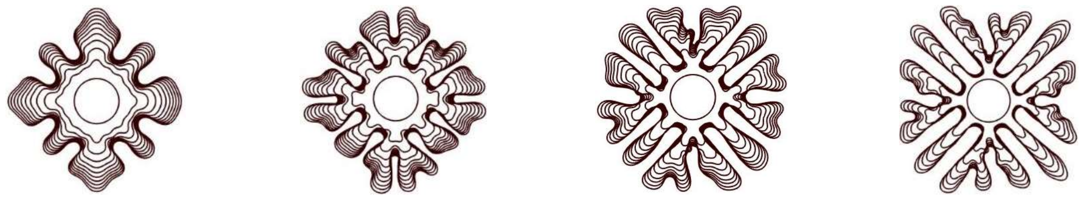

Figure 4.2 *Time sequences of the interface for $n = 0.9$ and different values of the Deborah number over $t^* = 0\ to\ 15$ or breakthrough.*

The effects of the power-law index *n* which measures the intensity of shear-thinning are presented in Figure 4.3 for $De = 0.15$. The results indicate that as n decreases, the shear-thinning effects get stronger, and the finger structures change. In particular, tip-splitting is delayed with a slight decrease of *n* and totally suppressed with a further decrease of *n*. These trends however change when the power-law index is decreased below a critical value, $n \approx 0.95$ with new fingers developing and involving more complex growth mechanisms that ultimately result in more intricate interfacial morphologies.

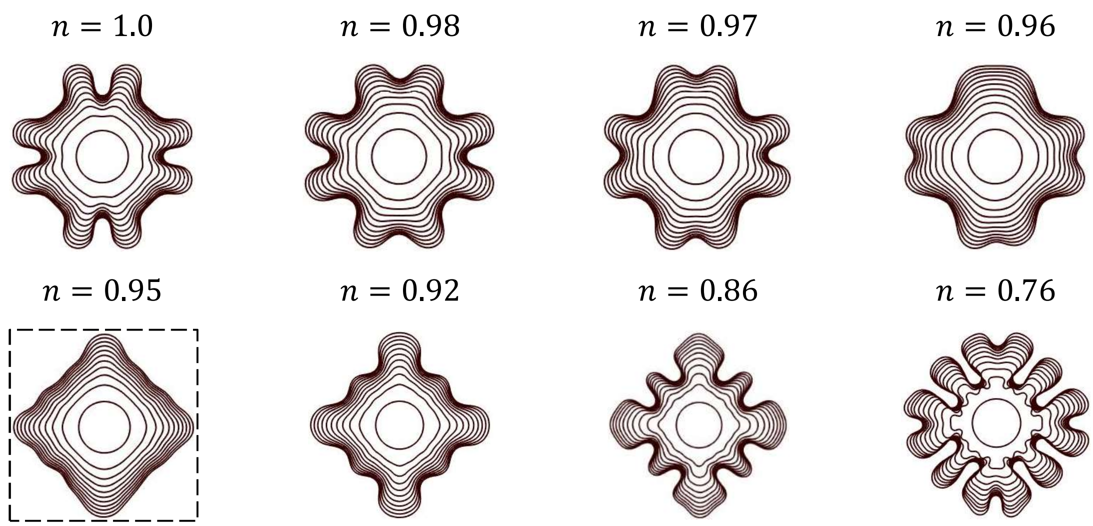

Figure 4.3 *Time sequences of the interface for $De = 0.15$ and different values of the power-law index over $t^* = 0\ to\ 15$ or breakthrough.*

4.1.2 Quantitative Analysis

The previous results indicate that changes in the rheological characteristics of the displaced fluid induce major changes in the interfacial instability and the finger structures, and these changes do not seem to be monotonic. In order to further characterize the evolution of the interfacial instability, a number of quantitative criteria consisting of the effective number of fingers and the finger area density, will be adopted.

The number of fingers of the interface at any given time is determined using the Fourier spectrum of the interface [86]. The interface is considered as points of a radius versus angle function, and its discrete Fourier transform is determined. The effective number of fingers k_{eff} is obtained as:

$$k_{eff} = \frac{\sum_k |F(k)|^2 k}{\sum_k |F(k)|^2} \tag{4.1}$$

where $F(k)$ is the Fourier transform and k is the wavenumber in the transform space.

(a) $k_{eff} = 4.08$ $FAD = 0.66$

(b) $k_{eff} = 11.18$ $FAD = 0.63$

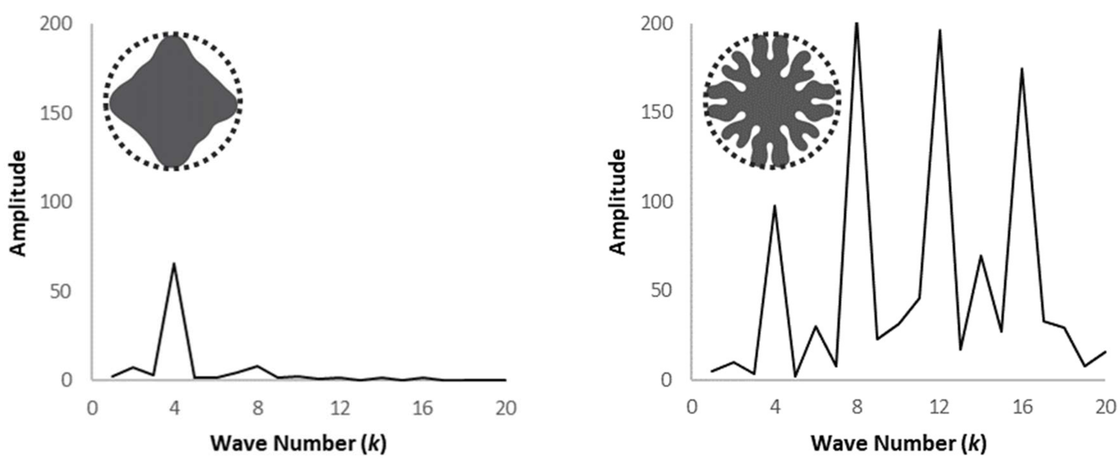

Figure 4.4 *Fourier transform spectra of interfaces, the effective number of fingers k_{eff} and the finger area density (FAD) for (a) $De = 0.07$ and (b) $De = 0.20$ for $n = 0.8$ and $t^* = 15$.*

Figure 4.4 illustrates typical examples for the variation of the Fourier's amplitude with the wavenumber at $t^* = 15$, for *n=0.8* and two values of the Deborah number, corresponding to results shown in Figure 4.1. In the case $De = 0.07$, the interface exhibits four dominant fingers, with additional four side small protrusions. This qualitative characterization of the interface is well reflected by the Fourier spectrum (Figure 4.4-a) and is captured by the numerical value of the effective number; $k_{eff} = 4.08$. For $De = 0.20$, the interface consists of four dominant fingers separated by four less developed shielded fingers, resulting in a total of eight major fingers. These are captured by the two peaks at wavenumbers $k = 4$ and $k = 8$. The third peak at $k = 12$ reflects the tip splitting of the four main fingers (Figure 4.4-b) while the one at $k = 16$ accounts for all the fingers from the tip splitting of the four main fingers and the four shielded ones. The small peak at $k = 14$ reflects the fact that the two sub-fingers from the tip splitting of the two shielded fingers are less developed than the others. The effective fingers number is in this case $k_{eff} = 11.18$.

A second quantitative criteria to characterize the instability at the interface is the finger area density; *FAD*, defined as the ratio of the fingering area to $\pi {r_{tip}}^2$ where r_{tip} is the radius of the point on the interface farthest from the centre of the domain [85]. A unit value of *FAD* represents the case of a stable circular interface, and the more complex the finger structures the smaller the value of *FAD*. Values of *FAD* are indicated in Figure 4.4 for *n=0.8* and $De = 0.07 \text{ and } 0.20$ and reflect that more instable interface result for the latter value.

The effective number of fingers and the finger area density are henceforth used to characterize and quantify the development of the instability at the interface as the rheological properties of the non-Newtonian fluid are changed.

Figure 4.5 depicts the variations of k_{eff} and *FAD* with time for different values of the Deborah number in the case *n=0.8*. The Newtonian reference case is shown in solid line while the non-Newtonian cases are depicted using symbols. Furthermore, for clarity not all values of *De* are included, and only those that capture the main interesting trends are shown. Both k_{eff} and *FAD* vary with time but tend to reach a plateau at later times. Furthermore, except for the early stages of the flow where the number of fingers may vary non-monotonically with time, the subsequent evolution is monotonic in all examined values of *De* and levels off late in the flow (Figure 4.5-a).

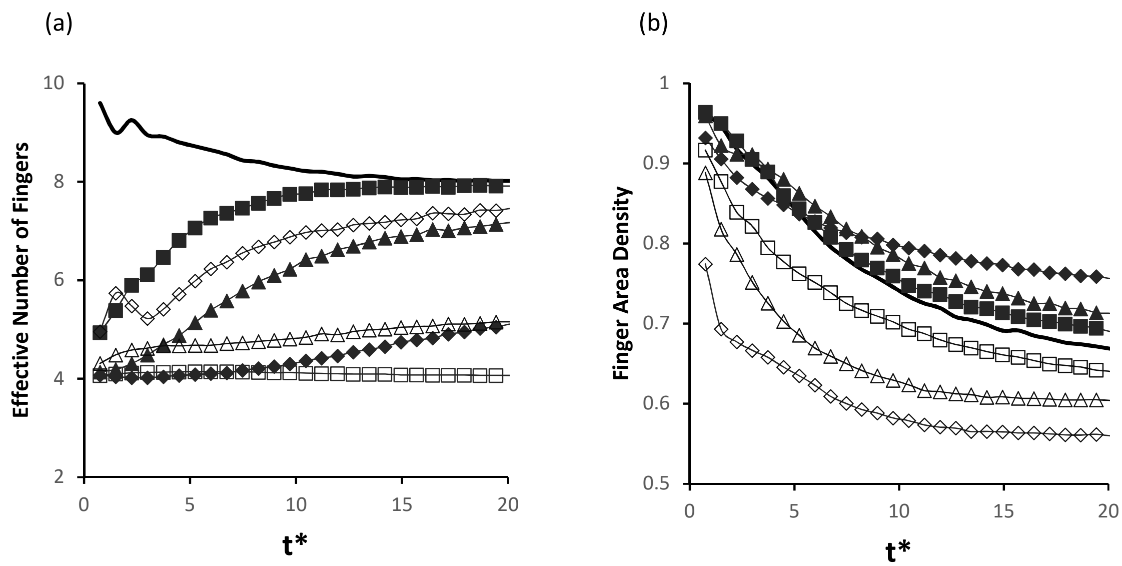

Figure 4.5 *(a) Effective number of fingers and (b) Finger area density versus time for n=0.8 and different values of De. De=0.0(▬), 0.03(■), 0.05(▲), 0.06(◆), 0.07(□), 0.09(△), 0.15(◇).*

A close examination of the variation of the effective number of fingers with De at later times, illustrate clearly the non-monotonic variation of k_{eff} with De. Initially the number of fingers tends to decrease as De is increased, followed by a reversal of trend where k_{eff} increases with increasing De. The minimum number of fingers is about four and is reached for $De \approx 0.07$. Similar conclusions can be drawn for the finger area density where a plateau is observed late in the flow. The variation of *FAD* with *De* at such times is also non-monotonic, starting with an initial increasing trend followed by a decreasing one as the Deborah number is increased, with a maximum attained at $De \approx 0.06$. Note that *FAD* tends in general to decrease with time, reflecting more unstable interfaces and intricate finger structures as the flow progresses. Furthermore, the effective number of fingers of the non-Newtonian fluids ($De > 0$) are systematically smaller than their Newtonian counterpart, while their *FAD* may be smaller or larger than that of the Newtonian flow.

The results of this quantitative analysis confirm the previous observations from the interfacial contours regarding the existence of a turning point in the evolution of the interfacial morphology that occurs at a critical value of the Deborah number; $De_c \approx 0.07$ in the case *n=0.8*.

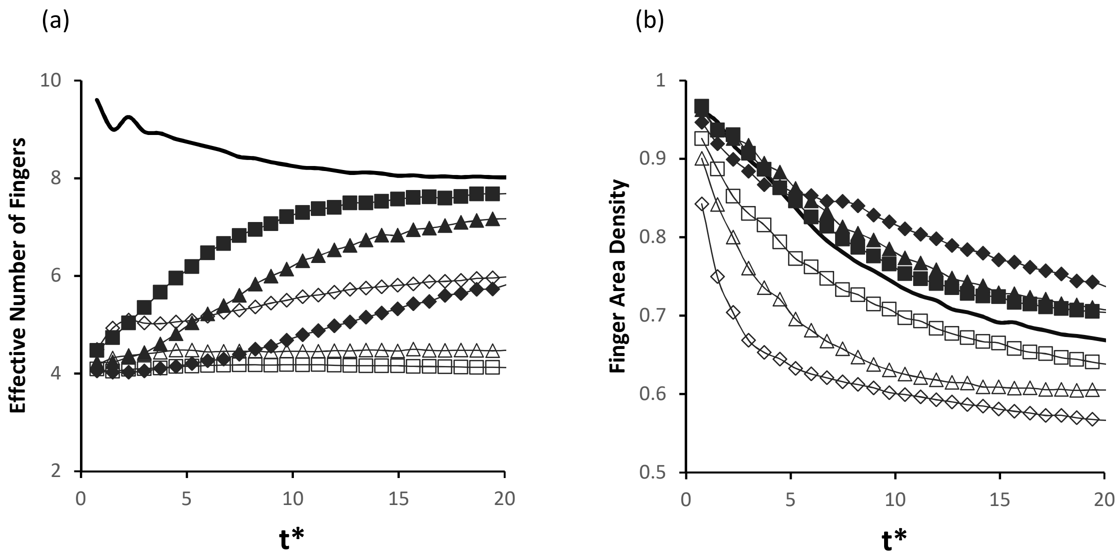

Figure 4.6 *(a) Effective number of fingers and (b) Finger area density versus time for De=0.15 and different values of n. n=1.00(▬), 0.98(■), 0.97(▲), 0.96(◆), 0.95(□), 0.92(△), 0.86(◇).*

The variations of k_{eff} and *FAD* with time for different values of the power-law index *n* at fixed $De = 0.15$ lead to similar conclusions. In particular, the trends reflect well that the flow instability increases with time, and both k_{eff} and *FAD* tend to level off at large times (Figure 4.6). At such late-times, the variations with *n* of both k_{eff} and *FAD* are non-monotonic revealing the existence of a critical power-law index value $n_c \approx 0.95$ around which the variations with *n* change trends (Figure 4.6). Again, these results concord with the observations based on the interfacial contours depicted in Figure 4.3. Note that k_{eff} of the Newtonian displacement is systematically larger than those of the shear-thinning flows (*n<1*) while the finger area density is smaller than those for weakly shear-thinning fluids, but becomes larger for smaller *n*.

The previous quantitative analyses indicate that changes with time of both the number of fingers and the area density level off at late-times and both quantities have a constant value if one considers a long enough time. All subsequent results and discussion will focus on the behaviour of the flow at such long times.

4.1.3 Critical Deborah number

The previous results indicate that for given values of the mobility ratio *M*, Capillary number *Ca* and power-law index *n*, there is a critical Deborah number De_c that characterizes the non-Newtonian displacement. De_c is defined as the Deborah number at which the effective number of fingers is the smallest. It can also be determined from the value at which the finger area density reaches its first maximum. In this section, exact values of De_c and their dependence on the other dimensionless groups are presented;

$$De_c = \mathfrak{I}_p(M, Ca, n)$$

In order to determine De_c, a large number of simulations were carried out by varying the Deborah number for fixed *M*, *Ca* and *n* and determining the values of the effective number of fingers and the area density.

Figure 4.7 shows the variations of k_{eff} and *FAD* with De for different values of the power-law index and for *M*=100 and *Ca*=70. For a given value of the power-law index, k_{eff} initially decreases with increasing De. This decrease in k_{eff} results in an almost smooth though not perfectly circular interface which explains the corresponding initial increase of *FAD*. Further increase in De leads to the development of new small protruding fingers that distort the interface. As a result, k_{eff} starts to increase while *FAD* decreases.

It is clear that the number of fingers reaches a minimum at the critical Deborah number De_c, that seems to decrease with decreasing power-law index, or equivalently with stronger shear-thinning behaviour (Figure 4.7-a). Similarly, the finger area density reaches its maximum at De_c (Figure 4.7-b).

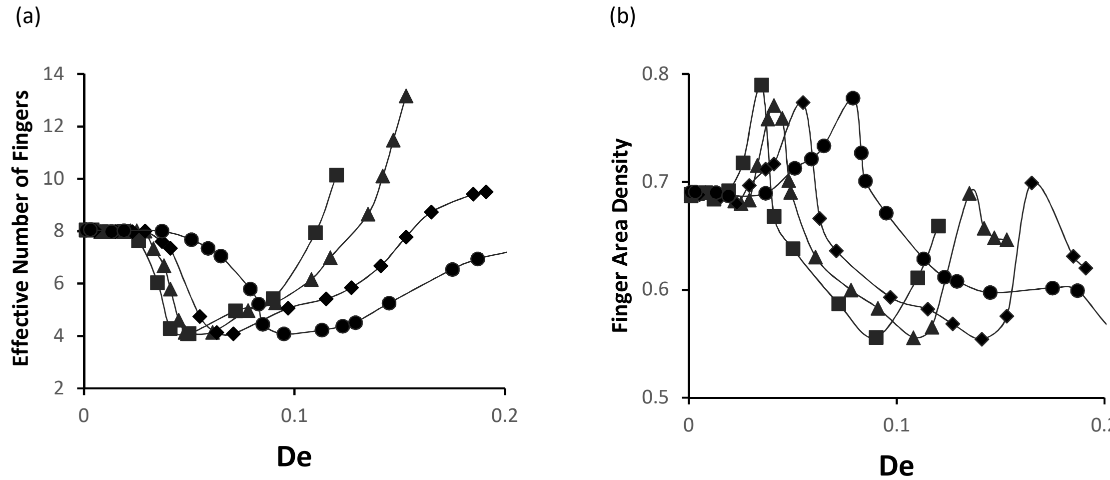

***Figure 4.7** (a) Effective number of fingers and (b) Finger area density versus De for different values of n at t*=15. n=0.60(■), 0.70(▲), 0.80(◆), 0.90(●).*

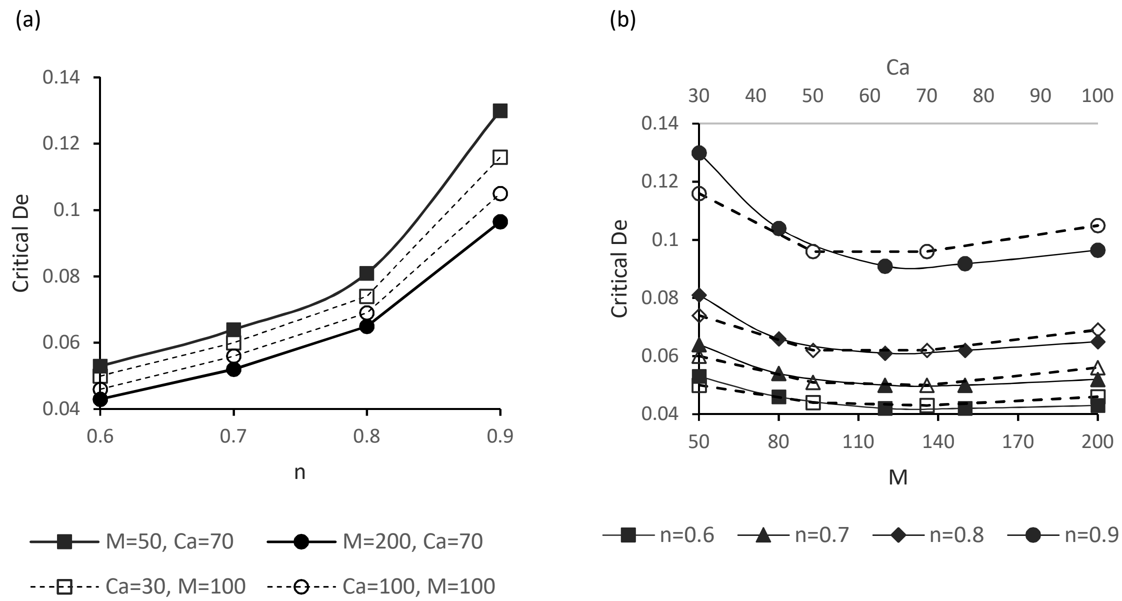

***Figure 4.8** Critical Deborah number versus (a) n for different values of M and Ca, (b) M and Ca for different values of n, filled symbols for M (Ca=70) and empty symbols for Ca (M=100).*

In what follows, the dependence of the critical Deborah number on the mobility ratio *M* and the Capillary number *Ca*, is discussed. Figure 4.8 depicts the variation of De_c with *n* for different values of the mobility ratio and the Capillary number and with *M* and *Ca* for different values of the power-law index. For any given values of the mobility ratio and the Capillary number,

De_c increases monotonically with increasing power-law index, i.e. with weaker shear-thinning behaviour (Figure 4.8-a). Though the figure shows results only for four values of (*M*, *Ca*), this trend was observed consistently for all considered values of *M* and *Ca*. Furthermore, De_c decreases with increasing mobility ratio for fixed *n* and *Ca*. However the effects of *M* on De_c tend to subside at larger values of the mobility ratio, implying that there is an asymptotic behaviour for large *M* (Figure 4.8-b). It should however be noted that the effect of the mobility ratio is non-monotonic. At small *M*, the critical Deborah number decreases as *M* increases, reaching a minimum before increasing again and then reaching a plateau value. It should be mentioned that this non-monotonic behaviour is more notable for large values of the power-law index, or equivalently for weakly shear-thinning fluids (see Figure 4.8-b).

De_c was also found to vary non-monotonically with *Ca*. More specifically, the critical Deborah number initially decreases as *Ca* increases, before starting to increase as the Capillary number further increases (Figure 4.8-b). This non-monotonic effect becomes stronger for larger power-law index, i.e. as the shear-thinning effects decrease.

4.1.4 Critical Power-Law Index

Similar to the critical Deborah number, there is a critical power-law index n_c for given values of the mobility ratio *M*, Capillary number *Ca* and Deborah number *De*. The critical power-law index n_c is defined as the value at which the effective number of fingers is the smallest. It can also be determined from the value at which the FAD reaches its first maximum. In this section, exact values of n_c are presented;

$$n_c = \mathcal{H}_p(M, Ca, De) \tag{4.2}$$

A large number of simulations was conducted to determine the critical values of the power-law index. Figure 4.9 shows the variations of k_{eff} and *FAD* with the power-law index for different values of *De* and for *M*=100 and *Ca*=70. The number of fingers reaches a minimum at the critical index n_c, which tends to decrease with decreasing Deborah number (Figure 4.9-a). Similarly, the finger area density reaches its maximum at the critical power-law index (Figure 4.9-b).

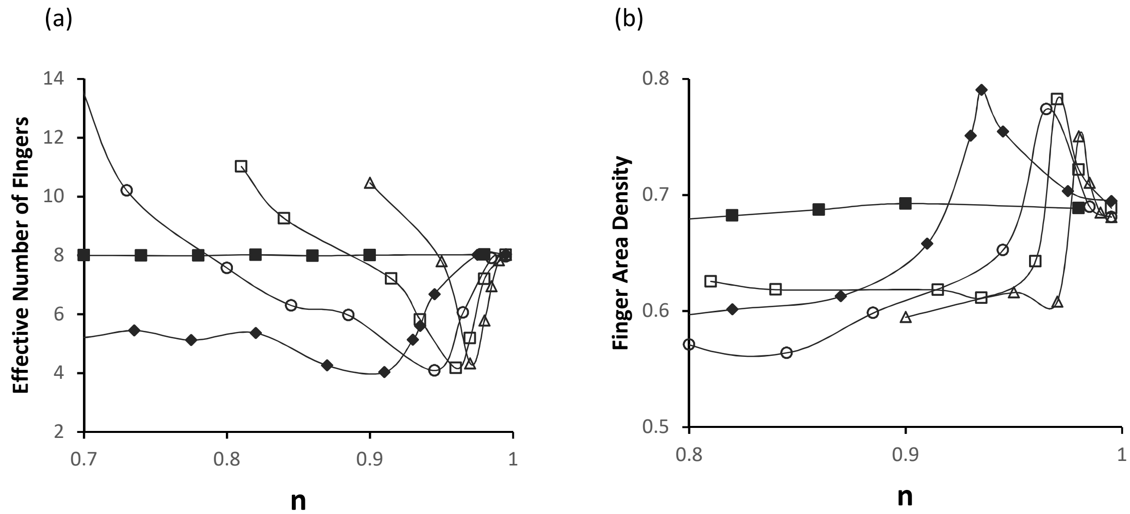

Figure 4.9 *(a) Effective number of fingers and (b) Finger area density versus n for different values of De at* $t^* = 15$. *De=0.02(■), 0.10(◆), 0.15(○), 0.20(□), 0.30(△).*

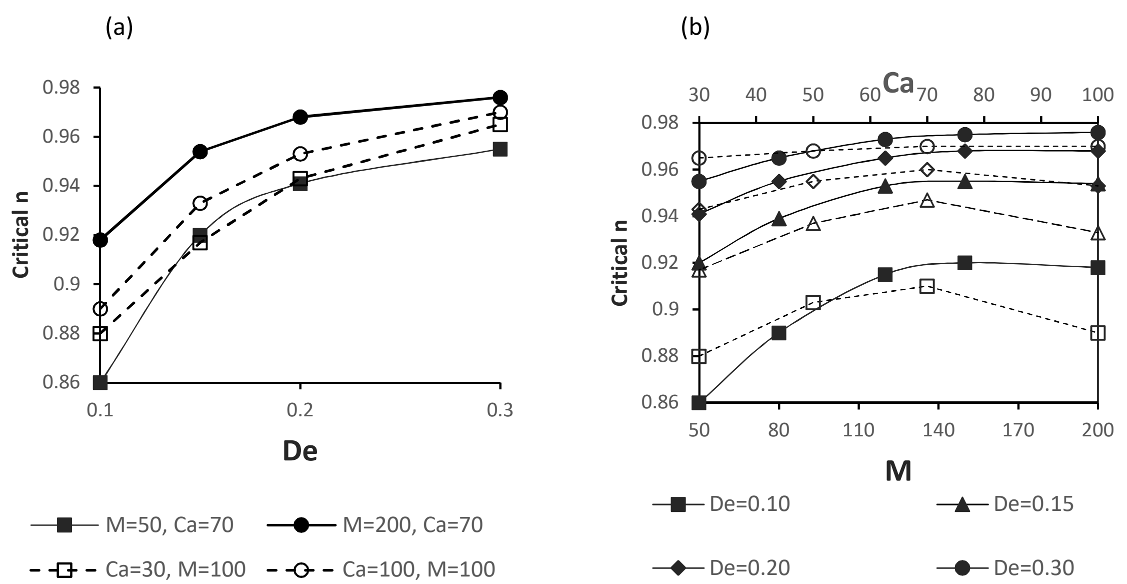

Figure 4.10 *Critical power-law index versus (a) De for different values of M and Ca, (b) M and Ca for different values of De, filled symbols for M (Ca=70) and empty symbols for Ca (M=100).*

The dependence of n_c on the other three governing parameters is illustrated in Figure 4.10. For a fixed Capillary number *Ca* =70, the critical power-law index shows an overall increasing trend with increasing *De* for fixed mobility ratio (Figure 4.10-a) and with increasing *M* for fixed

Deborah number (Figure 4.10-b). However this increase tends to be stronger for smaller values of either parameters, *De* or *M*, and levels off for larger values. For a fixed *M=100*, n_c increases with De for any given *Ca* (Figure 4.10-a) and shows a non-monotonic dependence on the Capillary number under fixed *De*, where it initially increases up to a maximum before decreasing again (Figure 4.10-b). This dependence on *Ca* is however weak for larger *De*, where n_c becomes virtually independent of the Capillary number.

4.2 Shear-Thickening Flow Displacements

The previous results and discussion have focused on shear-thinning fluids (*n<1)*. In this section, we focus our attention on shear-thickening (dilatant) fluids (*n>1)* and follow the same line of analysis as for shear-thinning flow displacements.

4.2.1 Interfacial Contours

Figure 4.11 depicts time sequences of interfacial contours for *n=1.2* and different values of the Deborah number. There is a clear trend for change of the interfacial instability and the number of fingers with increasing De. Similar to what was found in the case of shear-thinning displacements, the trends are also here non-monotonic where in a first stage larger values of De tend to attenuate the instability reducing the number of fingers and resulting in an almost stable interface. The trend is subsequently reversed where stronger interfacial instabilities develop as De is further increased.

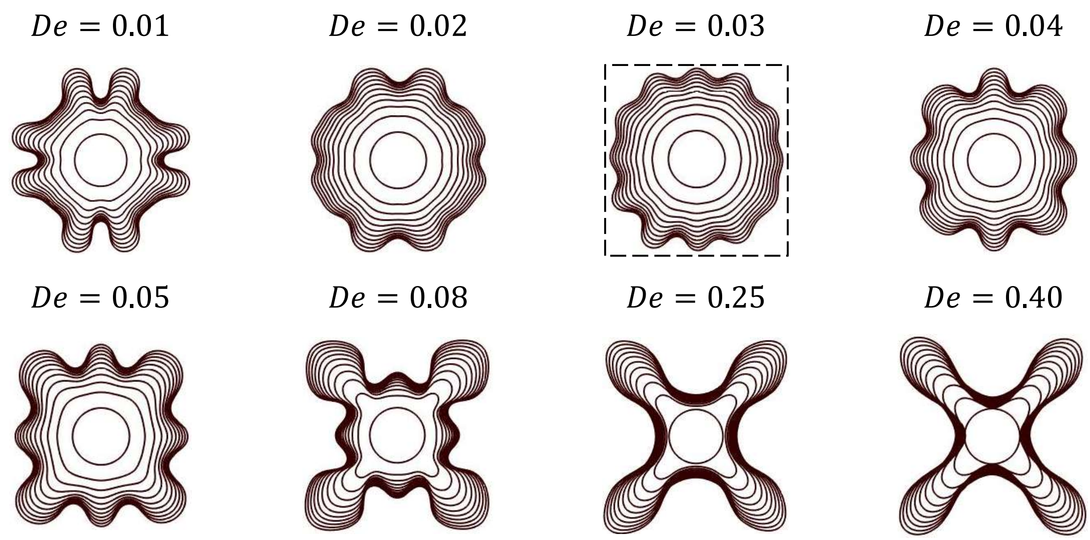

Figure 4.11 *Time sequences of the interface for $n = 1.2$ and different values of the Deborah number over $t^* = 0\ to\ 15$.*

The effects of the power-law index *n* on the instability are depicted in Figure 4.12 for $De = 0.03$. The shear-thickening effects become stronger as the power-law index increases. The interface becomes less unstable, and tip-splitting is delayed with a small increase of *n*. However, interfacial instabilities start to grow again and become stronger with a further increase of *n*.

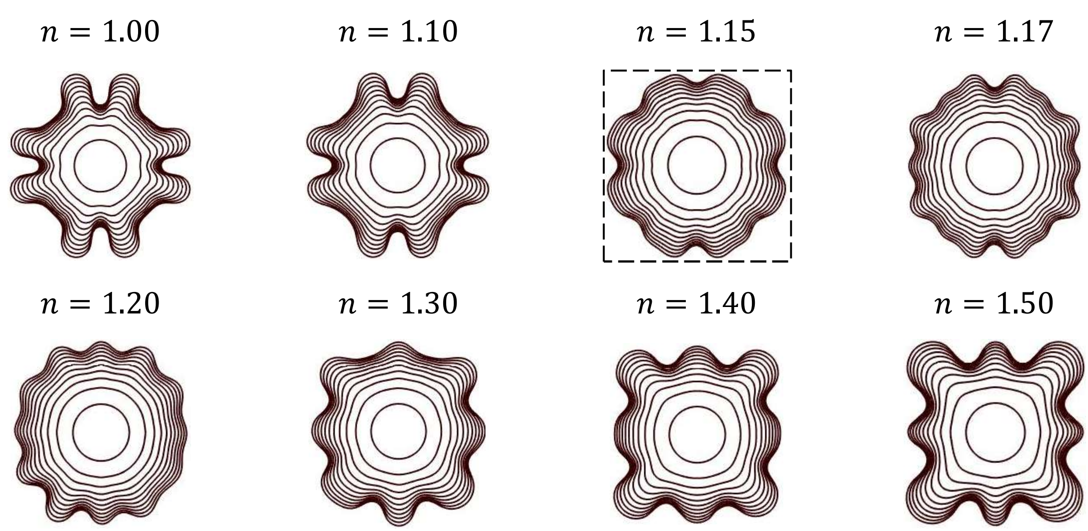

Figure 4.12 *Time sequences of the interface for $De = 0.03$ and different values of the power-law index over $t^* = 0\ to\ 15$.*

4.2.2 Quantitative Analysis

The effective number of fingers and the finger area density are used to characterize and quantify the interfacial instability. Figure 4.13 shows the variations of k_{eff} and *FAD* with time for different values of the Deborah number in the case *n=1.2*. After an initial transient regime where the variation may be non-monotonic, both the effective number of fingers and the finger area density reach a steady state. What is notable is that the values of k_{eff} and *FAD* at the steady state vary non-monotonically with the Deborah number reaching a maximum at $De \approx 0.03$ where the maximum effective number of fingers is about nine. The results of this quantitative analysis confirm the existence of the critical Deborah number $De_c \approx 0.03$ in the case *n=1.2*. It should be noted that for large enough values of De, both the effective number of fingers and the finger area density tend to converge towards an asymptotic value.

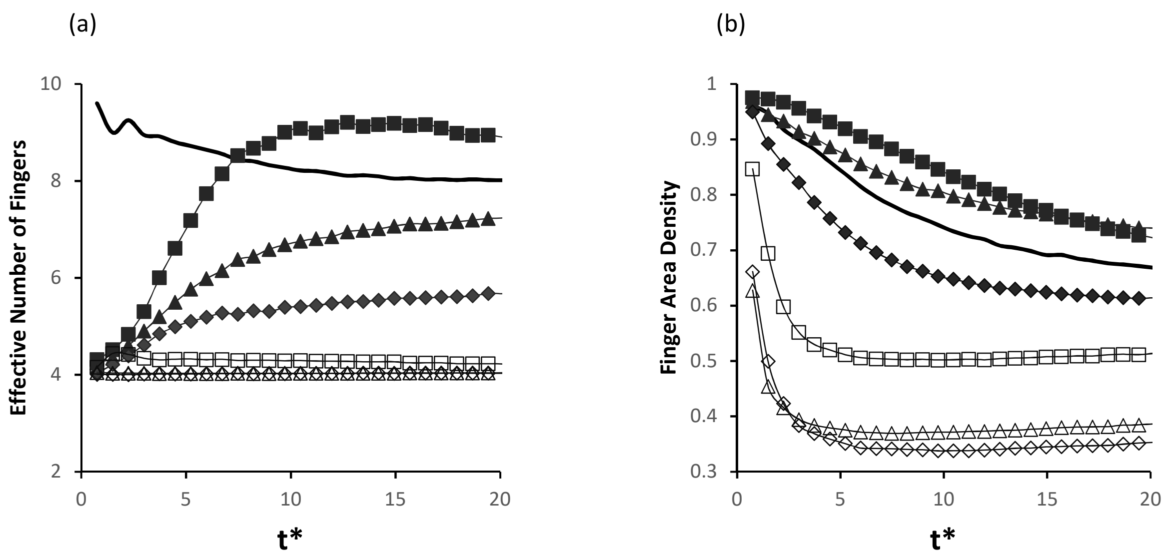

Figure 4.13 *(a) Effective number of fingers and (b) Finger area density versus time for n=1.2 and different values of De. De=0.0(—), 0.03(■), 0.04(▲), 0.05(◆), 0.08(□), 0.25(△), 0.40(◇).*

Similar conclusions are drawn from plots of the variations of k_{eff} and *FAD* with time for different values of the power-law index *n* at fixed $De = 0.03$ (see Figure 4.14). Variations with *n* of both k_{eff} and *FAD* are also non-monotonic showing the existence of a critical power-law index value $n_c \approx 1.17$.

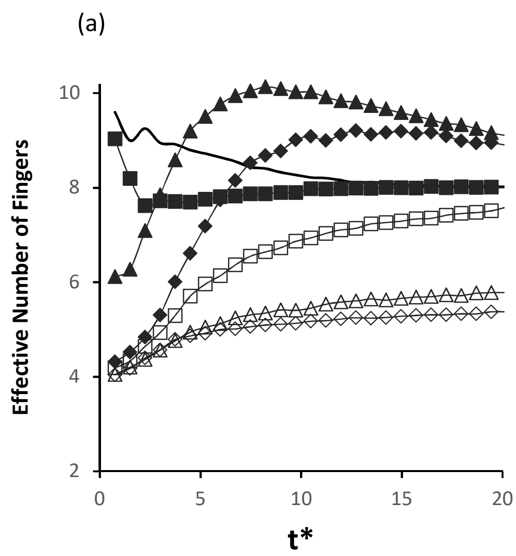

Figure 4.14 *(a) Effective number of fingers and (b) Finger area density versus time for De=0.03 and different values of n. n=1.00(▬), 1.10(■), 1.15(▲), 1.20(◆), 1.30(□), 1.40(△), 1.50(◇).*

4.2.3 Critical Deborah number

Similar to the shear-thinning flow displacement, the previous results reveal that for fixed values of *M*, *Ca* and *n*, there is a critical Deborah number De_c that characterizes the non-Newtonian displacement;

$$De_c = \Im_d(M, Ca, n) \tag{4.3}$$

De_c is defined as the Deborah number at which the effective number of fingers and the finger area density are the largest.

A large number of simulations has been carried out and Figure 4.15 presents the variations of k_{eff} and *FAD* with the Deborah number for different values of the power-law index and for *M*=100 and *Ca*=70. Initially, an increase of De results in an increase of k_{eff}. However, as illustrated in Figure 4.11, though the fingers increase in number, they are less protruding resulting in an almost circular interface. This explains the corresponding increase of the *FAD*. As De is further increased, few of the small protruding fingers project out radially and in the process suppress neighbouring fingers. This leads to a more distorted interface with smaller but more developed fingers. Hence the observed subsequent decrease of k_{eff} and *FAD.* This shows that both the number of fingers and the finger area density reach a maximum at the critical Deborah number (Figure 4.15).

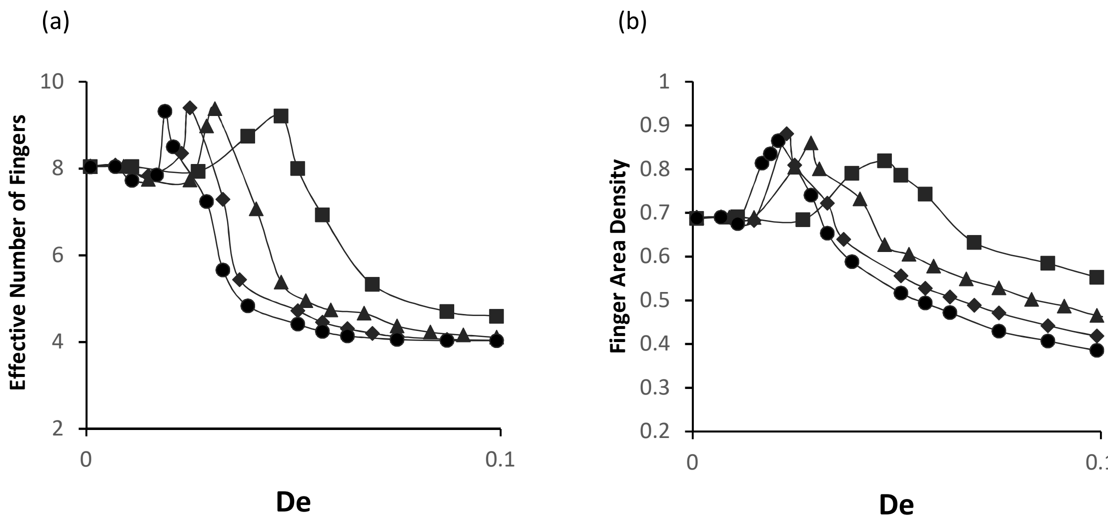

Figure 4.15 *(a) Effective number of fingers and (b) Finger area density versus De for different values of n at* $t^* = 15$. *n=1.10(■), 1.20(▲), 1.30(◆), 1.40(●).*

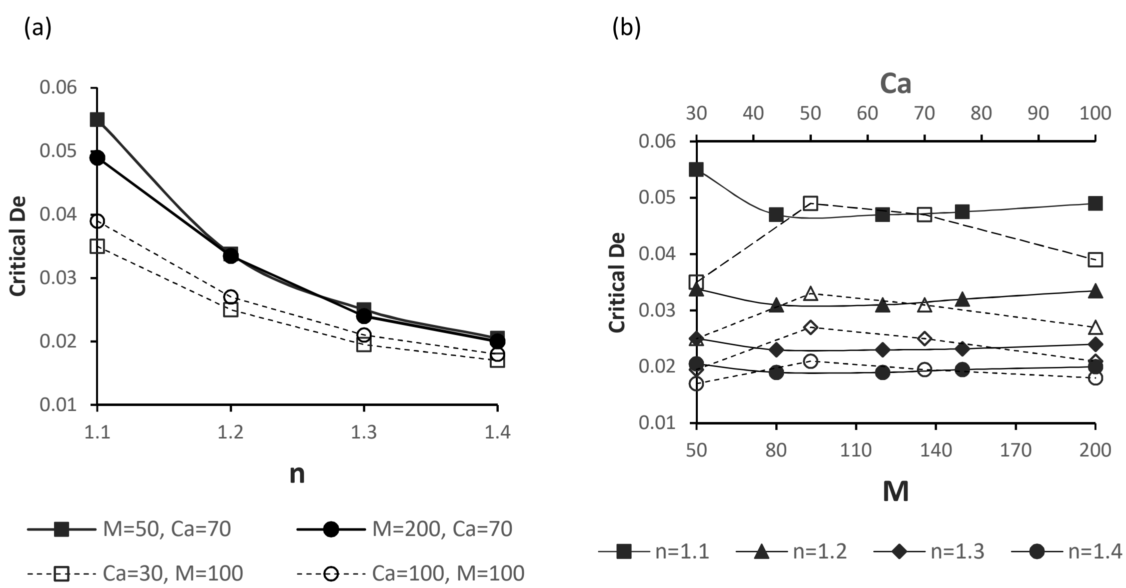

Figure 4.16 *Critical Deborah number versus (a) n for different values of M and Ca, (b) M and Ca for different values of n, filled symbols for M (Ca=70) and empty symbols for Ca (M=100).*

The dependence of the critical Deborah number on the power-law index, the mobility ratio and the Capillary number is illustrated in Figure 4.16. For any fixed value of *M* and *Ca*, there is a clear monotonic trend for a decrease of De_c as *n* increases, however this dependence decreases for large values of the power-law index (Figure 4.16-a). The variation of De_c with the mobility ratio is most noticeable at the smaller values of *M* where there is a decreasing trend that is stronger for the lower values of *n*. For large *M*, the critical Deborah number may be deemed independent of the mobility ratio (Figure 4.16-b). The dependence of De_c on *Ca* for fixed *n* and *M* is however non-monotonic, reaching a maximum value around *Ca=50* for *M*=100 and all considered values of *n* (Figure 4.16-b).

4.2.4 Critical Power-Law Index

The simulation results confirm that there is a critical power-law index n_c for given values of the mobility ratio *M*, Capillary number *Ca* and Deborah number De. This critical index n_c is defined as the power-law index value at which the effective number of fingers and FAD are maximum;

$$n_c = \mathcal{H}_d(M, Ca, De) \tag{4.4}$$

Figure 4.17 shows the variations of k_{eff} and *FAD* with the power-law index for different values of the Deborah number and for *M*=100 and *Ca*=70. Both the number of fingers and FAD reach their maximum values at the critical n_c.

As illustrated in Figure 4.18-a, the critical power-law index tends to decrease with increasing De, and this for all values of *M* and *Ca*. For any fixed values of the Capillary and Deborah numbers; n_c tends to decrease with increasing *M*, but this dependence levels off at large mobility ratios (Figure 4.18-b). The variation of the critical power-law index with the Capillary number is non-monotonic exhibiting an increasing trend in the range of small values of *Ca*, followed by a decreasing trend (Figure 4.18-b). The maximum is attained for $Ca \approx 50$ in the case *M*=100 and for all considered values of *De*.

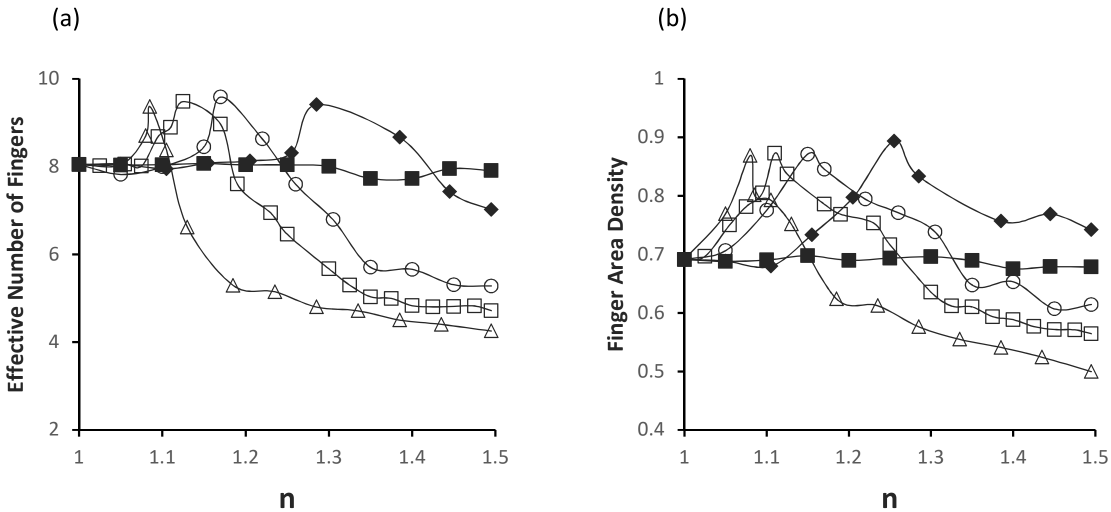

Figure 4.17 *(a) Effective number of fingers and (b) Finger area density versus n for different values of De at* $t^* = 15$. *De=0.01(■), 0.025(◆), 0.03(○), 0.04(□), 0.05(△).*

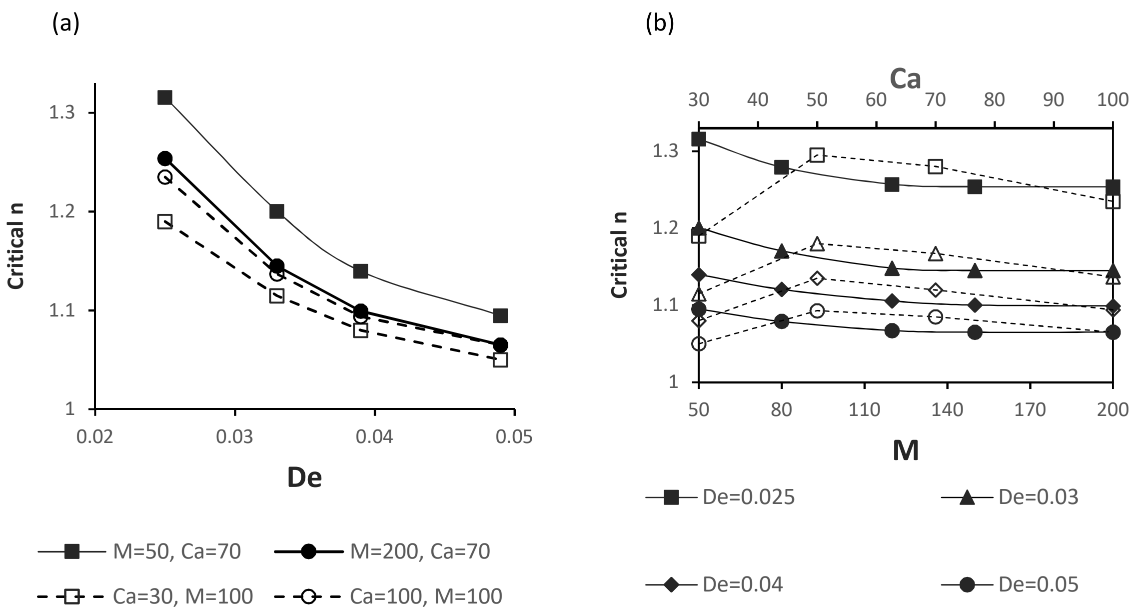

Figure 4.18 *Critical power-law index versus (a) De for different values of M and Ca, (b) M and Ca for different values of De, filled symbols for M (Ca=70) and empty symbols for Ca (M=100).*

The previous results indicate that there are critical values of the two rheological parameters; *De* and *n* at which the evolution of the finger structures at the interface undergoes a change resulting in the least unstable interfacial configuration. The values of the critical Deborah number and power-law index were determined using the variation of two quantitative properties, the effective number of fingers and the fingers' area density (FDA). The dependence of these critical rheological characteristics on the other parameters are summarized in Table 4.1.

		Effect of increasing *De*	Effect of increasing *n*	Effect of increasing *M*	Effect of increasing *Ca*
Shear-thinning fluids	De_c		↗	↘	↘↗
	n_c	↗		↗	↗↘
Shear-thickening fluids	De_c		↘	↘	↗↘
	n_c	↘		↘	↗↘

Table 4.1 *Summary of the effects of M, Ca, n and De on the critical Deborah number and power-law index.*

These special values are expected to be associated with a change in the local forces at the interface, and understandably with the nature of the flow. The dynamics in the case of the non-Newtonian fluids are expected to depend on the local viscosity which is directly dependent on the local velocity gradients. As a result, different flow characteristics have been closely looked at and around the critical values in an attempt to identify the mechanisms behind these changes. These included the effective mobility ratio M_g, the velocity field and shear stress around the interface. For brevity, the results of this investigation are not presented and we will focus only on the aspects that seem to point towards the pertinent mechanisms.

The shear-thinning character of a non-Newtonian fluid is known to increase the selection and wavelength of unstable modes [22]. This results in a stabilization of small wavelengths and the attenuation or suppression of tip-splitting. Under small shear-thinning effects, the flow is not affected in its early development and exhibits the same morphology and number of fingers as in the Newtonian case (see Figures 4.1-4.3). However, stronger velocity gradients in the later stages of the flow accentuate the shear-thinning effects, resulting in the attenuation or even suppression of tip-splitting. As a result, the interface exhibits four dominant outward growing fingers that are wider than the original fingers and cover more of the flow domain. This translates in the observed initial decrease of k_{eff} and increase of *FAD*. This also corresponds to the least unstable configuration with the smoothest possible interface and as a consequence smallest velocity gradients. Further increase of *De* and/or decrease of *n* accentuate the shear-thinning effects that now can develop at lower shear-rates. As a result, these effects are manifested in the first stages of the flow leading to an early distortion of the interface (e.g. *De*=0.15 in Figure 5 or n=0.92 in Figure 7). This helps the early emergence of wide fingers that offer an easy flow path for the displacing fluid and result in localized strong velocity gradients. Under such strong gradients, larger *De* or smaller *n* lead to a smaller effective viscosity of the displaced fluid and hence a region of low flow resistance that tends to feed the growth of these dominant, outward growing fingers. The region between these early dominant fingers stretches and develops new side-fingers once it exceeds the critical length for unstable modes to grow. Recall that this critical wavelength is larger for shear-thinning fluids, hence the later development of these side-fingers. This offers a new flow route for the displacing Newtonian fluid and helps feed these sub-fingers through the main mechanism previously described for the dominant ones. As a result, stronger velocity gradients develop and accentuate the shear-thinning effects in the subsequent flow evolution. Consequently, the interface develops a series of new sub-fingers, side-fingers, tip-splitting and branching structures. These complex mechanisms are observed mainly on the dominant fingers for moderate shear-thinning effects, but extend to all fingers in the case of strongly shear-thinning fluids.

In the case of shear-thickening fluids, there is a tendency towards larger wave-number unstable modes that result in smaller fingers. There is also a shift of the dominant unstable modes towards larger wavenumbers accompanied with a decrease of the growth rate [22]. These effects are well manifested in the later stages of the flow when the shear-thickening effects are small. This explains the initial increase in the number of fingers that tend to be thinner and less developed, as either the Deborah number or power-law index is increased (Figures 4.11 and 4.12). Note that though the fingers increase in number, they are less protruding resulting in an undulating, almost circular interface. Hence the observed initial increase of both k_{eff} and *FAD*. Under these conditions, the displacement exhibits its least unstable interface and smallest velocity gradients. As shear-thickening effects increase and as a result the effective mobility ratio increases, the instability is affected early in the flow. This leads to the development of few thin and outward extending fingers that dominate the early development of the flow. This trend is expected based on previous studies where it is reported that larger mobility ratios tend to reduce inter-finger interactions [84]. This favors the mechanism of shielding where only few primary fingers dominate the flow and suppress the growth of secondary ones. As a result, strong velocity gradients between the tip and fjords of the fingers develop and lead to even larger effective mobility ratios. This sustains the growth of these fingers and suppresses the developments of sub-fingers, resulting in smaller swept area of the displaced fluid. Hence the observed drop in the number of fingers and the finger area density.

The previous interpretations based on the changes in the local velocity gradients and the interplay with the interfacial instability are further ascertained by examining the variation of the shear strain rate at the interface. Figure 23 depicts the shear strain rate at the interface as a function of the angular coordinate $\theta \in [0,2\pi]$ for different values of the Deborah number. The results are presented at *M*=100, *Ca*=70, *n*=0.8 that lead to a De_c ≈*0.07*. The radial position of the interface is also shown.

It is clear that the shear strain rate (*SSR*) varies with the Deborah number, such that it is smoother at De_c. This smoother behaviour was quantified and ascertained through plots of the Fourier's transform that for brevity, are not shown here. This is further quantified by the values of the average of the rate of shear strain that clearly reaches a minimum value at De_c (see Figure 4.19). At this critical value, the interfacial length (*IL*) is also at its minimum value, reflecting the least unstable nature of the interface.

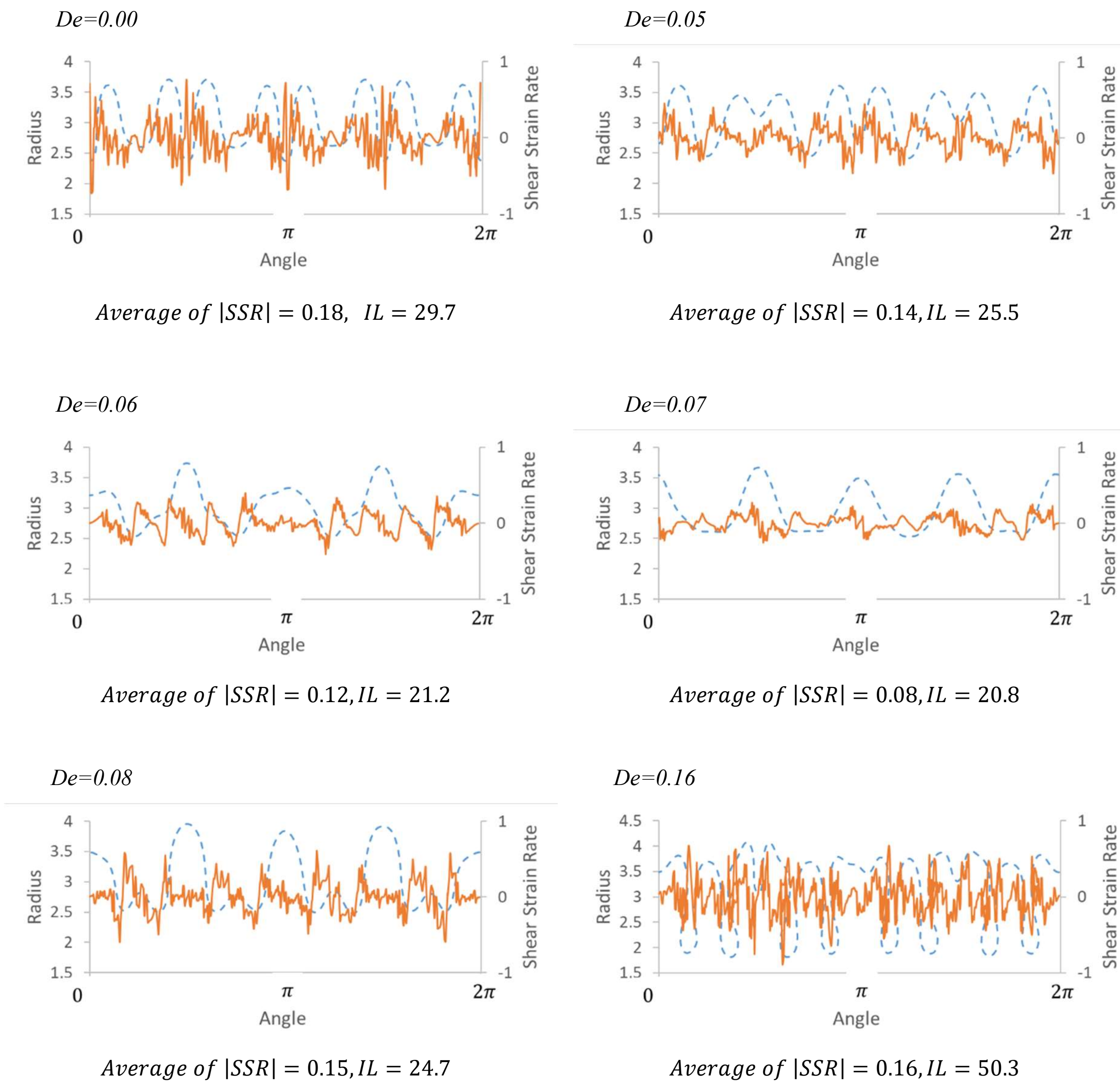

Figure 4.19 *Variations of the shear rate strain and interfacial location for different values of the Deborah number. M=100, Ca=70, n=0.8 and t*=15.*

These results were consistently observed for all examined parameters, i.e. minimum shear strain rate and interfacial length at the critical values De_c and n_c . Though not presented for brevity, the same conclusions were obtained for shear-thickening flows.

4.3 Discussion

In this Chapter, it is found that the characteristics of both the shear-thinning or shear-thickening fluids, namely *De* and *n,* result in non-monotonic effects on the interfacial instability, where initially they tend to attenuate the instability before subsequently enhancing it. This has led to the identification of critical values De_c and n_c that lead to the least unstable interfaces. The dependence of the critical Deborah number De_c and power-law index n_c on *M* and *Ca* are examined.

It is also found that for fixed values of and *M* and *Ca*, De_c increases with increasing power-law index in the case of shear-thinning fluids and decreases in the case of shear-thickening ones. This implies that the stronger the deviation from the Newtonian behaviour the smaller the critical Deborah number. Likewise, n_c was found to increase with the Deborah number in shear-thinning flows and to decrease in shear-thickening ones, with these trends levelling off at large *De*. Furthermore, both De_c and n_c exhibit a strong dependence on the mobility ratio at small values of *M*, and are weakly dependent or virtually independent on *M* at large values of the mobility ratio. More specifically, De_c exhibits a decreasing trend with *M* for both shear-thinning and shear-thickening fluids while increasing and decreasing trends of n_c with *M* are found in the case shear-thinning and shear-thickening fluids, respectively. The dependence of the critical values of both rheological parameters on the Capillary number are however non-monotonic. In both shear-thinning and shear-thickening flows as *Ca* increases, n_c first increases and then decreases after attaining a maximum. The critical Deborah number exhibits a minimum at an intermediate value of Ca in shear-thinning flows and a maximum in shear-thickening ones. It must be finally mentioned that under strong non-Newtonian behaviours (small *n* for shear-thinning fluids and large *n* for shear-thickening ones) the dependence of the critical Deborah number on either *M* or *Ca* become small and De_c can be regarded to be independent of these two parameters.

CHAPTER 5

RESULTS: NON-HOMOGENEOUS POROUS MEDIA

In this Chapter, immiscible radial displacement flows between two Newtonian fluids in a non-homogeneous porous media are examined. The physical model of the flow in a non-homogeneous porous medium and the governing equations with boundary conditions are presented, and the simulation results are discussed.

5.1 Governing Equations

In this section, the model geometry with non-momogeneous porous medium is presented, and the governing equations and corresponding boundary conditions are discussed.

5.1.1 Model Geometry

The domain under consideration consists of a horizontal two-dimensional non-homogeneous square [2a x 2a] porous medium where the permeability k varies with the radial distance from the centre. A Newtonian fluid (fluid 1) of viscosity η_1 is injected in the centre of the domain to displace radially a second Newtonian fluid (fluid 2) of viscosity η_2. A schematic of the flow is depicted in Figure 5.1.

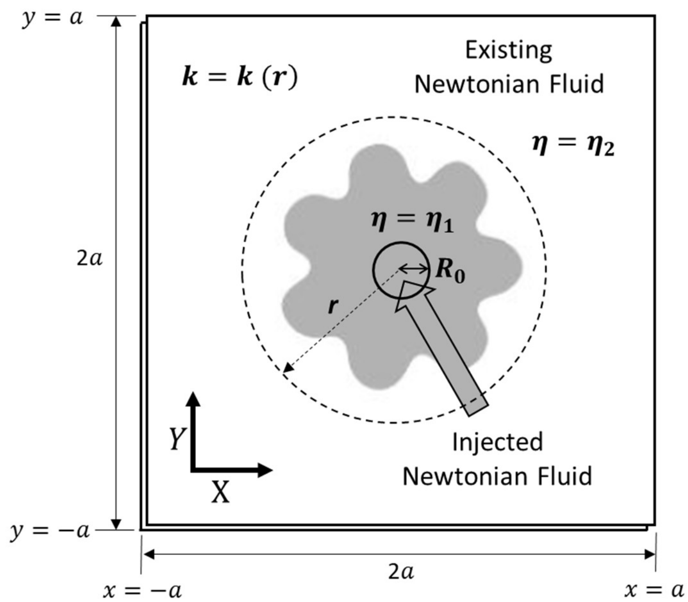

Figure 5.1 *Schematic of the two-fluid radial displacement in the non-homogeneous porous medium.*

5.1.2 Governing Equation

In the present study, the permeability varies periodically in the radial direction from the centre:

$$k(r) = \begin{cases} k_0, & r < R_0 \\ k_0(1 + b \sin a(r - R_0)), & r \geq R_0 \end{cases} \tag{5.1}$$

where *a* and *b* are the frequency and amplitude of the permeability variation respectively. The permeability is constant k_0 within the initial cicular interface $(r < R_0)$ where a Newtonian fluid is injected. Figure 5.2 shows how the permeability $k(r)$ changes for example values of the frequency and amplitude.

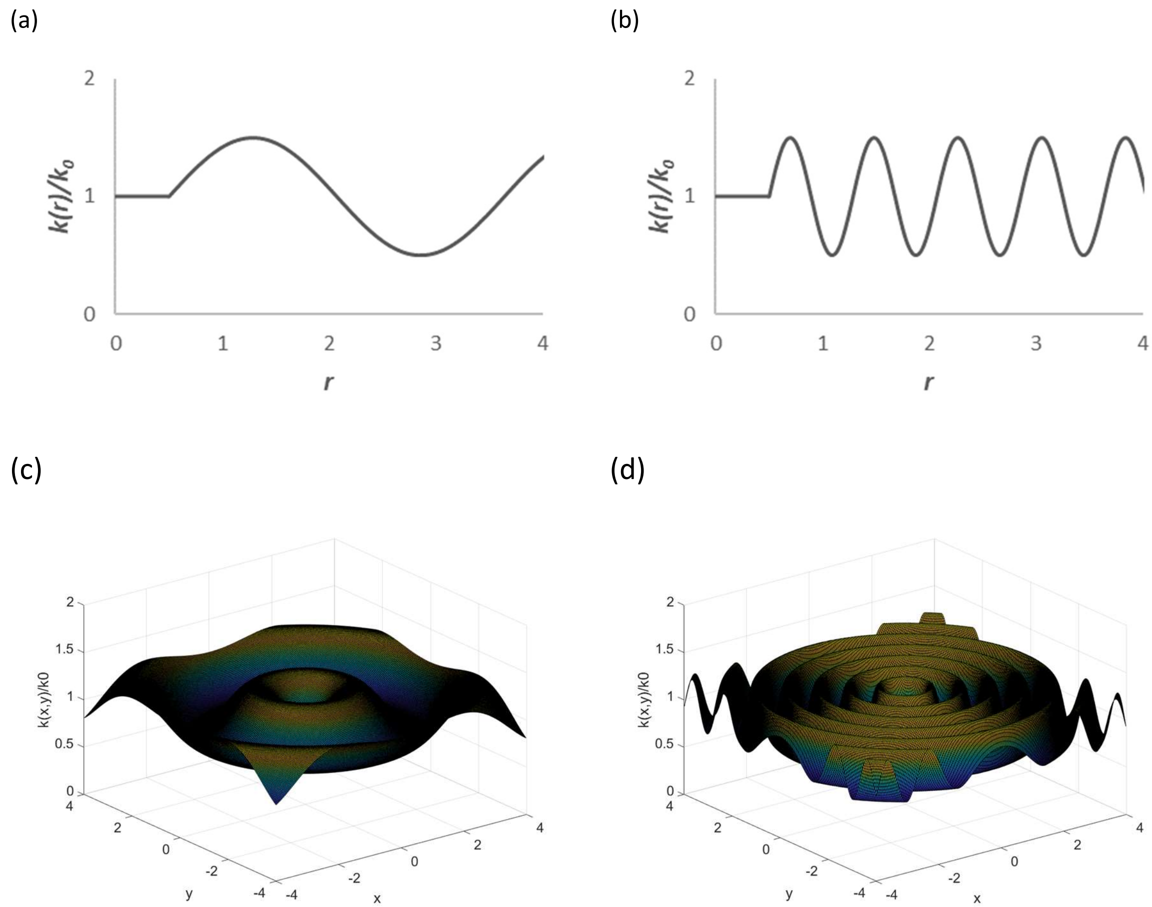

Figure 5.2 *$k(r)/k_0$ versus r for R_0=0.5 and (a) a=2, b=0.5 (b) a=8, b=0.5 (c) a=2, b=0.25 (d) a=8, b=0.25*

The mobilities of the two fluids are $\beta_1(r) = k(r)/\eta_1$ and $\beta_2(r) = k(r)/\eta_2$. The flow displacement is governed by the Darcy's law and the continuity equation:

$$\nabla p = \begin{cases} -\dfrac{1}{\beta_1(r)} U & fluid\ 1 \\ -\dfrac{1}{\beta_2(r)} U & fluid\ 2 \end{cases} \tag{5.2}$$

$$\nabla \cdot U = \begin{cases} \phi(r), & r \le R_0 \\ 0, & r > R_0 \end{cases} \tag{5.3}$$

The boundary conditions at the interface and the distribution of the injection strength remain the same as the ones presented in Chapter 3. The pressure drop across the interface is equation (4) where τ is the surface tension and κ is the curvature of the interface. Equation (5.5) is the kinematic boundary condition. Equation (5.6) is the injection strength $\phi(r)$ distributed over the injection area. Equation (5.7) is the constant injection rate Q_0 obtained by integrating $\phi(r)$ over the injection area.

$$[p]_1^2 = \tau\kappa \tag{5.4}$$

$$[U_n]_1^2 = 0 \tag{5.5}$$

$$\phi(\mathrm{r}) = \begin{cases} \varphi_0[1 + \cos(\pi \mathrm{r}/\mathrm{R}_0)], & \mathrm{r} \le \mathrm{R}_0 \\ 0, & \mathrm{r} > \mathrm{R}_0 \end{cases} \tag{5.6}$$

$$\mathrm{Q}_0 = \varphi_0 {\mathrm{R}_0}^2 \left(\pi - \frac{4}{\pi}\right) \tag{5.7}$$

5.1.3 Numerical Methods

The governing equations with the jump conditions at the interface is a two-dimensional elliptic interface problem with non-constant coefficients $\beta^+(r) = \beta_2(r) = k(r)/\eta_2$ and $\beta^-(r) = \beta_1(r) = k(r)/\eta_1$. The coefficient $\beta(r)$ depends on only the radial distance from the centre, and it is discontious at the interface. In the injection area ($\mathrm{r} \le \mathrm{R}_0$), $\beta(r)$ is constant k_0/η_1. The equations are solved using the same iterative method presented in Chapter 3. The problem and jump conditions along the interface are

$$\Delta(\beta(r)\nabla u) = f(x,y)$$

$$[u] = w(s) \tag{5.8}$$

$$[\beta u_n] = v(s)$$

where u is the pressure and f is the source term and $v(s) = 0$ and $w(s)$ is the pressure drop due to the surface tension. The above problem is preconditioned to an equivalent problem as shown in Chapter 3:

$$\Delta u + \frac{\nabla\beta^+}{\beta^+}\cdot\nabla u = \frac{f}{\beta^+}\ (outside\ interface)$$

$$\Delta u + \frac{\nabla\beta^-}{\beta^-}\cdot\nabla u = \frac{f}{\beta^-}\ (inside\ interface)$$

(5.9)

$$[u] = w(s)$$

$$[u_n] = g(s)$$

where $g(s)$ is unknown. The terms other than Δu are moved to the right hand side in order to use the fast poison solver in an iterative way:

$$\Delta u = \frac{f}{\beta^+} - \frac{\nabla\beta^+}{\beta^+}\cdot\nabla u\ (outside\ interface)$$

(5.10)

$$\Delta u = \frac{f}{\beta^-} - \frac{\nabla\beta^-}{\beta^-}\cdot\nabla u\ (inside\ interface)$$

The iteration starts with the case where the permeability is constant k_0. The right-hand side of the equation is calculated from the solution of the previous iteration and treated as constant. The iteration continues until the relative difference between the current and previous solutions is less than 1.0E-04. The correction term in each iteration is assumed to be the same as the correction term of the first iteration where the permeability constant k_0.

5.2 Results

In order to investigate the effects of the periodically varying permeability $k(r)$ on the finger structures, numerous simulations were carried out varying the frequency a of $k(r)$ with a fixed amplitude $\mathrm{b} = 0.25$ for different values of the Capillary number Ca and the mobility ratio M. Figure 5.3 depicts time sequences of the interface for $\mathrm{Ca} = 70$, $\mathrm{M} = 60$ and different values of the frequency a of $k(r)$ from $\mathrm{a} = 1$ to $\mathrm{a} = 10$. The finger structures are almost the same showing eight dominant fingers for all frequencies of the periodic permeability.

$a = 1$ $a = 4$ $a = 8$ $a = 10$

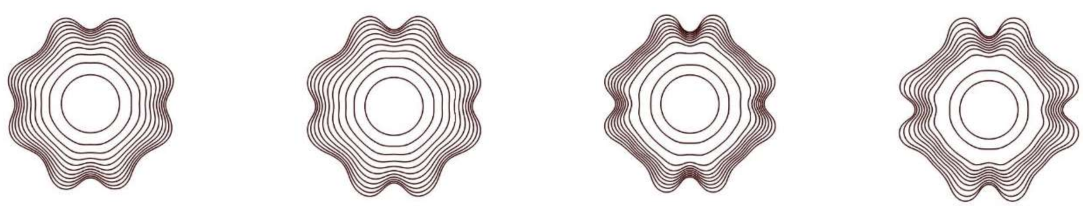

Figure 5.3 *Time sequences of the interface for $Ca = 70$, $M = 60$ and different values of the frequency a over $t^* = 0 \; to \; 15$.*

Figure 5.4 shows time sequences of the interface for a larger value of the mobility ratio, $M = 140$. The finger structures are almost identical for smaller frequencies of the periodic permeability, $\mathrm{a} = 1$ and $\mathrm{a} = 4$. However, the interfaces become slightly more unstable for larger frequencies, $\mathrm{a} = 8$ and $\mathrm{a} = 10$.

$a = 1$ $a = 4$ $a = 8$ $a = 10$

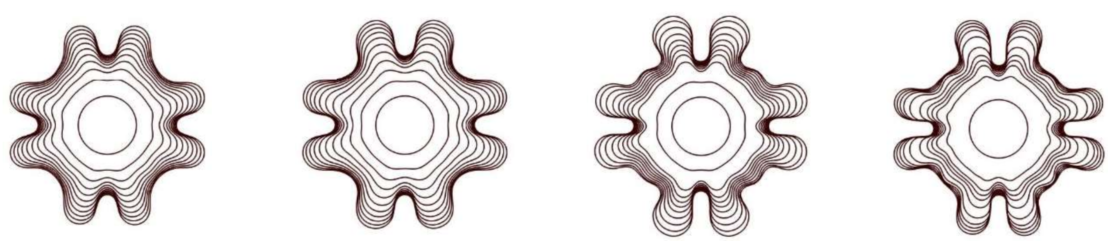

Figure 5.4 *Time sequences of the interface for $Ca = 70$, $M = 140$ and different values of the frequency a over $t^* = 0 \; to \; 15$.*

Similar results for a larger value of the Capillary number, $Ca = 90$, are shown in Figure 5.5. The periodic permeabilities of smaller frequencies have little effect on the finger structures, and slightly more unstable interfaces are obtained for larger frequencies.

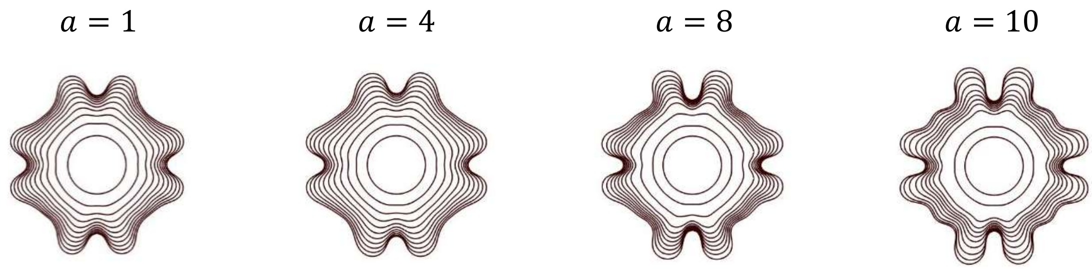

Figure 5.5 *Time sequences of the interface for $Ca = 90$, $M = 60$ and different values of the frequency a over $t^* = 0\ to\ 15$.*

The effects of the periodic permeability for larger values of the Capillary number, $Ca = 90$ and the mobility ratio, $M = 140$ are presented in Figure 5.6. Similar to the previous results, the finger structures are not affected by the periodic permeabilities of smaller frequencies. However, the interface becomes noticeably more unstable with a larger frequency of $a = 10$. This indicates that the periodic permeability field of a higher frequency can enhance the instability of an interface when the Capillary number and the mobility ratio are large enough.

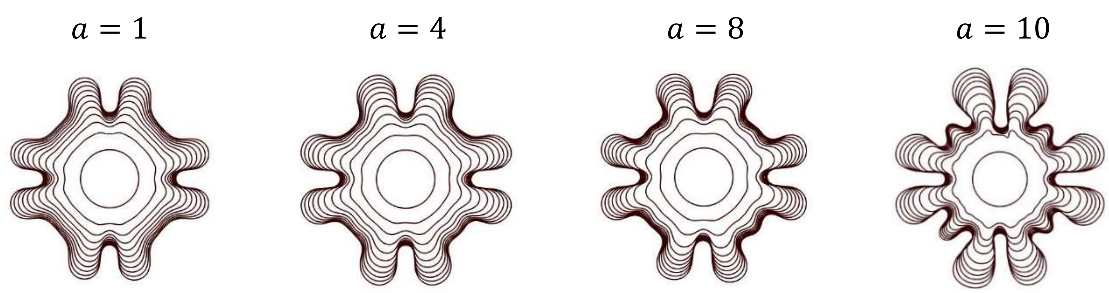

Figure 5.6 *Time sequences of the interface for $Ca = 90$, $M = 140$ and different values of the frequency a over $t^* = 0\ to\ 15$.*

5.3 Discussion

In this chapter, immiscible radial displacement flows between two Newtonian fluids in a non-homogeneous porous media with a periodic permeability were examined. The permeability of the non-homogeneous porous media was modeled to vary periodically in the radial direction from the centre and characterized by an amplitude and frequency. Simulations were carried out for different values of the Capillary number and the mobility ratio varying the frequency at a fixed amplitude in order to examine the effects of the periodic permeability on the interfacial instability. It is found that the periodic permeability has negligible effects on the finger structures when the Capillary number and the mobility ratio are smaller. However, the simulation results indicated that the instability of an interface can be noticeably enhanced in a non-homogeneous porous media with a higher frequency periodic permeability field when the Capillary number and the mobility ratio are large enough.

CHAPTER 6

CONCLUSIONS AND RECOMMENDATIONS

6.1 Summary

In Chapter 3 and 4, immiscible flows that involve radial displacements of shear-thinning or shear-thickening non-Newtonian fluids by a Newtonian fluid in homogeneous porous media are examined. The flows characterized by four dimensionless groups, the mobility ratio *M*, the Capillary number *Ca*, the Deborah number *De* and the power-law index *n* are modeled numerically to trach the time evolution of the interface. The flow displacements are characterized qualitatively through time sequences of the interfacial contours as well as quantitatively using the effective fingers number k_{eff} obtained from Fourier spectra of the interface and the finger area density, *FAD*. The results show that the effects of these two parameters on the instability are not monotonic, and it is found that there exists some critical value of either De or n for which the flow is least unstable. The dependence of these critical values on the mobility ratio (M) and Capillary number (Ca) is also examined.

In Chapter 5, immiscible radial displacement flows between two Newtonian fluids in a non-homogeneous porous media with a periodic permeability are examined numerically. The effects of the frequency of the periodic permeability are investigated by performing simulations for different values of the Capillary number (Ca) and the mobility ratio (M). The results show that the periodic permeability has negligible effects for small Ca and M. However, the interface becomes noticeably unstable in a high frequency periodic permeability porous media for large Ca and M.

6.2 Recommendations

The results for this study involving immiscible radial displacements of shear-thinning or shear-thickening fluids by a Newtonian fluid in a homogeneous porous medium offer the perspective of using the interfacial finger structures to determine the rheological properties of generalized Newtonian (shear-thinning/shear thickening) fluids. This possibility may be actually extended to general viscoelastic fluids since it is known that elastic effects can be ignored, at least for moderate values of the Deborah number. The results also point to the prospect of using hydrodynamics and flow instabilities under controlled conditions in simple geometries as a potential rheometry tool that can be used as a stand-alone or in conjunction with other standard techniques. The nonlinear simulation can be further extended to perform simulations for immiscible rectilinear flow displacements. There is also a possibility of combining time dependent flows and non-Newtonian displacements. Furthermore, the scenarios where the displacing fluid is non-Newtonian or where both are non-Newtonian can be examined.

References

[1] S. Hill and F. Inst P, "Channelling in packed columns," *Chemical Engineering Science,* vol. 1, p. 247, 1952.

[2] P. G. Saffman, G. I. Taylor, "The penetration of a fluid into a porous medium or Hele-Shaw cell containing a more viscous liquid," *Proceedings of the Royal Society of London A,* vol. 245, p. 312, 1958.

[3] G. M. Homsy, "Viscous fingering in porous media," *Annual Review of Fluid Mechanics,* vol. 19, p. 271, 1987.

[4] S. H. Hejazi and J. Aaziez, "Nonlinear simulation of transverse flow interactions with chemically driven convective mixing in porous media," *Water Resources Research,* vol. 49, p. 4607, 2013.

[5] K. V. McCloud, J. V. Maher, "Experimental perturbations to Saffman-Taylor flow," *Physics Reports,* vol. 260, p. 139, 1995.

[6] A. C. Callan-Jones, J. F. Joanny and J. Prost, "Viscous-fingering-like instability of cell fragments," *Physical Review Letters,* vol. 100, p. 258106, 2008.

[7] O. Zik, Z. Olami and E. Moses, "Fingering instability in combustion," *Physical Review Letters,* vol. 81, p. 3868, 1998.

[8] B. Habermann, "The efficiency of miscible displacement as a function of mobility ratio," *Petroleum Transactions,* vol. 219, p. 264, 1960.

[9] B. Jha, L. Cueto-Felgueroso and R. Juanes, "Fluid mixing from viscous fingering," *Physical Review Letters,* vol. 106, p. 194502, 2011.

[10] J. Nittmann, G. Daccord and H. E. Stanley, "Fractal growth of viscous fingers: quantitative characterization of a fluid instability phenomenon," *Nature,* vol. 314, p. 141, 1985.

[11] G. Daccord, J. Nittmann and H. E. Stanley, "Radial viscous fingers and diffusion-limited aggregation: Fractal dimension and growth sites," *Physical Review Letters,* vol. 56, p. 336, 1986.

[12] M. Kawaguchi, K. Makino and T. Kato, "Viscous fingering patterns in polymer solutions," *Physica D,* vol. 109, p. 325, 1997.

[13] A. Lindner, D. Bonn and J. Meunier, "Viscous fingering in a shear-thinning fluid," *Physics of Fluids,* vol. 12, p. 256, 2000.

[14] A. Lindner, D. Bonn, E. C. Poire, M. B. Amar and J. Meunier, "Viscous Fingering in non-Newtonian fluids," *Journal of Fluid Mechanics,* vol. 469, p. 237, 2002.

[15] H. Li, B. Maini and J. Azaiez, "Experimental and numerical anaysis of the viscous fingering instability of shear-thinning fluids," *The Canadian Journal of Chemical Engineering,* vol. 84, p. 52, 2006.

[16] Y. Nagatsu, K. Matsuda, Y. Kato and Y. Tada, "Experimental study on miscible viscous fingering involving viscosity changes induced by variations in chemical species concentrations due to chemical reactions," *Journal of Fluid Mechanics,* vol. 571, p. 475, 2007.

[17] R. Tsuzuki, T. Ban, M. Fujimura and Y. Nagatsu, "Dual role of surfactant-producing reaction in immiscible viscous fingering evolution," *Physics of Fluids,* vol. 31, p. 022102, 2019.

[18] L. Kondic, P. Palffy-Muhoray and M. J. Shelley, "Models of non-Newtonian Hele-Shaw flow," *Physical Review E,* vol. 54, p. 4536, 1996.

[19] L. Kondic, M. J. Shelley and P. Palffy-Muhoray, "Non-Newtonian Hele-Shaw flow and the Saffman-Taylor instability," *Physical Review Letters,* vol. 80, p. 1433, 1998.

[20] P. Fast, L. Kondic, M. J. Shelley and P. Palffy-Muhoray, "Pattern formation in non-Newtonian Hele-Shaw flow," *Physics of Fluids,* vol. 13, p. 1191, 2001.

[21] B. Singh and J. Azaiez, "Numerical simulation of viscous fingering of shear-thinning fluids," *The Canadian Journal of Chemical Engineering,* vol. 79, p. 961, 2001.

[22] Y. Sun and C. Beckermann, "A two-phase diffuse-interface model for Hele-Shaw flows with large property contrasts," *Physica D,* vol. 237, p. 3089, 2008.

[23] M. Moore, A. Juel, J. Burgess, W. McCormick and H. Swinney, "Fluctuations and pinch-offs observed in viscous fingering," *AIP Conference Proceedings,* vol. 676, p. 189, 2003.

[24] S. Hill, "Channelling in packed columns," *Chemical Engineering Science,* vol. 1, p. 247, 1952.

[25] R. L. Slobod, B. H. Caudle, "X-Ray shadowgraph studies of areal sweepout efficiencies," *Society of Petroleum Engineers,* vol. 195, p. 265, 1952.

[26] P. V. Meurs, "The use of transparent three-dimensional models for studying the mechanism of flow processes in oil reservoirs," *Society of Petroleum Engineers,* vol. 210, p. 295, 1957.

[27] P. G. Saffman and G. Taylor, "The penetration of a fluid into a porous medium or Hele-Shaw cell containing a more ciscous fluid," *Procedings of the Royal Society A,* vol. 245, p. 312, 1958.

[28] R. J. Blackwell, J. R. Rayne and W. M. Terry, "Factors influencing the efficiency of miscible displacement," *Society of Petroleum Engineers,* vol. 217, p. 1, 1959.

[29] B. Habermann, "The efficiency of miscible displacement as a function of mobility ratio," *Transactions of the American Institute of Mining and Metalurgical Engineers,* vol. 219, p. 264, 1960.

[30] A. L. Benham and R. W. Olson, "A model study of viscous fingering," *Society of Petroleum Engineers,* vol. 3, p. 136, 1963.

[31] R. L. Slobod, R. A. Thomas, "Effect of transverse diffusion on fingering in miscible-phase displacement," *Society of Petroleum Engineers Journal,* vol. 3, p. 9, 1963.

[32] T. K. Perkins, O. C. Johnston and R. N. Hoffman, "Mechanics of viscous fingering in miscible systems," *Society of Petroleum Engineers,* vol. 5, p. 301, 1965.

[33] T. K. Perkins, O. C. Johnston, "A study of immiscible fingering in linear models," *Society of Petroleum Engineers Journal,* vol. 9, p. 39, 1969.

[34] R. A. Wooding, "Growth of fingers at an unstable diffusing interface in a porous medium or Hele-Shaw cell," *Journal of Fluid Mechanics,* vol. 39, p. 477, 1969.

[35] L. Paterson, "Radial fingering in a Hele-Shaw cell," *Journal of Fluid Mechanics,* vol. 113, p. 513, 1981.

[36] J.-D. Chen, "Radial viscous fingering patterns in Hele-Shaw cells," *Experiments in Fluids,* vol. 5, p. 363, 1987.

[37] X. Kong, M. Haghighi, Y. C. Yortsos, "Visualization of steam displacement of heavy oils in a Hele-Shaw cell," *Fuel,* vol. 71, p. 1465, 1992.

[38] J. C. Bacri, N. Rakotomalala, D. Salin and R. Woumeni, "Miscible viscous fingering: Experiments versus continuum approach," *Physics of Fluids A,* vol. 4, p. 1611, 1992.

[39] A. G. Banpurkar, A. V. Limaye, S. B. Ogale, "Occurrence of coexisting dendrite morphologies: Immiscible fluid displacement in an anisotropic radial Hele-Shaw cell under a high flow rate regime," *Physical Review E,* vol. 61, p. 5507, 2000.

[40] Y. Nagatsu, N. Fujita, Y. Kato, Y. Tada, "An experimental study of non-isothermal miscible displacements in a Hele-Shaw cell," *Experimental Thermal and Fluid Science,* vol. 33, p. 695, 2009.

[41] A. R. White, T. Ward, "CO2 sequestration in a radial Hele-Shaw cell via an interfacial chemical reaction," *Chaos: An Interdisciplinary Journal of Nonlinear Science,* vol. 22, p. 037114, 2012.

[42] E. O. Dias, E. Alvarez-Lacalle, M. S. Carvalho and J. A. Miranda, "Minimization of viscous fluid fingering: A variational scheme for optimal flow rates," *Physical Review Letters,* vol. 109, p. 1144502, 2012.

[43] R. J. Marshall and A. B. Metzner, "Flow of viscoelastic fuids through porous media," *Industrial & Engineering Chemistry Fundamentals,* vol. 6, p. 393, 1967.

[44] D. L. Dauben and D. E. Menzie, "Flow of polymer solutions through porous media," *Society of Petroleum Engineers,* vol. 19, p. 1063, 1967.

[45] K. S. Lee and E. L. Claridge, "Areal sweep efficiency of pseudoplastic fluids in a five-spot Hele-Shaw model," *Society of Petroleum Engineers,* vol. 8, p. 52, 1968.

[46] J. G. Savins, "Non-Newtonian flow through porous media," *Industrial & Engineering Chemistry,* vol. 61, p. 18, 1969.

[47] G. Daccord and J. Nittmann, "Radial viscous fingers and diffusion-limited aggregation: fractal dimension and growth sites," *Physical Review Letters,* vol. 56, p. 336, 1986.

[48] E. Allen and D. Boger, "The influence of rheological properties on mobility control in polymer-augmented waterflooding," *Society of Petroleum Engineers,* p. 449, 1988.

[49] H. V. Damme, E. Alsac, C. Laroche and L. Gatineau, "On the respective roles of low surface tension and non-Newtonian rheological properties in fractal fingering," *Europhysics Letters,* vol. 5, p. 25, 1988.

[50] D. E. Smith, X. Z. Wu, A. Libchaber, E. Moses and T. Witten, "Viscous finger narrowing at the coil-stretch transition in a dilute polymer solution," *Physical Review A,* vol. 45, p. R2165, 1992.

[51] D. Bonn, H. Kellay, M. Braunlich, M. B. Amar and J. Meunier, "Viscous fingering in complex fluids," *Physica A,* vol. 220, p. 60, 1995.

[52] A. Lindner, P. Coussot and D. Bonn, "Viscous fingering in a yield stress fluid," *Physical Review Letters,* vol. 85, p. 314, 2000.

[53] S. Malhotra and M. M. Sharma, "Impact of fluid elasticity on miscible viscous fingering," *Chemical Engineering Science,* vol. 117, p. 125, 2014.

[54] R. L. Chuoke, P. van Meurs, and C. van der Poel, "The instability of slow, immiscible, viscous liquid-liquid displacements in permeable media," *Petroleum Transuctions,* vol. 216, p. 188, 1959.

[55] E. J. Peters and D. L. Flock, "The onset of instability during two-phase immiscible displacement in porous media," *Society of Petroleum Engineers of AIME,* vol. 21, p. 249, 1981.

[56] C. T. Tan, G. M. Homsy, "Stability of miscible displacements in porous media: rectilinear flow," *Physics of Fluids,* vol. 29, p. 3549, 1986.

[57] C. T. Tan, G. M. Homsy, "Stability of miscible displacements in porous media: radial source flow," *Physics of Fluids,* vol. 30, p. 1239, 1987.

[58] K. Ghesmat and J. Azaiez, "Viscour fingering instability in porous media: Effect of anisotropic velocity-dependent dispersion tensor," *Transport in Porous Media,* vol. 73, p. 297, 2007.

[59] H. Alhumade, J. Azaiez, "Stability analysis of reversible reactive flow displacements in porous media," *Chemical Engineering Science,* vol. 101, p. 46, 2013.

[60] K. Ghesmat, H. Hassanzadeh, J. Abedi and Z. Chen, "Influence of nanoparticles on the dynamics of miscible Hele-Shaw flows," *Journal of Applied Physics,* vol. 109, p. 104907, 2011.

[61] S. H. Hejazi, P. M. J. Trevelyan, J. Azaiez and A. De Wit, "Viscous fingering of a miscible reactive A + B → C interface: a linear stability analysis," *Journal of Fluid Mechanics,* vol. 652, p. 501, 2010.

[62] H. Pascal, "Stability of non-Newtonian fluid interfaces in a porous medium and its applications in an oil displacement mechanism," *Journal of Colloid and Interface Science,* vol. 123, p. 14, 1988.

[63] S. D. R. Wilson, "The Taylor-Saffman problem for a non-Newtonian liquid," *Journal of Fluid Mechanics,* vol. 220, p. 413, 1990.

[64] J. E. Sader, D. Y. C. Chan and B. D. Hughes, "Non-Newtonian effects on immiscible viscous fingering in a radial Hele-Shaw cell," *Physical Review E,* vol. 49, p. 420, 1994.

[65] J. Azaiez and B. Singh, "Stability of miscible displacements of shear thinning fluids in a Hele-Shaw cell," *Physics of Fluids,* vol. 14, p. 1557, 2002.

[66] M. Reza Shoghi and M. Norouzi, "Linear stability analysis and nonlinear simulation of non-Newtonian viscous fingering instability in heterogeneous porous media," *Rheologica Acta,* vol. 54, p. 973, 2015.

[67] E. J. Koval, "A method for predicting the performance of unstable miscible displacement in heterogeneous media," *Society of Petroleum Engineers,* vol. 3, p. 145, 1963.

[68] M. R. Todd and W. J. Longstaff, "The development, testing, and application of a numerical simulator for predicting miscible flood performance," *Society of Petroleum Engineers,* vol. 24, p. 874, 1972.

[69] F. J. Fayers, "An approximate model with physically interpretable parameters for representing miscible viscous fingering," *Society of Petroleum Engineers,* vol. 3, p. 551, 1988.

[70] D. W. Peaceman and H. H. Rachford, "Numerical calculation of multidimensional miscible displacement," *Society of Petroleum Engineers,* vol. 2, p. 327, 1962.

[71] M. A. Christie and D. J. Bond, "Detailed simulation of unstable processes in miscible flooding," *Society of Petroleum Engineers,* vol. 2, p. 514, 1987.

[72] D. S. Kershaw, "The incomplete Cholesky-conjugate gradient method for the iterative solution of systems of linear equations," *Journal of Computational Physics,* vol. 26, p. 43, 1976.

[73] E. L. Dougherty, "Mathematical model of an unstable miscible displacement," *Society of Petroleum Engineers,* vol. 3, p. 155, 1962.

[74] C. T. Tan, G. M. Homsy, "Simulation of nonlinear viscous fingering in miscible displacement," *Physics of Fluids,* vol. 31, p. 1330, 1988.

[75] M. A. Christie, "High resolution simulation of unstable flows in porous media," *Society of Petroleum Engineers,* vol. 4, p. 297, 1989.

[76] U. G. Araktingi and F. M. Orr, "Viscous fingering, gravity segregation, and reservoir heterogeneity in miscible displacements in vertical cross sections," *Society of Petroleum Engineers,* p. 39, 1990.

[77] W. B. Zimmerman and G. M. Homsy, "Nonlinear viscous fingering in miscible displacement with anisotropic dispersion," *Physics of Fluids A,* vol. 3, p. 1859, 1991.

[78] W. B. Zimmerman and G. M. Homsy, "Viscous fingering in miscible displacements: Unification of effects of viscosity contrast, anisotropic dispersion, and velocity

dependence of dispersion on nonlinear finger propagation," *Physics of Fluids A,* vol. 4, p. 2348, 1992.

[79] S. Chen, B. Merriman, S. Osher and P. Smereka, "A simple level set method for solving stefan problems," *Journal of Computational Physics,* vol. 135, p. 8, 1997.

[80] T. Y. Hou, Z. Li, S. Osher and H. Zhao, "A hybrid method for moving interface problems with application to the Hele-Shaw flow," *Journal of Computational Physics,* vol. 134, p. 236, 1997.

[81] X. Guan, R. Pitchumani, "Viscous fingering in a Hele-Shaw cell with finite viscosity ratio and interfacial tension," *Journal of Fluids Engineering,* vol. 125, p. 354, 2003.

[82] J. Bear, Dynomics of fluids in porous media, New York: Dover, 1972.

[83] Q. Yuan, J. Azaiez, "Inertial effects in cyclic time-dependent displacement flows in homogeneous porous media," *Canadian Journal of Chemical Engineering,* vol. 93, p. 1490, 2015.

[84] S. J. Jackson, D. Stevens, H. Power and D. Giddings, "A boundary element method for the solution of finite mobility ratio immiscible displacement in a Hele-Shaw cell," *International Journal for Numerical Methods in Fluids,* vol. 78, p. 521, 2015.

[85] T. F. Lins and J. Azaiez, "Flow instabilities of Time-Dependent Injection Schemes in Immiscible Displacements," *The Canadian Journal of Chemical Engineering,* 2016.

[86] T. Lins and J. Azaiez, "Resonance-like dynamics in radial cyclic injection flows of immiscible fluids in homogenous porous media," *Journal of Fluid Mechanics,* vol. 819, pp. 713-729, 2017.

[87] C.-Y. Chen and E. Meiburg, "Miscible porous media displacements in the quarter five-spot configuration. Part 1. The homogeneous case," *Journal of Fluid Mechanics,* vol. 371, p. 233, 1998.

[88] C. Almarcha, P. Trevelyan, P. Grosfils and A. De Wit, "Chemically driven hydrodynamic instabilities," *Physical Review Letters,* vol. 104, p. 044501, 2010.

[89] M. Sajjadi and J. Azaiez, "Scaling and unified characterization of flow instabilities in layered heterogeneous porous media," *Physical Review E,* vol. 88, p. 033017, 2013.

[90] Q. Yuan, X. Zhou, F. Zeng, K. D. Knorr and M. Imran, "Investigation of concentration-dependent diffusion on frontal instabilities and mass transfer in homogeneous porous media," *The Canadian Journal of Chemical Engineering,* vol. 96, p. 323, 2018.

[91] Y.-S. Huang and C.-Y. Chen, "A numerical study on radial Hele-Shaw flow: influence of fluid miscibility and injection scheme," *Computational Mechanics,* vol. 55, p. 407, 2015.

[92] L. Kondic, M. J. Shelley and P. Palffy-Muhoray, "Non-Newtonian Hele-Shaw flow and the Saffman-Taylor instability," *Physical Review Letters,* vol. 80, p. 1433, 1998.

[93] H. Shokri, M. H. Kayhani and M. Norouzi, "Nonlinear simulation and linear stability analysis of viscous fingering instability of viscoelastic liquids," *Physics of Fluids,* vol. 29, p. 033101, 2017.

[94] H. Shokri, M. H. Kayhani and M. Norouzi, "Nonlinear viscoelastic fingering instability in miscible displacement through homogeneous and heterogeneous porous media," *Chemical Engineering Research and Manuscript Draft,* 2017.

[95] Y. Shi and G. Tang, "Non-Newtonian rheology property for two-phase flow on fingering phenomenon in porous media using the lattice Boltzmann method," *Journal of Non-Newtonian Fluid Mechanics,* vol. 229, p. 86, 2016.

[96] A. A. Yazdi and M. Norouzi, "Numerical study of Saffman–Taylor instability in immiscible nonlinear viscoelastic flows," *Rheologica Acta,* vol. 57, p. 575, 2018.

[97] M. Norouzi, A. Yazdi and A. Birjandi, "A numerical study on Saffman-Taylor instability of immiscible viscoelastic-Newtonian displacement in a Hele-Shaw cell," *Journal of Non-Newtonian Fluid Mechanics,* vol. 260, p. 109, 2018.

[98] R. B. Bird, R. C. Armstrong and O. Hassager, Dynamics of polymeric liquids volume 1 fluid mechanics, New York: John Wiley & Sons, 1987.

[99] Z. Li and I. Kazufumi, The immersed interface method: Numerical solutions of PDEs involving interfaces and irregular domains, Philadelphia: Society for Industrial and Applied Mathematics, 2006.

[100] T. Y. Hou, Z. Li, S. Osher and H. Zhao, "A hybrid method for moving interface problems with application to the Hele-Shaw flow," *Journal of Computational Physics,* vol. 134, p. 236, 1997.

[101] Z. Li, "A fast iterative algorithm for elliptic interface problems," *SIAM Journal on Numerical Analysis,* vol. 35, p. 230, 1998.

[102] S. Osher and R. Fedkiw, Level set methods and dynamic implicit surfaces, Los Angeles: Springer, 2003.

[103] J. A. Sethian, Level set methods and fast marching methods, Cambridge: Cambridge University Press, 1999.

[104] K. T. Chu, "Level set method library (LSMLIB)," [Online]. Available: http://ktchu.serendipityresearch.org/software/lsmlib/.

[105] Z. Li, "IIMPACK: A collection of fortran codes for interface problems," [Online]. Available: ftp.eos.ncsu.edu/pub/math/zhilin/Packages/FIIM_LEVEL.

Appendix

American Physical Society
Reuse and Permissions License

10-Sep-2019

T his license agreement between the American Physical Society ("APS") and Young Hoon Lee ("You") consists of your license details and the terms and conditions provided by the American Physical Society and SciPris.

Licensed Content Information

Lice nse Numbe r: RNP/19/SEP/018649
Lice nse date : 10-Sep-2019
DO I: 10.1103/PhysRevLett.56.336
Title : Radial viscous fingers and diffusion-limited aggregation: Fractal dimension and growth sites
Author: Gérard Daccord, Johann Nittmann, and H. Eugene Stanley
Publication: Physical Review Letters
Publishe r: American Physical Society
Cost: USD $ 0.00

Request Details

Doe s your re use re quire significant modifications: No
Spe cify inte nde d distribution locations:
Canada
Re use Cate gory: Reuse in a thesis/dissertation
Re que stor Type : Student
Ite ms for Re use : Figures/Tables
Numbe r of Figure /Table s: 1
Figure /Table s De tails: FIG. l. (a) Schematic illustration of the lateral and radial cells, (b) typical radial viscous finger, and (c) analysis of the fractal dimension by method (i).
Format for Re use : Print and Electronic
Total numbe r of print copie s: Up to 1000

Information about New Publication:

Unive rsity/Publishe r: University of Calgary
Title of disse rtation/the sis: Immiscible Radial Newtonian and non-Newtonian Flow Displacements in Porous Media
Author(s): Lee, Young Hoon
Expe cte d comple tion date : Sep. 2019

License Requestor Information

Name : Young Hoon Lee
Affiliation: Individual
Email Id: ddolee4@gmail.com
Country: Canada

TERMS AND CONDITIONS

T he American Physical Society (APS) is pleased to grant the Requestor of this license a non-exclusive, non-transferable permission, limited to Print and Electronic format, provided all criteria outlined below are followed.

1. You must also obtain permission from at least one of the lead authors for each separate work, if you haven't done so already. T he author's name and affiliation can be found on the first page of the published Article.
2. For electronic format permissions, Requestor agrees to provide a hyperlink from the reprinted APS material using the source material's DOI on the web page where the work appears. T he hyperlink should use the standard DOI resolution URL, http://dx.doi.org/{DOI}. T he hyperlink may be embedded in the copyright credit line.
3. For print format permissions, Requestor agrees to print the required copyright credit line on the first page where the material appears: "Reprinted (abstract/excerpt/figure) with permission from [(FULL REFERENCE CITAT ION) as follows: Author's Names, APS Journal T itle, Volume Number, Page Number and Year of Publication.] Copyright (YEAR) by the American Physical Society."
4. Permission granted in this license is for a one-time use and does not include permission for any future editions, updates, databases, formats or other matters. Permission must be sought for any additional use.
5. Use of the material does not and must not imply any endorsement by APS.
6. APS does not imply, purport or intend to grant permission to reuse materials to which it does not hold copyright. It is the requestor 's sole responsibility to ensure the licensed material is original to APS and does not contain the copyright of

another entity, and that the copyright notice of the figure, photograph, cover or table does not indicate it was reprinted by APS with permission from another source.
7. T he permission granted herein is personal to the Requestor for the use specified and is not transferable or assignable without express written permission of APS. T his license may not be amended except in writing by APS.
8. You may not alter, edit or modify the material in any manner.
9. You may translate the materials only when translation rights have been granted.
10. APS is not responsible for any errors or omissions due to translation.
11. You may not use the material for promotional, sales, advertising or marketing purposes.
12. T he foregoing license shall not take effect unless and until APS or its agent, Aptara, receives payment in full in accordance with Aptara Billing and Payment Terms and Conditions, which are incorporated herein by reference.
13. Should the terms of this license be violated at any time, APS or Aptara may revoke the license with no refund to you and seek relief to the fullest extent of the laws of the USA. Official written notice will be made using the contact information provided with the permission request. Failure to receive such notice will not nullify revocation of the permission.
14. APS reserves all rights not specifically granted herein.
15. T his document, including the Aptara Billing and Payment Terms and Conditions, shall be the entire agreement between the parties relating to the subject matter hereof.

American Physical Society
Reuse and Permissions License

10-Sep-2019
T his license agreement between the American Physical Society ("APS") and Young Hoon Lee ("You") consists of your license details and the terms and conditions provided by the American Physical Society and SciPris.

Licensed Content Information

Lice nse Numbe r: RNP/19/SEP/018648
Lice nse date : 10-Sep-2019
DO I: 10.1103/PhysRevLett.109.144502
Title : Minimization of Viscous Fluid Fingering: A Variational Scheme for
Optimal Flow Rates
Author: Eduardo O. Dias et al.
Publication: Physical Review Letters
Publishe r: American Physical Society
Cost: USD $ 0.00

Request Details

Doe s your re use re quire significant modifications: No
Spe cify inte nde d distribution
locations:
Canada
Re use Cate gory: Reuse in a thesis/dissertation
Re que stor Type : Student
Ite ms for Re use : Figures/Tables
Numbe r of Figure /Table s: 1
Figure /Table s De tails: FIG. 4. Typical experimental patterns at time tf ¼ 20 s for (a) Q0 ¼
2:08 cm2=s, and (b) its corresponding ideal injection rate. For (a) and
(b) T f ¼ 65 and Ca ¼ 112.
Format for Re use : Print and Electronic
Total numbe r of print copie s: Up to 1000

Information about New Publication:

Unive rsity/Publishe r: University of Calgary
Title of disse rtation/the sis: Immiscible Radial Newtonian and non-Newtonian Flow Displacements
in Porous Media
Author(s): Lee, Young Hoon
Expe cte d comple tion date : Sep. 2019

License Requestor Information

Name : Young Hoon Lee
Affiliation: Individual
Email Id: ddolee4@gmail.com
Country: Canada

TERMS AND CONDITIONS

T he American Physical Society (APS) is pleased to grant the Requestor of this license a non-exclusive, non-transferable permission, limited to Print and Electronic format, provided all criteria outlined below are followed.
1. You must also obtain permission from at least one of the lead authors for each separate work, if you haven’t done so

already. T he author's name and affiliation can be found on the first page of the published Article.
2. For electronic format permissions, Requestor agrees to provide a hyperlink from the reprinted APS material using the source material's DOI on the web page where the work appears. T he hyperlink should use the standard DOI resolution URL, http://dx.doi.org/{DOI}. T he hyperlink may be embedded in the copyright credit line.
3. For print format permissions, Requestor agrees to print the required copyright credit line on the first page where the material appears: "Reprinted (abstract/excerpt/figure) with permission from [(FULL REFERENCE CITAT ION) as follows: Author's Names, APS Journal T itle, Volume Number, Page Number and Year of Publication.] Copyright (YEAR) by the American Physical Society."
4. Permission granted in this license is for a one-time use and does not include permission for any future editions, updates, databases, formats or other matters. Permission must be sought for any additional use.
5. Use of the material does not and must not imply any endorsement by APS.
6. APS does not imply, purport or intend to grant permission to reuse materials to which it does not hold copyright. It is the requestor 's sole responsibility to ensure the licensed material is original to APS and does not contain the copyright of another entity, and that the copyright notice of the figure, photograph, cover or table does not indicate it was reprinted by APS with permission from another source.
7. T he permission granted herein is personal to the Requestor for the use specified and is not transferable or assignable without express written permission of APS. T his license may not be amended except in writing by APS.
8. You may not alter, edit or modify the material in any manner.
9. You may translate the materials only when translation rights have been granted.
10. APS is not responsible for any errors or omissions due to translation.
11. You may not use the material for promotional, sales, advertising or marketing purposes.
12. T he foregoing license shall not take effect unless and until APS or its agent, Aptara, receives payment in full in accordance with Aptara Billing and Payment Terms and Conditions, which are incorporated herein by reference.
13. Should the terms of this license be violated at any time, APS or Aptara may revoke the license with no refund to you and seek relief to the fullest extent of the laws of the USA. Official written notice will be made using the contact information provided with the permission request. Failure to receive such notice will not nullify revocation of the permission.
14. APS reserves all rights not specifically granted herein.
15. T his document, including the Aptara Billing and Payment Terms and Conditions, shall be the entire agreement between the parties relating to the subject matter hereof.

ELSEVIER LICENSE TERMS AND CONDITIONS

Sep 10, 2019

This Agreement between University of Calgary -- Younng Hoon Lee ("You") and Elsevier ("Elsevier") consists of your license details and the terms and conditions provided by Elsevier and Copyright Clearance Center.

License Number 4665500594383
License date Sep 10, 2019
Licensed Content Publisher Elsevier
Licensed Content Publication Physica D: Nonlinear Phenomena
Licensed Content Title Viscous fingering patterns in polymer solutions
Licensed Content Author Masami Kawaguchi,Kyoko Makino,Tadaya Kato
Licensed Content Date Nov 15, 1997
Licensed Content Volume 109
Licensed Content Issue 3-4
Licensed Content Pages 8
Start Page 325
End Page 332
Type of Use reuse in a thesis/dissertation
Portion figures/tables/illustrations
Number of
figures/tables/illustrations

1
Format both print and electronic
Are you the author of this
Elsevier article?
No
Will you be translating? No
Original figure numbers Fig. 4. Fingering pattern for the 0.5gper 100ml HPMC-I solutions at
several injection pressures of 1.0, 2.0, 3~0, and 5.0kPa.
Title of your
thesis/dissertation
Immiscible Radial Newtonian and non-Newtonian Flow
Displacements in Porous Media
Expected completion date Sep 2019
Estimated size (number of
pages)
100
Requestor Location University of Calgary
2500 University Drive NW
Calgary, AB T2N 1N4
Canada
Attn: University of Calgary
Publisher Tax ID GB 494 6272 12
Total 0.00 CAD
Terms and Conditions

INTRODUCTION

1. The publisher for this copyrighted material is Elsevier. By clicking "accept" in connection
with completing this licensing transaction, you agree that the following terms and conditions
apply to this transaction (along with the Billing and Payment terms and conditions established by Copyright Clearance Center, Inc. ("CCC"), at the time that you opened your
Rightslink account and that are available at any time at
http://myaccount.copyright.com).

GENERAL TERMS

2. Elsevier hereby grants you permission to reproduce the aforementioned material subject to
the terms and conditions indicated.

3. Acknowledgement: If any part of the material to be used (for example, figures) has
appeared in our publication with credit or acknowledgement to another source, permission

must also be sought from that source. If such permission is not obtained then that
material
may not be included in your publication/copies. Suitable acknowledgement to the
source
must be made, either as a footnote or in a reference list at the end of your
publication, as
follows:
"Reprinted from Publication title, Vol /edition number, Author(s), Title of article /
title of
chapter, Pages No., Copyright (Year), with permission from Elsevier [OR
APPLICABLE
SOCIETY COPYRIGHT OWNER]." Also Lancet special credit - "Reprinted from The
Lancet, Vol. number, Author(s), Title of article, Pages No., Copyright (Year), with
permission from Elsevier."
4. Reproduction of this material is confined to the purpose and/or media for which
permission is hereby given.
5. Altering/Modifying Material: Not Permitted. However figures and illustrations may
be
altered/adapted minimally to serve your work. Any other abbreviations, additions,
deletions
and/or any other alterations shall be made only with prior written authorization of
Elsevier
Ltd. (Please contact Elsevier at permissions@elsevier.com). No modifications can be
made
to any Lancet figures/tables and they must be reproduced in full.
6. If the permission fee for the requested use of our material is waived in this
instance,
please be advised that your future requests for Elsevier materials may attract a fee.
7. Reservation of Rights: Publisher reserves all rights not specifically granted in the
combination of (i) the license details provided by you and accepted in the course of
this

licensing transaction, (ii) these terms and conditions and (iii) CCC's Billing and Payment
terms and conditions.

8. License Contingent Upon Payment: While you may exercise the rights licensed immediately upon issuance of the license at the end of the licensing process for the transaction, provided that you have disclosed complete and accurate details of your proposed
use, no license is finally effective unless and until full payment is received from you (either
by publisher or by CCC) as provided in CCC's Billing and Payment terms and conditions. If
full payment is not received on a timely basis, then any license preliminarily granted shall be
deemed automatically revoked and shall be void as if never granted. Further, in the event
that you breach any of these terms and conditions or any of CCC's Billing and Payment
terms and conditions, the license is automatically revoked and shall be void as if never
granted. Use of materials as described in a revoked license, as well as any use of the
materials beyond the scope of an unrevoked license, may constitute copyright infringement
and publisher reserves the right to take any and all action to protect its copyright in the
materials.

9. Warranties: Publisher makes no representations or warranties with respect to the licensed
material.

10. Indemnity: You hereby indemnify and agree to hold harmless publisher and CCC, and

their respective officers, directors, employees and agents, from and against any and
all
claims arising out of your use of the licensed material other than as specifically
authorized
pursuant to this license.
11. No Transfer of License: This license is personal to you and may not be
sublicensed,
assigned, or transferred by you to any other person without publisher's written
permission.
12. No Amendment Except in Writing: This license may not be amended except in a
writing
signed by both parties (or, in the case of publisher, by CCC on publisher's behalf).
13. Objection to Contrary Terms: Publisher hereby objects to any terms contained in
any
purchase order, acknowledgment, check endorsement or other writing prepared by
you,
which terms are inconsistent with these terms and conditions or CCC's Billing and
Payment
terms and conditions. These terms and conditions, together with CCC's Billing and
Payment
terms and conditions (which are incorporated herein), comprise the entire
agreement
between you and publisher (and CCC) concerning this licensing transaction. In the
event of
any conflict between your obligations established by these terms and conditions and
those
established by CCC's Billing and Payment terms and conditions, these terms and
conditions
shall control.
14. Revocation: Elsevier or Copyright Clearance Center may deny the permissions
described

in this License at their sole discretion, for any reason or no reason, with a full refund payable
to you. Notice of such denial will be made using the contact information provided by you.
Failure to receive such notice will not alter or invalidate the denial. In no event will Elsevier
or Copyright Clearance Center be responsible or liable for any costs, expenses or damage
incurred by you as a result of a denial of your permission request, other than a refund of the
amount(s) paid by you to Elsevier and/or Copyright Clearance Center for denied permissions.

LIMITED LICENSE

The following terms and conditions apply only to specific license types:

15. Translation: This permission is granted for non-exclusive world English rights only unless your license was granted for translation rights. If you licensed translation rights you
may only translate this content into the languages you requested. A professional translator
must perform all translations and reproduce the content word for word preserving the
integrity of the article.

16. Posting licensed content on any Website: The following terms and conditions apply as
follows: Licensing material from an Elsevier journal: All content posted to the web site must
maintain the copyright information line on the bottom of each image; A hyper-text must be
included to the Homepage of the journal from which you are licensing at
http://www.sciencedirect.com/science/journal/xxxxx or the Elsevier homepage for books at

http://www.elsevier.com; Central Storage: This license does not include permission for a
scanned version of the material to be stored in a central repository such as that provided by
Heron/XanEdu.
Licensing material from an Elsevier book: A hyper-text link must be included to the Elsevier
homepage at http://www.elsevier.com . All content posted to the web site must maintain the
copyright information line on the bottom of each image.
Posting licensed content on Electronic reserve: In addition to the above the following clauses are applicable: The web site must be password-protected and made available only to
bona fide students registered on a relevant course. This permission is granted for 1 year only.
You may obtain a new license for future website posting.
17. For journal authors: the following clauses are applicable in addition to the above:
Preprints:
A preprint is an author's own write-up of research results and analysis, it has not been peerreviewed,
nor has it had any other value added to it by a publisher (such as formatting, copyright, technical enhancement etc.).
Authors can share their preprints anywhere at any time. Preprints should not be added to or
enhanced in any way in order to appear more like, or to substitute for, the final versions of
articles however authors can update their preprints on arXiv or RePEc with their Accepted
Author Manuscript (see below).
If accepted for publication, we encourage authors to link from the preprint to their formal

publication via its DOI. Millions of researchers have access to the formal publications on
ScienceDirect, and so links will help users to find, access, cite and use the best available
version. Please note that Cell Press, The Lancet and some society-owned have different
preprint policies. Information on these policies is available on the journal homepage.

Accepted Author Manuscripts: An accepted author manuscript is the manuscript of an article that has been accepted for publication and which typically includes authorincorporated
changes suggested during submission, peer review and editor-author communications.

Authors can share their accepted author manuscript:

- immediately
  - via their non-commercial person homepage or blog
  - by updating a preprint in arXiv or RePEc with the accepted manuscript
  - via their research institute or institutional repository for internal institutional uses or as part of an invitation-only research collaboration work-group
  - directly by providing copies to their students or to research collaborators for their personal use
  - for private scholarly sharing as part of an invitation-only work group on commercial sites with which Elsevier has an agreement
- After the embargo period
  - via non-commercial hosting platforms such as their institutional repository
  - via commercial sites with which Elsevier has an agreement

In all cases accepted manuscripts should:

- link to the formal publication via its DOI
- bear a CC-BY-NC-ND license - this is easy to do
- if aggregated with other manuscripts, for example in a repository or other site, be shared in alignment with our hosting policy not be added to or enhanced in any way to
appear more like, or to substitute for, the published journal article.

Published journal article (JPA): A published journal article (PJA) is the definitive final record of published research that appears or will appear in the journal and embodies all
value-adding publishing activities including peer review co-ordination, copy-editing, formatting, (if relevant) pagination and online enrichment.
Policies for sharing publishing journal articles differ for subscription and gold open access
articles:
Subscription Articles: If you are an author, please share a link to your article rather than the
full-text. Millions of researchers have access to the formal publications on ScienceDirect,
and so links will help your users to find, access, cite, and use the best available version.
Theses and dissertations which contain embedded PJAs as part of the formal submission can
be posted publicly by the awarding institution with DOI links back to the formal publications on ScienceDirect.
If you are affiliated with a library that subscribes to ScienceDirect you have additional
private sharing rights for others' research accessed under that agreement. This includes use
for classroom teaching and internal training at the institution (including use in course packs
and courseware programs), and inclusion of the article for grant funding purposes.
Gold Open Access Articles: May be shared according to the author-selected end-user license and should contain a CrossMark logo, the end user license, and a DOI link to the
formal publication on ScienceDirect.
Please refer to Elsevier's posting policy for further information.
18. **For book authors** the following clauses are applicable in addition to the above:

Authors are permitted to place a brief summary of their work online only. You are not
allowed to download and post the published electronic version of your chapter, nor may you
scan the printed edition to create an electronic version. Posting to a repository: Authors are
permitted to post a summary of their chapter only in their institution's repository.
19. Thesis/Dissertation: If your license is for use in a thesis/dissertation your thesis may be
submitted to your institution in either print or electronic form. Should your thesis be
published commercially, please reapply for permission. These requirements include
permission for the Library and Archives of Canada to supply single copies, on demand, of
the complete thesis and include permission for Proquest/UMI to supply single copies, on
demand, of the complete thesis. Should your thesis be published commercially, please
reapply for permission. Theses and dissertations which contain embedded PJAs as part of
the formal submission can be posted publicly by the awarding institution with DOI links
back to the formal publications on ScienceDirect.

Elsevier Open Access Terms and Conditions

You can publish open access with Elsevier in hundreds of open access journals or in nearly
2000 established subscription journals that support open access publishing. Permitted third
party re-use of these open access articles is defined by the author's choice of Creative
Commons user license. See our open access license policy for more information.

Terms & Conditions applicable to all Open Access articles published with Elsevier:

formal publication through the relevant DOI), provides a link to the license, indicates if
changes were made and the licensor is not represented as endorsing the use made of the
work. Further, any new works must be made available on the same conditions. The full
details of the license are available at http://creativecommons.org/licenses/by-nc-sa/4.0.

CC BY NC ND: The CC BY-NC-ND license allows users to copy and distribute the Article,
provided this is not done for commercial purposes and further does not permit distribution of
the Article if it is changed or edited in any way, and provided the user gives appropriate
credit (with a link to the formal publication through the relevant DOI), provides a link to the
license, and that the licensor is not represented as endorsing the use made of the work. The
full details of the license are available at http://creativecommons.org/licenses/by-nc-nd/4.0.

Any commercial reuse of Open Access articles published with a CC BY NC SA or CC BY
NC ND license requires permission from Elsevier and will be subject to a fee.

Commercial reuse includes:

• Associating advertising with the full text of the Article
• Charging fees for document delivery or access
• Article aggregation
• Systematic distribution via e-mail lists or share buttons

Posting or linking by commercial companies for use by customers of those companies.

20. Other Conditions:

v1.9

Questions? customercare@copyright.com or +1-855-239-3415 (toll free in the US) or
+1-978-646-2777.